

File with N74-22633

INVESTIGATION OF THE EFFECT OF HUB SUPPORT PARAMETERS
ON TWO-BLADED ROTOR OSCILLATORY LOADS

By Charles D. Lee and James A. White



Prepared under Contract NAS1-11352 by
BELL HELICOPTER COMPANY
Fort Worth, Texas

for

NATIONAL AERONAUTICS AND SPACE ADMINISTRATION

May 1974

INVESTIGATION OF THE EFFECT OF HUB SUPPORT PARAMETERS
ON TWO-BLADED ROTOR OSCILLATORY LOADS

By Charles D. Lee and James A. White

Prepared under Contract NAS1-11352 by
BELL HELICOPTER COMPANY
Fort Worth, Texas

for

NATIONAL AERONAUTICS AND SPACE ADMINISTRATION

May 1974

TABLE OF CONTENTS

	<u>Page</u>
SUMMARY	1
INTRODUCTION	2
SYMBOLS	3
TECHNICAL DISCUSSION	5
Basic Concepts of Impedance	5
Effects of Variation in Hub Impedance	6
Method of Varying Parameters	8
TEST EQUIPMENT	9
Model Description	9
Rotor System	10
Scaling Criteria	11
Instrumentation System	11
TEST PROGRAM AND PROCEDURES	12
Shake Test Procedure	12
Tunnel Test Procedure	13
TEST RESULTS	13
Ground Vibration Tests	13
Tunnel Tests	15
CONCLUSIONS	17
REFERENCES	19
TABLES	20
FIGURES	27
APPENDIX	49

LIST OF TABLES

<u>Table No.</u>		<u>Page</u>
I	SCALING FACTORS	20
II	MODEL INSTRUMENTATION LIST	21
III	COMPARISON OF COMPUTED AND MEASURED PYLON NATURAL FREQUENCIES	22
IV	MODEL UH-1D 1/5 SCALE ROTOR LONGITUDINAL SHAKE TESTS	23
V	MODEL UH-1D 1/5 SCALE ROTOR LATERAL SHAKE TESTS	25
VI	COMPARISON OF COMPUTED AND MEASURED FREE-FREE ROTOR NATURAL FREQUENCIES	26

LIST OF FIGURES

<u>Figure No.</u>		<u>Page</u>
1	Characteristics of Rotating System Natural Frequencies with Rotor Rotational Speed	27
2	One-per-rev Inplane Rotor Response for a Typical Pylon/Rotor Coupled System During Normal Run-up	28
3	Coupled Coincident Rotating Natural Frequency Variation with Pylon Mass and Spring Rate	29
4	One-per-rev Inplane Rotor Response Variation with Pylon Frequency Ratio ...	30
5	Variation of Normalized One-per-rev Inplane Bending Moment with a) Pylon Frequency Ratio, b) Pylon Mass Ratio ...	31
6	Model Installed in Tunnel	32
7	Model Schematic	33
8	Tunnel Installation Dimensional Data All Dimensions in Centimeters	34

LIST OF FIGURES (Continued)

<u>Figure No.</u>		<u>Page</u>
9	One-fifth Scale UH-1D Model Rotor Natural Frequencies, Collective Mode Fan Plot	35
10	One-fifth Scale UH-1D Model Rotor Natural Frequencies, Cyclic Mode Fan Plot	36
11	Shake Test Installation	37
12	Shake Test Controls and Data Acquisition System	38
13	Block Diagram of Ground Vibration Test Data Acquisition System	39
14	Variation of Longitudinal Pylon and Rotor Natural Frequencies with Pylon Mass Ratio and Spring Rate	40
15	Variation of Lateral Pylon and Rotor Natural Frequencies with Pylon Mass Ratio and Spring Rate	41
16	Pylon Fixed System Coincident Frequencies	42
17	Comparison of Computed and Measured One-per-rev Oscillatory Inplane Bending Moment (15.6-percent Radius) vs Pylon Mass Ratio and Spring Rate for $V = 20.7$ m/s, rpm = 720, and $\theta_0 = 16^\circ$.	43
18	Variation of Inplane Bending Moment (15.6-percent Radius) with Pylon Mass Ratio and Spring Rate for $V = 32.3$ m/s, rpm = 720, and $\theta_0 = 16^\circ$...	44
19	Variation of Inplane Bending Moment (15.6-percent Radius) with Pylon Mass Ratio and Spring Rate for $V = 20.7$ m/s, rpm = 650, and $\theta_0 = 16^\circ$	45

LIST OF FIGURES (Continued)

<u>Figure No.</u>		<u>Page</u>
20	Variation of Inplane Bending Moment (15.6-percent Radius) with Pylon Mass Ratio and Spring Rate for $V = 32.3 \text{ m/s}$, $\text{rpm} = 650$, and $\theta_0 = 16^\circ$...	46
21	One-fifth Scale UH-1D Main Rotor Oscillatory Bending Moment vs Percent Radius for Maximum and Minimum Hub Impedance at $V = 20.7 \text{ m/s}$, $\text{rpm} = 720$, and $\theta_0 = 16^\circ$...	47
22	Pylon Longitudinal Hub Mobility vs Frequency for $K_p = 400 \text{ N/cm}$ and $\bar{m} = 3.35$	51
23	Pylon Longitudinal Hub Mobility vs Frequency for $K_p = 1050 \text{ N/cm}$ and $\bar{m} = 3.35$	52
24	Pylon Longitudinal Hub Mobility vs Frequency for $K_p = 1120 \text{ N/cm}$ and $\bar{m} = 3.35$	53
25	Coupled Pylon/Rotor Longitudinal Hub Mobility vs Frequency for $K_p = 400$ N/cm and $\bar{m} = 3.35$	54
26	Coupled Pylon/Rotor Longitudinal Hub Mobility vs Frequency for $K_p = 1050$ N/cm and $\bar{m} = 3.35$	55
27	Coupled Pylon/Rotor Longitudinal Hub Mobility vs Frequency for $K_p = 1120 \text{ N/cm}$ and $\bar{m} = 3.35$	56
28	Instrumented Blade Vertical Tip Transfer Mobility vs Frequency for Inplane Excitation at Rotor Hub (Pylon/ Rotor Assembly) $K_p = 1050 \text{ N/cm}$ and $\bar{m} = 3.35$	57
29	Free-Free Rotor Inplane Hub Mobility vs Frequency for Single Inplane Exciter at Instrumented Blade Tip	58

LIST OF FIGURES (Continued)

<u>Figure No.</u>		<u>Page</u>
30	Free-Free Rotor Inplane Hub Mobility vs. Frequency for Inplane Excitation at Each Blade Tip	59
31	Blade Inplane Bending Moment @ 15.6 Percent Radius, $\alpha_s = -2^\circ$, $\theta_o = 16^\circ$	60
32	Blade Inplane Bending Moment @ 28.8 Percent Radius, $\alpha_s = -2^\circ$, $\theta_o = 16^\circ$	61
33	Blade Inplane Bending Moment @ 47.9 Percent Radius, $\alpha_s = -2^\circ$, $\theta_o = 16^\circ$	62
34	Blade Inplane Bending Moment @ 59.0 Percent Radius, $\alpha_s = -2^\circ$, $\theta_o = 16^\circ$	63
35	Blade Flapwise Bending Moment @ 15.6 Percent Radius, $\alpha_s = -2^\circ$, $\theta_o = 16^\circ$	64
36	Blade Flapwise Bending Moment @ 28.8 Percent Radius, $\alpha_s = -2^\circ$, $\theta_o = 16^\circ$	65
37	Blade Flapwise Bending Moment @ 47.9 Percent Radius, $\alpha_s = -2^\circ$, $\theta_o = 16^\circ$	66
38	Blade Flapwise Bending Moment @ 59.0 Percent Radius, $\alpha_s = -2^\circ$, $\theta_o = 16^\circ$	67
39	Blade Torsional Moment @ 15.6 Percent Radius, $\alpha_s = -2^\circ$, $\theta_o = 16^\circ$	68
40	Blade Torsional Moment @ 47.9 Percent Radius, $\alpha_s = -2^\circ$, $\theta_o = 16^\circ$	69
41	Pitch Link Axial Load, $\alpha_s = -2^\circ$, $\theta_o = 16^\circ$	70
42	Blade Inplane Bending Moment vs Collective Blade Angle $V = 20.7$ m/s, rpm = 720, $\alpha_s = -2^\circ$, 15.6%R	71

LIST OF FIGURES (Continued)

<u>Figure No.</u>		<u>Page</u>
43	Blade Inplane Bending Moment vs Collective Blade Angle $V = 32.3 \text{ m/s}$, $\text{rpm} = 650$, $\alpha_s = -2^\circ$, 15.6%R	72
44	Blade Flapwise Bending Moment vs Collective Blade Angle $V = 20.7 \text{ m/s}$, $\text{rpm} = 720$, $\alpha_s = -2^\circ$, 15.6%R	73
45	Blade Flapwise Bending Moment vs Collective Blade Angle $V = 32.3 \text{ m/s}$, $\text{rpm} = 650$, $\alpha_s = -2^\circ$, 15.6%R	74

INVESTIGATION OF THE EFFECT OF HUB SUPPORT PARAMETERS ON TWO-BLADED ROTOR OSCILLATORY LOADS*

By Charles D. Lee and James A. White
Bell Helicopter Company

SUMMARY

This report presents the results of a test program and analysis to investigate the effects of inplane hub support parameters on the oscillatory chordwise loads of a two-bladed teetering rotor. The test program was conducted in two phases. Phase I consisted of a shake test to define the impedance of a number of test configurations as a function of frequency. Phase II was the test of these configurations in the NASA-Langley Transonic Dynamics Tunnel.

The test rotor was a one-fifth-scale dynamically and aerodynamically similar model (Mach scaling) of the UH-1D rotor system. The variations in hub support parameters were achieved by changing the spring rate of the pylon mounts and/or the pylon mass. System frequencies and inplane hub mobility (the inverse of hub impedance) were obtained during Phase I tests by shaking the rotor hub, both laterally and longitudinally, for each of nine combinations of pylon springs and masses. Hub mobility is the hub response per exciting force. During Phase II, rotor loads, including inplane (chordwise), flapwise (beamwise), and torsional bending moments were measured at several blade stations.

The test showed that the one-per-rev inplane bending moments could be changed by a factor of 2.0 as a function of the pylon configuration at the same aerodynamic operating condition. The higher harmonic inplane, flapwise, and torsional bending moments, and pitch link axial loads were not affected by changes in inplane hub impedance. The maximum inplane loads occurred for the pylon configuration with the minimum spring rate and maximum inertia (i.e., the pylon configuration with its natural frequency farthest from the rotor operating speed). The minimum inplane loads occurred for the pylon configuration with the maximum spring rate and minimum inertia (i.e., the configuration with its pylon natural frequency nearest the rotor operating speed).

The test results generally substantiated the predicted trends although differences in the magnitude of the bending moments were observed when compared to predicted results. Some of these differences were due to influence of the model balance and/or tunnel floor on hub impedance. No variations were noted which are attributable to direct aerodynamic influence.

*The contract research effort which has lead to the results in this report was financially supported by USAAMRDL (Langley Directorate).

INTRODUCTION

The analysis of rotor/pylon interaction is fundamental to the determination of two-bladed teetering rotor response. (For multibladed rotor systems, less significance is apportioned to this characteristic, particularly for hinged rotors where the blades are effectively decoupled from the hub.) Over the years, a number of reports and papers have been published on this subject (e.g., the reports by Coleman/Feingold and Brooks, refs. 1 and 2). The emphasis in these papers was directed to the stability characteristics of the rotor/pylon system and little attention was given to the effect of support system parameters on rotor response under the influence of airloads. In addition, methods for the determination of the parameters required to simulate these effects analytically had not been and are not presently fully developed.

The top of the transmission shaft, or mast, is the boundary for the rotor. Historically, thought and analysis have been facilitated by separating the rotor and fuselage systems at this location. Although high-speed computers have eliminated the practical necessity of this, it continues to be in common usage. The dynamic restraint offered to the rotor is called hub impedance. The primary factors determining hub impedance are the pylon mass, damping, and spring rate. As the pylon mass (inertia) and/or spring rate increase without bound, the hub impedance approaches infinity and the rotor approaches cantilever response. Conversely, as the pylon mass and spring rate approach zero, the rotor response approaches the free-free condition (zero hub impedance). An explanation of mobility (and thus of impedance) is presented in reference 3, and is further discussed in references 4 and 5. The effect of impedance on rotor dynamic characteristics is discussed in a subsequent section.

A significant increase in understanding of hub impedance and its impact on rotor loads has resulted from recent analytical studies and small-scale model tests. (See ref. 6.) Reference 7 contains a discussion of hub impedance and its importance to the prediction of rotor responses and to the correlation of full-scale, model-scale, and analytical data. Small-scale dynamic model tests have been conducted to substantiate and improve the analytical treatment. Most of these tests have been conducted with only dynamic considerations and little aerodynamic testing has been done to evaluate these concepts.

The purpose of this program was to provide data, which included aerodynamic as well as dynamic influence, to evaluate the effect of inplane hub impedance on rotor oscillatory loads.

SYMBOLS

cg	center of gravity	
F	force	newton
g	acceleration due to gravity	meter/second ²
I	moment of inertia	kilogram meter ²
K	spring rate	newton/centimeter
m	concentrated mass	kilogram
\bar{m}	pylon mass ratio $= m_{pe}/m_R$	-
M (1.0,90.)	advancing tip Mach number	-
R	radius	meter
\bar{R}	response	meter, meter/second, meter/second ²
R'	product of gravitational acceleration and gas constant	meter ² second ² /degree
r	distance from cg to pylon pivot point	meter
s	distance from hub center to pylon pivot point	meter
T	temperature	kelvin
t	time	second
V	velocity	meter/second
Z	impedance	newton second ² /meter
α_s	shaft angle	degree

γ	ratio of specific heats	-
θ_0	blade root collective angle	degree
λ	model scale = model length/ full-scale length	-
μ	advance ratio = $\frac{V}{\Omega R}$	-
μ'	dynamic viscosity	newton/second/meter ²
ρ	mass density	kilogram/meter ³
ϕ	phase angle	degree
Ω	rotational frequency	hertz
ω	natural frequency	hertz
$\bar{\omega}$	pylon frequency ratio = ω_c / Ω	

Subscripts:

b, ζ	blade
c	coincident frequencies
e	effective
FS	full scale
H	hub
M	model
P	pylon
R	rotor
r	rotating system
u	uncoupled

TECHNICAL DISCUSSION

Basic Concepts of Impedance

The purpose of the tests reported herein was to determine the effect of pylon inertia and spring rate on the chordwise one-per-rev load of a two-bladed teetering rotor. The pylon inertia and spring rate together determine the dynamic boundary condition for the rotor in the plane of rotation (at the rotor hub). This dynamic reaction has many names: hub impedance, hub mobility, hub effective mass, hub effective spring, etc. The name preferred here is hub impedance, defined as:

$$Z(\omega) = Fe^{i\omega t} / \bar{R}e^{i(\omega t + \phi)}$$

Where F is the magnitude of a harmonic force and \bar{R} is the magnitude of the harmonic response (acceleration, velocity, or displacement). The general development of the impedance/mobility method is described in references 3 through 5. The impedance/mobility method is currently being investigated in several areas for its efficacy as an analytical method for helicopter analysis, and will not be pursued herein. Only the definition of impedance with respect to dynamic reaction will be used.

Coleman, et al. (ref. 1) demonstrated that the coupled natural frequencies of the rotor and support system (for an isotropic support) in rotating coordinates have the characteristics shown in Figure 1a. The uncoupled rotating system frequencies are given by points A and B and by the dashed lines in the figure. The uncoupled blade frequency (point A) is the system frequency determined by setting the pylon support spring to zero (Figure 1b), but retaining the support system mass. The uncoupled pylon frequency (point B) is the system frequency determined by ignoring the blade flexibility and retaining the blade mass. Other definitions of the system uncoupled frequencies are possible, but result in the same coupled system values. The coupled frequencies are given by the solid curves in the figure. Points C and D define an instability region associated with the first whirl frequency (critical speed) of the pylon; however, structural damping is generally sufficient to stabilize this mode which is excited by a rotor out-of-balance force (not by one-per-rev airloads).

These points (A through D) do not directly influence the rotor one-per-rev airload response. They are presented here for the purpose of acquainting the reader with the Coleman frequency diagram and will not be discussed further.

Points E and F of Figure 1a are the coupled natural frequencies of the pylon and rotor (in the rotating system) that are coincident with the rotor speed and are excited by one-per-rev airloads. In ensuing discussions, the symbols ω_p and $\omega_{\zeta c}$ will be used for the coupled natural frequencies given by points E and F, respectively. The uncoupled coincident rotating frequency given by point G in Figure 1a corresponds to that case for which the rotor is rigid. In this case, the rotor speed at which coincidence occurs is equal to $\omega_{pu}/2$, where ω_{pu} is the pylon uncoupled frequency. The symbol ω_c will be used for point G in the discussion that follows.

Figure 2 shows the rotor one-per-rev inplane bending moment (rotating system) during run-up as characterized by ω_{pc} and $\omega_{\zeta c}$ (points E and F of Figure 1a). The response of the system at ω_{pc} (point E) involves mostly pylon motion while that at $\omega_{\zeta c}$ (point F) involves mostly blade motion.

Effects of Variation in Hub Impedance

The results of the analytical and experimental studies described in reference 6 are given in Figures 3 and 4. Figure 3 gives the coupled coincident natural frequencies (ω_{pc} , $\omega_{\zeta c}$) of the pylon and the rotor as a function of ω_c as defined previously. The figure is computed by varying the support system spring rate, with constant support system mass and rotor parameters, and determining the frequencies of the maximum response of the system. The analytical model used for this determination is shown in the figure. The diagonal line, $\omega_c = \Omega$, is the uncoupled coincident pylon frequency for an infinitely stiff inplane rotor. For zero support system spring, ω_c and $\omega_{pc} = 0$, and $\omega_{\zeta c}$ is the free-free rotor frequency including the pylon mass. This establishes the minima for the coupled frequency curves. For an infinite support system spring rate, $\omega_{\zeta c}$ and $\omega_c = \infty$ and ω_{pc} asymptotically approaches the cantilever blade frequency. This establishes the upper limit for the coupled frequency curves. The variation of the coupled frequencies is given by the curves in the figure. The solid curves show the frequency variation for a light support system and the dotted curves show the variation for a heavy system both with increasing spring rate.

Figure 3 shows the loci of maximum response of the rotor to one-per-rev airloads for all two degree-of-freedom isotropic support systems and a specified rotor system. This figure was verified experimentally from run-up data for a series of pylon configurations with constant mass as follows. For each configuration tested, the uncoupled pylon coincident frequency,

ω_c , was determined by shake tests. The blade inplane bending moment for each configuration tested was measured for incremental rotor speeds. The rotor speed (or natural frequency) for each maximum response was recorded and plotted as a function of ω_c . Thus, the ordinate of Figure 3 is also the rotor operating speed at which maximum rotor response occurs due to one-per-rev airloads.

Figure 4 gives the one-per-rev inplane bending moment, normalized on the rotor cantilever response, as a function of pylon frequency ratio. The pylon frequency ratio, $\bar{\omega}$, is defined as the ratio of ω_c to the rotor operating speed (i.e., $\bar{\omega} = \omega_c / \Omega$). This figure is generated by computing the inplane rotor response for each pylon configuration at a given rotor speed, dividing the result by the cantilever rotor response for the same rotor speed, and plotting this ratio as a function of $\bar{\omega}$. Experimentally, this graph was generated by determining the response at a given rotor speed from run-up graphs for each pylon configuration, forming the response ratio, and plotting this ratio as a function of $\bar{\omega}$.

Figure 4 can also be generated conceptually from Figure 3. Choose a rotor operating speed less than the blade cantilever frequency and draw a horizontal line across the figure as shown. The intersection of this line with the ordinate, with the $\omega_c = \Omega$ line, and with the coupled frequency curve are the points of interest. For a light support system and $\omega_c = 0$, the rotor response is the free-free response of the rotor (including pylon mass). For $\omega_c = \Omega$, point A of Figure 3, the impedance of the pylon spring and system mass sum to zero. For this case, the rotor response is characteristically rigid body and a minimum. Several explanations for this phenomena have been theorized, but will not be pursued here. However, experimental data verify the existence of this minimum for multi degree-of-freedom as well as two degree-of-freedom support systems. At point B, the rotor speed is coincident with the coupled system frequency and resonance loads result. For large values of ω_c , the coupled blade frequency approaches the cantilever blade frequency and the rotor response approaches the blade cantilever response as a limit.

Figure 4 is similar for any choice of rotor speed and values of $\bar{\omega}$ less than 1.0. For values of $\bar{\omega}$ greater than 1.0 point B moves to the right for higher operating speeds and to the left for lower operating speeds with corresponding changes in the rotor response in the region between points A and B. For large inertia pylons, the coupled coincident natural frequency for $\bar{\omega} = 0$ approaches the cantilever blade frequency and the variation in inplane bending moment with pylon frequency ratio is shown by the dashed curve in Figure 4.

It is concluded that Figure 4 presents the total variation in rotor one-per-rev bending moment as a function of support system parameters for all rotor speeds less than the blade cantilever frequency. (Since support system parameters determine the magnitude of the rotor hub impedance, Figure 4 also presents the effect of hub impedance on rotor one-per-rev in-plane loads.) For support systems with frequency ratios less than 1.0, the rotor response will be less than or equal to the cantilever response. Support systems with frequency ratios greater than 1.0 will exhibit response greater than cantilever and should be avoided.

The addition of a mast bending degree-of-freedom changes the Coleman frequency diagram, the response of the rotor during run-up, and the coupled rotating frequency diagram (Figure 3). However, the variation in rotor one-per-rev inplane moment with hub impedance (support system parameters) is virtually the same as that given in Figure 4 for the two degree-of-freedom system. The principal difference is that the rotor response for pylon frequency ratios greater than point B are generally less than the cantilever response.

Method of Varying Parameters

For this discussion, the parameters of interest are the pylon support spring rate and the pylon mass. (Damping is neglected.) The choice of spring rate is in general limited to available hardware, while a mass variation is more easily attainable for any desirable increment by adding nonstructural weight to the system. The mass variation is defined in terms of increments of the ratio of rotor mass to pylon mass.

A portion of Figure 4, the rotor response for $\bar{\omega}$ equal to or less than 1.0, is reproduced in Figure 5a. In this case, the load reference is chosen as the free-free rotor blade response. Typical lines of constant pylon mass and constant pylon spring rate are indicated in the figure.

In Figure 5b, the rotor response is plotted as a function of the pylon mass ratio m with pylon spring rate as a parameter. The relative magnitudes of pylon spring rates and masses are chosen such that $K_1 < K_2 < K_3$ and $m_1 < m_2 < m_3$, and with constant increments from the minimum case. The value of K is the spring rate of the pylon at the rotor hub, while the mass ratio is the ratio of the effective pylon mass in the rotating system to the mass of the rotor when disconnected from the pylon. Thus, the presentation given in Figure 5b gives the effect of the pylon spring rate and mass on the rotor response in terms of the physical properties of these elements.

For a two degree-of-freedom isotropic system, the effective pylon mass is given by

$$m_{pe} = \frac{I_p + m_p r^2}{s^2}$$

where I_p is the pylon moment of inertia about the pylon center of gravity, cg , m_p is the mass of the pylon, r is the distance from the pylon cg to the pylon pivot point, and s is the distance from the pylon pivot point to the center of rotation of the rotor (hub center). The pylon mass ratio is then given by

$$\bar{m} = m_{pe}/m_R$$

where m_R is the total rotor mass.

TEST EQUIPMENT

Model Description

The test model, shown installed in the tunnel in Figure 6, is the same basic model described in reference 7 with a different rotor system installed. Various modifications to the model were required to accomplish the test objective. The following paragraphs describe the model as tested.

The test model is a single rotor configuration having a 292.6 centimeter diameter main rotor. The body has a maximum diameter of 51.0 centimeters. A fixed incidence horizontal stabilizer is attached to the tailboom structure to minimize the fuselage pitching moment.

Figure 7 is a schematic of the model and shows the relationship of the various component parts. Figure 8 gives the dimensional envelope for the model installation. The support frame of the model is constructed of heavy aluminum alloy plate. This frame attaches to the pitch plate and provides the model pitch axis. Model pitch change is affected by a remotely controlled linear actuator attached to the frame at one end and to the pitch plate at the other. The pitch plate is bolted to the NASA-Langley six-component balance (SP03R).

The model pylon assembly is attached to the support frame through a set of four elastomeric mounts (see Figure 7). Three sets of mounts are available, each set having a different spring rate, such that the hub impedance can be varied by changing the pylon mounts. The pylon assembly consists of the power train,

transmission, rotor shaft, controls system, hub, rotor blades, and pylon weights. This system was originally designed to represent a one-quarter scale AH-1G helicopter pylon and is too large and massive to scale accurately a one-fifth sized UH-1D pylon. Also, the model drive motors are installed as a part of the pylon resulting in an initial greater-than-scale pylon inertia. Thus, the hub impedance of the model is not a scaled representation of the full-scale hub impedance and only trends (not magnitudes) as established by an incremental impedance can be considered to be representative of full-scale rotor response. The pylon weights are designed to be installed in two equal increments. Each increment increases the pylon inertia an amount approximately equal to one-half the inertia of the rotor system (rotating coordinates) and results in a corresponding change in the hub impedance.

The rotor is powered by two variable-frequency, water-cooled electric motors each rated 37 kilowatts at 12,000 rpm. The motors are belted to a common input to the transmission assembly that drives the rotor. Motor rpm is reduced 14:1 ahead of the rotor shaft by a 5.4:1 belt reduction and a 2.6:1 gear reduction. This reduction is compatible with the requirement to maintain the full-scale advance ratio and advancing-tip Mach number during the model tests.

The rotor controls consist of a "rise-and-fall" swashplate, driven by pylon-based actuators, to vary the blade collective pitch and the lateral and longitudinal (fore-and-aft) cyclic requirements. All actuators are remotely controlled from a control console. The rotor control rates are each designed to be one-quarter of a degree per second for the rated 28-volt input to the control motors. These rates can be changed by varying the voltages to the motors.

A truss-type tubular steel tailboom attaches to the aft support frame and provides the structural support for the horizontal stabilizer and the tailboom fairing. The nose, pylon, and center-body fairings are attached directly to the support frame. Approximately 11 kilograms of lead are attached to the tailboom in the appropriate location to produce a fuselage that is free of resonant frequencies throughout the rotor operating range.

Rotor System

The model has a one-fifth size, dynamically similar UH-1D rotor system. The rotor diameter is 292.6 centimeters and the chord is a constant 10.7 centimeters. The blade uses an NACA 0012 airfoil section and has a -10.9 degrees of twist. The

basic blade construction is a bonded stainless steel spar encapsulated in aluminum honeycomb covered with a fiberglass shell. Ballast weights are bonded to the spar as required to obtain the scaled weight, center of gravity, and inertia at each segment. The rotor hub is geometrically and dynamically scaled insofar as practical. In order to adapt to the existing model mast (designed to be a one-quarter scale AH-1G), the center segment of the model UH-1D hub was allowed to be larger and stiffer than scale. This small deviation did not appreciably affect the rotor system frequencies. Figures 9 and 10 show the calculated frequency plots for the one-fifth scale UH-1D rotor system as tested. (Reference 8.) Collective modes as referred to in Figure 9 are those blade bending modes excited by collective pitch inputs; these are the flapwise symmetric modes and chordwise asymmetric modes. Cyclic modes, Figure 10, refers to the blade bending modes excited by cyclic pitch inputs; these modes are the asymmetric flapwise and symmetric chordwise modes.

Scaling Criteria

Scaling parameters were determined by maintaining the model rotor advance ratio, μ , and advancing-tip Mach number, $M(1.0, 90.)$, numerically equal to the full-scale rotor values. Table I presents the major scaling parameters used in designing the scaled rotor system. The relationship between model and full-scale values of several frequently used nondimensional ratios is given in this table.

Instrumentation System

Instrumentation is installed on the model to provide a measurement of the model aerodynamic parameters, rotor and control loads, rotor rpm and azimuth, and various position data. Table II is a list of the instrumentation available on the model.

The six force and moment components of the entire model (rotor and fuselage) are measured by a balance (SP03R) provided and calibrated by the NASA-Langley Research Center. The other individual component loads and moments are obtained from strain gage bridges. Each foil-type strain gage composes one arm of a four active arm bridge. Bridge sensitivities were determined by applying known incremental loads through the expected operating range. The load-equivalent electrical output was obtained using a precision resistor shunt on one leg of the bridge.

All control positions and the fuselage pitch attitude are obtained from potentiometers used as one arm of a four-arm bridge circuit. Each position is equipped with dual sensing circuits, one for recording and one for monitoring. Flapping is measured by a potentiometer mounted on the mast and mechanically geared to the rotor hub. All position sensors were calibrated through the full operating range.

All data, except the six-component balance and tunnel information, were recorded on magnetic tape using a contractor-furnished data acquisition system. This system was activated only when prime data were to be recorded. A separate NASA tape system recorded the same data and ran continuously when the model was operating to provide a record of any incident or emergency operation. This tape was periodically erased and reused. All tunnel condition data and the model aerodynamic data (balance data, control positions, mast torque, and rpm) were recorded and reduced by NASA-Langley.

TEST PROGRAM AND PROCEDURES

The test program was conducted in two phases. Phase I consisted of shake testing the pylon to determine the impedance of each of the nine configurations to be tested in the tunnel. Phase II was the tunnel tests of each hub impedance configuration to obtain the rotor oscillatory loads at common test conditions.

Shake Test Procedure

Shake tests were conducted prior to tunnel entry to define the hub impedance (or equivalent) of each spring-mass combination. The model pylon was assembled in the build-up area of the Transonic Dynamics Tunnel. The basic model was mounted on the balance and through the balance to a rigid calibration table in the Calibration Laboratory. The pylon was shaken both laterally and longitudinally at the rotor hub with an electromagnetic shaker suspended and supported by three cables attached to a ceiling-mounted hoist (see Figure 11).

A mechanical impedance head was installed between the shaker and the hub to measure the force and acceleration of the shaker. An additional accelerometer was attached directly to the hub, and its output and the force from the impedance head were transmitted to the instrumentation system and plotted versus frequency. The shaker, impedance head, shaker controls, and data acquisition system were provided and calibrated by NASA-Langley. The controls and data acquisition system are

shown in Figure 12. An instrumentation schematic is shown in Figure 13.

Each set of mounts (three sets) were shaken with each of three pylon weights. The weights shaken were the actual tested pylon weight, actual plus 22.7 kilograms, and actual plus 45.4 kilograms. The addition of 36.8 kilograms of this weight increases the pylon inertia an amount equal to the pylon inertia contributed by the rotor system. A set of pylon mounts consists of four individual mounts each having the same spring rate. The individual spring rates used for the three sets were calibrated to be 1800, 4700, and 5000 newtons per centimeter. The equivalent pylon spring rates at the rotor hub (K_p) for these three sets of mounts were 400, 1050, and 1120 newtons per centimeter, respectively. Each spring-mass combination was shaken over a frequency range from 5 to 70 hertz both laterally and longitudinally with the rotor blades perpendicular to the direction of shaking in all cases. This frequency range included the operating frequencies and major harmonics of interest anticipated during the tunnel test.

Tunnel Test Procedure

The tunnel test provided data to assess the effect of hub impedance on rotor oscillatory loads. The test consisted of sweeping collective pitch at two operating conditions and two mast angles for each of the nine spring-mass combinations discussed in the previous section. The same collective pitch angles, shaft angles, rpms, and velocities were tested for each impedance configuration. The test procedure was to set the shaft angle and collective pitch to the selected angles, bring the model rpm to the desired value, then bring the tunnel to the proper velocity and record the data. The collective pitch was then varied incrementally and data were recorded at each collective angle. Shaft angle was repositioned and the collective sweep was repeated. Rotor rpm and tunnel velocity were reset to the new flight condition and the above collective pitch and shaft angle sequence repeated for each impedance configuration.

TEST RESULTS

Ground Vibration Tests

Ground vibration tests were conducted at the Bell Helicopter Engineering Research Laboratory and at the NASA facilities

at Langley Field, Virginia. These tests were conducted to determine

- rotor free-free natural frequencies, both vertical and inplane, and inplane hub impedance (due to rotor alone)
- pylon natural frequencies and inplane hub impedance (due to pylon alone)
- coupled rotor and pylon natural frequencies and inplane hub impedance (total system)

for comparison of analytical and test results. The results of these tests are discussed below.

The variation of the pylon frequencies, rotor on and off, and the coupled inplane rotor frequency with pylon mass ratio and pylon spring rate is presented in Figures 14 and 15 for longitudinal and lateral vibration tests, respectively. A comparison of computed and measured pylon frequencies for the configurations tested is given in Table III. Good agreement between computed values and test results is shown.

The pylon whirl frequencies are identified by the coincidence of the fixed system pylon frequency with rotor operational speed (i.e., $\omega_p = \Omega$). These coincidences for all configurations tested are shown in Figure 16. Impedance tests were conducted at 650 rpm and 720 rpm. At 650 rpm, a lateral pylon whirl frequency is located within 3 percent of the rotor operating speed for three of the configurations tested. Although some increases in loads are noted later, no detrimental effects of this coincident frequency were shown during the test.

A summary of all system frequencies observed during the ground vibration tests conducted at the Langley Field facility is given in Tables IV and V for longitudinal and lateral tests, respectively. Fixed system and rotor modes are easily identified by comparison of the rotor-on and rotor-off data. Modal identifications, where known, are indicated in the table.

A summary of vibration tests conducted at Bell Helicopter Company and at Langley Field to determine the rotor natural frequencies is given in Table VI. Good agreement between computed data (also given in Table VI) and test data is demonstrated. (See reference 8 for method of computation.)

Tunnel Tests

Tests were conducted in the NASA-Langley Transonic Dynamics Tunnel in a freon atmosphere to determine the effect of hub impedance on the inplane oscillatory response of the rotor. These tests were conducted for nine combinations of pylon inertia and spring rate at four rpm/airspeed operating conditions. The results of these tests are presented in Figures 17 through 21.

In order to simplify the following discussion, the operating conditions will be identified by the code numbers given below:

	<u>Rotor Speed</u>	<u>Tunnel Speed</u>
Code 1	650 rpm	20.7 m/sec
Code 2	650 rpm	32.3 m/sec
Code 3	720 rpm	20.7 m/sec
Code 4	720 rpm	32.3 m/sec

A comparison of computed (ref. 8) and measured one-per-rev inplane bending moments at the 15.6 percent blade radius is given in Figure 17 for a Code 3 operating condition at a root collective pitch of 16 degrees. (The data of Figure 17 through 20 are presented for the 15.6 percent blade radius station which is the most inboard blade station that was instrumented for bending moments. As shown in Figure 21, this blade station experienced the maximum loads response.) Computed and measured data for the 1050 and 1120 newtons per centimeter spring rates compare favorably, except for the low pylon mass ratio. The difference in the measured and computed data for these spring rates at the minimum mass ratio is attributed to coupling of the pylon/rotor system with a support mode of the balance or tunnel floor, which was not accounted for in the analysis. As pylon mass increases the effect of the additional spring decreases and consequently the difference between the coupled and measured data decreases at the higher mass ratios. A significant difference between computed and measured data is shown for the soft-spring rate at all pylon mass ratios tested. The reason for this large (relative to the other spring rates) difference at this spring rate is not discernable from the data available.

The difference in magnitude between the computed and measured data for all cases is attributed, at least in part, to scale effects. Rotor aerodynamic coefficients for the model scale Reynolds number were not available for use in the computations. Therefore, full-scale Reynolds number coefficients

were used in the analysis. Thus, the rotor aerodynamic performance and loads were not properly simulated.

The overall and one-per-rev inplane oscillatory blade bending moment at the 15.6 percent blade radius as a function of pylon mass ratio and pylon spring rate is given in Figures 18 through 20 for shaft angles of -2 and -6 degrees, at a root collective blade angle of 16 degrees. (See Appendix for other collective angles.) The variation in load with pylon parameters generally follows the anticipated trends as shown in Figure 5. The ratio of measured maximum to minimum one-per-rev moment for these cases (including Figure 17 data) varies from 1.8 to 2.0 with the lower values occurring for low-lift conditions. The lift varied from approximately 710 newtons for Code 2 tests at a -6 degree shaft angle to approximately 1620 newtons for Code 3 tests at a -2 degree shaft angle. For the approximate range of parameters tested, a maximum to minimum load ratio of 1.6 was predicted for 1330 newtons lift in a Code 4 operating condition.

The predicted maximum one-per-rev inplane moment, as shown in Figure 17, occurs for the pylon configuration with coupled natural frequency farthest from coincidence with the rotor operating speed (i.e., for the soft spring/heavy mass case). In addition, the predicted minimum one-per-rev inplane moment occurs for the pylon configuration with a coupled natural frequency nearest coincidence with the rotor operating speed (i.e., for the stiff spring/light mass case). This seemingly contradictory frequency effect is entirely consistent with expected results as discussed under the section entitled Effects of Variation in Hub Impedance. It can be seen in Figure 3 that for a two degree-of-freedom pylon, the uncoupled coincident natural frequency, ω_c , is always greater than the coupled natural frequency, ω_{pc} . As ω_c increases ω_{pc} also increases. As shown in Figure 4, the rotor response decreases as ω_c and/or ω_{pc} increases for all cases where ω_c/Ω is less than 1.0.

Although the data follow the predicted trends, several inconsistencies are observed which warrant further comment. At 720 rpm, the measured loads for the stiff and medium spring rates and minimum inertia configuration (Figures 17 and 18) were greater than anticipated and deviate significantly from the predictions (Figure 17). Wherein minimum response was anticipated for these configurations, the measured loads were greater than for the soft-spring rate with the same pylon inertia. This deviation is apparently independent of airspeed and load conditions, and is attributed to the coupling of the rotor and pylon with a support mode of the balance and/or tunnel floor, resulting in a lower coupled inplane rotor frequency and consequently increased rotor response.

At 650 rpm, the measured one-per-rev loads for the soft-spring rate/high inertia configuration (Figures 19 and 20) were significantly lower than anticipated. Wherein a maximum load condition was expected, the measured response for all airspeed/airload conditions was less than for either of the other spring rates tested at the same pylon inertia. Based on available data, no reasonable explanation can be given for this deviation.

It is also noted, that at 650 rpm, the measured loads for the stiff-spring rate configuration with light and medium inertia are higher than the loads for the standard spring rate (1050 newtons per centimeter) configurations with the same inertia. A review of Figure 16 shows that a lateral pylon whirl frequency is located very near the operating speed for these two configurations. Slight excitation of these frequencies, possibly due to small out-of-balance forces, could easily result in the load increases observed.

A comparison of the overall and one-per-rev inplane bending moments in Figures 19 and 20 verifies that the variation in moment is due primarily to variation in the one-per-rev component. This is further substantiated in Figure 21, in which the spanwise distribution of inplane and flapwise bending moments at the principal rotor harmonics is presented for the maximum and minimum hub impedance cases for the Code 3 test conditions. For the inplane moments, the values at three-per-rev and five-per-rev are extremely small and the one-per-rev component is the only significant response at all span locations. These same trends are true for all impedance values and test conditions investigated. (See Appendix.)

Figure 21 shows that inplane hub impedance variation has little or no effect on flapwise bending moments. This is the expected result since the vertical hub impedance is essentially invariant for the range of pylon parameters investigated. Examination of the data contained in the Appendix shows that this trend is true for all flapwise and torsional bending moments and axial pitch link loads measured at all test conditions.

CONCLUSIONS

The following conclusions can be drawn as a result of these tests:

- Inplane response changes by factors as large as 2.0 are realized for the range of pylon parameters tested. Thus, for two-bladed rotor systems, correlation of either wind-tunnel or full-scale inplane blade load

data with theory is not possible if inplane hub impedance effects are not included in the analysis.

- Good agreement, with respect to trends, is demonstrated between analysis and test.
- Inplane impedance parameters do not influence out-of-plane or torsional rotor responses.

Tests conducted to date have covered only a small portion of the pylon impedance range and have been basically related to pylon configurations presently operating in the field. Modern support systems are becoming increasingly complex, and vertical as well as inplane hub impedance effects are becoming more crucial for the two-bladed rotor system, both from the standpoint of rotor design and rotor response prediction. It is desirable that better methods for determining as well as using impedance parameters be developed.

Although the basic concepts of hub impedance are established, the effects of damping, inplane anisotropy, vertical impedance, and other parameters are not fully understood and merit further investigation.

REFERENCES

1. Coleman, Robert P.; and Feingold, Arnold M.: Theory of Self-Excited Mechanical Oscillations of Helicopter Rotors with Hinged Blades. NACA TR 1351, 1958.
2. Brooks, George W.: The Mechanical Instability and Forced Response of Rotors on Multiple-Degree-of-Freedom Supports. PhD Thesis, Princeton University, 1961.
3. Thorn, Richard P.: The Mobility Method. Machine Design Magazine, A Penton Publication, December, 1959.
4. Harris, Cyril M.; and Crede, Charles E.: Shock and Vibration Handbook, Vol. 1, McGraw-Hill Book Company, 1961.
5. Church, Austin H.: Mechanical Vibrations. Second ed., John Wiley and Sons, Inc., 1963.
6. White, James A.; and Lee, Charles D.: Effect of Hub Impedance on the Inplane Oscillatory Blade Loads of a Two-Bladed Rotor System. Paper presented at the American Helicopter Society Thirtieth Annual National Forum, Washington, D. C., May, 1974.
7. Lee, Charles; Charles, Bruce; and Kidd, David: Wind-Tunnel Investigation of a Quarter-Scale Two-Bladed High-Performance Rotor in a Freon Atmosphere. USAAVLABS TR 70-58, 1971.
8. Blankenship, B. L.; and Harvey, K. W.: A Digital Analysis for Helicopter Performance and Rotor Blade Bending Moments. Journal of the American Helicopter Society, Vol. 7 No. 4, October, 1962.

TABLE I. SCALING FACTORS

Item	Scale Factor, S	
Length	λ	0.200
Mass	$\rho\lambda^3$	0.027
Time	$2.272\lambda T^{-1/2}$	0.445
Mach Number	1/1	1.000
Reynolds Number	$.440\lambda\rho\mu'T^{1/2}$	0.419
Froude Number	$.194\lambda^{-1}T$	1.000
Lock Number	1/1	1.000
Force, Weight	$.194\lambda^2\rho T$	0.027
Velocity	$.440T^{1/2}$	0.449
Acceleration	$.194\lambda^{-1}T$	1.011
Frequency	$.440\lambda^{-1}T^{1/2}$	2.246
Angular Velocity	$.440\lambda^{-1}T^{1/2}$	2.246
Angular Acceleration	$.194\lambda^{-2}T$	5.054
Moduli, Pressure, Stress	$.194\rho T$	0.680
Moment, Torque	$.194\lambda^3\rho T$	0.0054
Power	$.085\lambda^2\rho T^{3/2}$	0.0122
Mass Moment of Inertia	$\lambda^5\rho$	0.0011
Area Moment of Inertia	λ^4	0.0016
Stiffness	$.194\lambda^4\rho T$	0.0011

Model Value = \hat{S} x Full Scale Value

λ = Model Length/Full Scale Length = 0.20

$\rho = \rho_M/\rho_{FS} = 4.123/1.226 = 3.364^*$

$\mu' = \mu'_{FS}/\mu'_M = \frac{17.91 \times 10^{-6}}{12.93 \times 10^{-6}} = 1.385^*$

$T = T_M/T_{FS} = 305.6K/293.3K = 1.042^*$

$\left(\frac{\gamma_{FS}^{R_{FS}}}{\gamma_M^{R_M}}\right)^{1/2} = \left(\frac{1.4 \times 88.52}{1.13 \times 21.24}\right)^{1/2} = 2.272$

*Typical values based on Test Data.

TABLE II. MODEL INSTRUMENTATION LIST

Item	Transducer Location	Transducer Type
Lift	Model Mount	SP03R Balance
Drag	Model Mount	SP03R Balance
Side Force	Model Mount	SP03R Balance
Pitching Moment	Model Mount	SP03R Balance
Rolling Moment	Model Mount	SP03R Balance
Yawing Moment	Model Mount	SP03R Balance
F/A Cyclic Position	Control System	Potentiometer
Lateral Cyclic Position	Control System	Potentiometer
Collective Pitch Position	Control System	Potentiometer
Mast Pitch Position	Pitch Actuator	Potentiometer
Mast Torque	Rotor Mast	Strain Gage
Flapwise Bending Moment	Blade Sta 9.0	Strain Gage
Flapwise Bending Moment	Blade Sta 16.6	Strain Gage
Flapwise Bending Moment	Blade Sta 27.6	Strain Gage
Flapwise Bending Moment	Blade Sta 34.0	Strain Gage
Chordwise Bending Moment	Blade Sta 9.0	Strain Gage
Chordwise Bending Moment	Blade Sta 16.6	Strain Gage
Chordwise Bending Moment	Blade Sta 27.6	Strain Gage
Chordwise Bending Moment	Blade Sta 34.0	Strain Gage
Torsional Bending Moment	Blade Sta 9.0	Strain Gage
Torsional Bending Moment	Blade Sta 27.6	Strain Gage
Pitch Link Load	Pitch Link	Strain Gage
Flapping Position	Rotor Hub	Potentiometer
Rotor Azimuth Position	Rotor Mast	Magnetic P/U
Rotor Rotational Speed	Rotor Mast	Magnetic P/U
Pylon Pitch Position	Pylon	Strain Gage
Pylon Roll Position	Pylon	Strain Gage
Pylon Acceleration	Pylon	Accelerometer
Fuselage Acceleration	Tailboom	Accelerometer
Drive Train Temperatures*	Power Train	Thermocouples

*Motors, drive train bearings, and transmission temperatures were monitored on a cycling temperature recorder.

TABLE III. COMPARISON OF COMPUTED AND MEASURED PYLON NATURAL FREQUENCIES

K_p (N/cm)	$\frac{m_p e}{m_R}$	Rotor	Lateral			Longitudinal		
			Computed	BHC Test	NASA Test	Computed	BHC Test	NASA Test
400	1.98	On	7.6	7.6	8.0	7.4	7.3	7.7
400	2.66	On	7.1	7.1	7.4	6.9	7.1	7.3
400	3.35	On	6.7	6.9	6.9	6.4	6.3	6.8
1050	1.98	On	10.7	10.8	10.5	10.3	8.4	8.7
1050	2.66	On	9.8	-	10.0	9.6	-	8.4
1050	3.35	On	9.2	-	9.4	8.9	-	8.0
1120	1.98	On	11.1	11.0	11.1	10.6	8.8	9.3
1120	2.66	On	10.1	-	10.4	9.8	-	9.0
1120	3.35	On	9.5	-	10.0	9.1	-	8.7
400	1.98	Off	9.1	9.2	9.0	8.5	8.6	8.9
400	2.66	Off	8.2	8.4	8.0	7.8	8.4	8.0
400	3.35	Off	7.3	7.5	7.2	7.1	8.1	7.8
1050	1.98	Off	12.8	12.2	12.7	12.1	10.1	9.9
1050	2.66	Off	11.2	-	11.4	10.8	-	9.4
1050	3.35	Off	10.2	-	10.5	9.9	-	8.8
1120	1.98	Off	13.2	13.4	13.8	12.4	10.6	10.8
1120	2.66	Off	11.6	-	12.6	11.1	-	10.3
1120	3.35	Off	10.5	-	11.7	10.2	-	9.6

TABLE IV. MODEL UH-1D 1/5 SCALE ROTOR - LONGITUDINAL SHAKE TESTS

Run No.	K_p (N/cm)	m_p/m_R	Rotor	Pylon Fore & Aft	1st Blade Torsion	1st Fuselage Vertical	1st Inplane Symmetric	Support Fore & Aft	3rd Flapwise Asymmetric	Fuselage Nose Vertical
18	1120	1.98	Off	10.9	-	18.5	-	20.8	27.0	36.3
7	1050	1.98	Off	10.0	-	17.0	-	19.2	-	34.4
8	400	1.98	Off	8.9	-	14.2	-	19.0	27.3	32.4
9	400	2.66	Off	8.0	-	14.0	-	18.8	27.0	31.7
10	400	3.35	Off	7.4	-	14.0	-	19.1	27.1	30.9
11	400	3.35	Off	7.4	-	14.0	-	19.8	26.6	31.1
5	1050	3.35	Off	8.9	-	16.1	-	19.8	-	33.8
17	1120	3.35	Off	9.7	-	17.4	-	20.3	27.8	35.2
15	1120	1.98	On	9.3	12.0	15.2	18.7	20.7	27.5	34.9
3c	1050	1.98	On	8.8	11.5	14.7	18.4	20.0	27.5	34.3
14	400	1.98	On	7.8	12.2	14.5	17.6	19.8	27.2	32.2
13	400	2.66	On	7.3	12.2	14.8	17.3	20.0	27.2	32.3
12	400	3.35	On	6.9	12.2	14.7	17.2	20.0	27.2	31.3
4	1050	3.35	On	8.0	11.8	14.7	17.7	19.8	27.2	33.6
16	1120	3.35	On	8.8	-	15.6	18.0	20.2	27.5	34.0




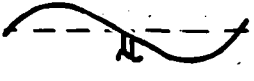

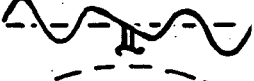
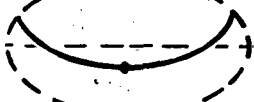

TABLE IV. Continued

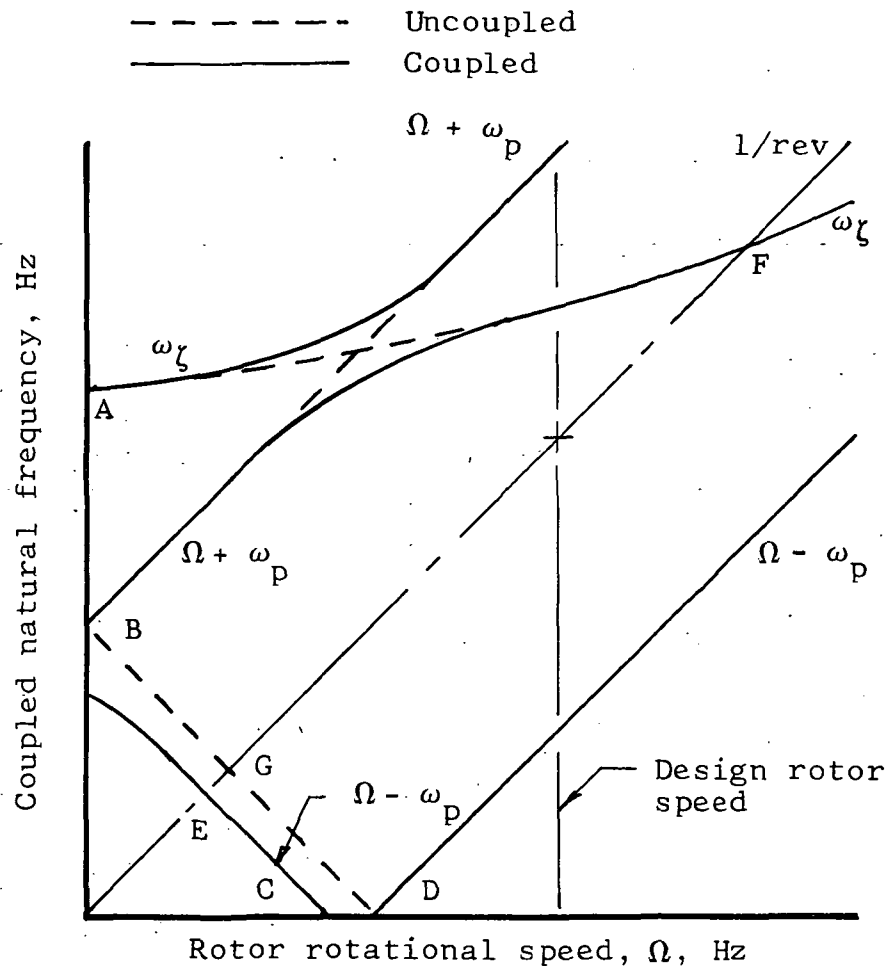
Run No.	K_p (N/cm)	m_p/m_R	Rotor	2nd Blade Torsion	Motor Pitch	2nd Fuselage Vertical	3rd Flapwise Symmetric	No I.D.	4th Flapwise Asymmetric	1st Inplane Asymmetric
18	1120	1.98	Off	-	45.0	52.3	-	61.5	-	-
7	1050	1.98	Off	-	43.0	51.5	-	60.7	-	-
8	400	1.98	Off	-	38.0	49.8	-	59.8	-	-
9	400	2.66	Off	-	37.0	47.8	-	59.5	-	-
10	400	3.35	Off	-	36.3	46.4	-	60.0	-	-
11	400	3.35	Off	-	36.5	45.8	-	57.0	-	-
5	1050	3.35	Off	-	41.1	47.5	-	-	-	-
17	1120	3.35	Off	-	42.3	48.5	-	59.2	-	-
15	1120	1.98	On	36.8	43.3	51.0	56.9	61.5	63.0	65.5
3c	1050	1.98	On	36.5	42.0	49.0	49.8	61.0	63.3	65.5
14	400	1.98	On	33.0	38.8	47.3	50.0	58.0	60.8	65.5
13	400	2.66	On	-	38.2	45.5	51.2	51.5	59.5	65.5
12	400	3.35	On	35.8	37.6	44.0	48.9	55.9	60.0	64.6
4	1050	3.35	On	35.8	40.0	46.5	-	-	-	-
16	1120	3.35	On	36.1	41.3	46.8	49.0	59.3	61.5	64.2

TABLE V. MODEL UH-1D 1/5 SCALE ROTOR - LATERAL SHAKE TESTS

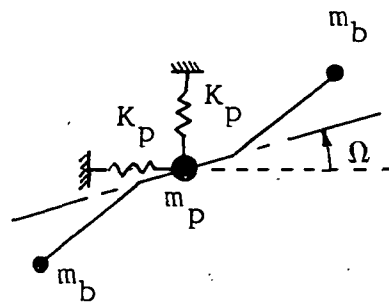
Run No.	K_p (N/cm)	m_p/m_r	Rotor	Pylon Lateral	1st Inplane Symmetric	1st Fuselage Lateral	Support Lateral	Fuselage Nose Lateral	Rotor Torsion	Motor Yaw	2nd Fuselage Lateral	3rd Flapwise Symmetric	No I.D.
20	1120	1.98	Off	13.8	-	21.1	22.7	32.2	-	39.5	45.4	-	57.7
30	1050	1.98	Off	12.7	-	21.0	23.5	33.6	-	38.4	45.0	-	56.0
29	400	1.98	Off	9.0	-	19.8	23.0	32.0	-	36.5	48.0	-	54.8
28	400	2.66	Off	8.0	-	19.8	22.9	31.1	-	36.2	47.5	-	54.8
27	400	3.35	Off	7.1	-	19.1	22.6	29.7	-	35.5	46.9	-	54.8
31	1050	3.35	Off	10.5	-	20.0	23.0	33.2	-	36.1	43.0	-	53.0
21	1120	3.35	Off	11.7	-	20.2	22.8	33.2	-	37.0	43.9	-	55.0
23	1120	1.98	On	11.1	17.6	21.2	23.0	33.2	35.4	38.5	45.0	53.2	-
33	1050	1.98	On	10.5	17.5	21.0	23.0	32.9	34.9	37.2	44.5	53.0	-
24	400	1.98	On	8.0	17.4	19.9	23.1	31.8	34.0	36.1	47.3	54.0	-
25	400	2.66	On	7.4	17.2	19.9	23.0	30.8	33.0	36.0	46.2	53.0	-
26	400	3.35	On	7.0	17.0	19.2	22.5	29.3	33.5	34.9	46.2	53.0	-
32	1050	3.35	On	9.4	17.2	20.0	23.2	30.0	33.0	35.9	47.0	54.0	-
22	1120	3.35	On	10.0	17.8	20.1	23.2	32.8	34.5	36.2	47.1	53.5	-

TABLE VI. COMPARISON OF COMPUTED AND MEASURED
FREE-FREE ROTOR NATURAL FREQUENCIES

Mode	Mode Shape	Frequencies - Hz				
		Computed	BHC Test	NASA Test		
			①	②	③	④
1st Flapwise Symmetric		2.7	2.7	-	-	-
2nd Flapwise Symmetric		19.3	20.7	19.9	-	20.0
3rd Flapwise Symmetric		51.7	53.0	52.0	-	-
2nd Flapwise Asymmetric		8.7	8.7	7.8	8.0	7.9
3rd Flapwise Asymmetric		27.8	27.8	27.8	27.7	26.9
4th Flapwise Asymmetric		61.0	61.0	62.0	61.0	-
1st Inplane Symmetric		20.6	*19.4	19.3	20.0	19.2
2nd Inplane Asymmetric		62.3	-	57.5	57.8	57.8
<u>Tests</u> ① Vertical Excitation at Rotor Hub (Vertical Acceleration at Blade Tip) ② Inplane Excitation of Rotor and Pylon at Rotor Hub (Vertical Acceleration at Blade Tip) ③ Inplane Excitation at Blade Tip (Single Exciter) - Inplane Acceleration at Rotor Hub ④ Inplane Excitation at Each Blade Tip - Inplane Acceleration at Rotor Hub * Inplane Excitation at Rotor Hub (Inplane Acceleration at Rotor Hub)						



a) Coleman Frequency Diagram



b) Analytical Model

Figure 1. Characteristics of Rotating System Natural Frequencies with Rotor Rotational Speed

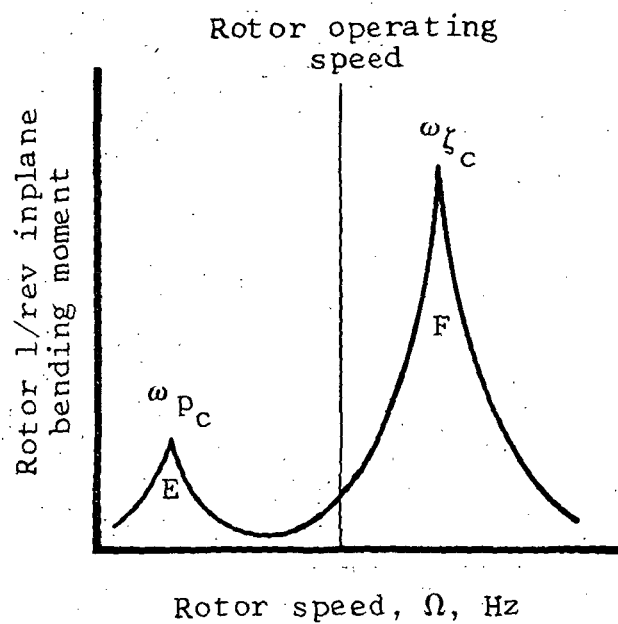


Figure 2. One-per-rev Inplane Rotor Response for a Typical Pylon/Rotor Coupled System During Normal Run-Up.

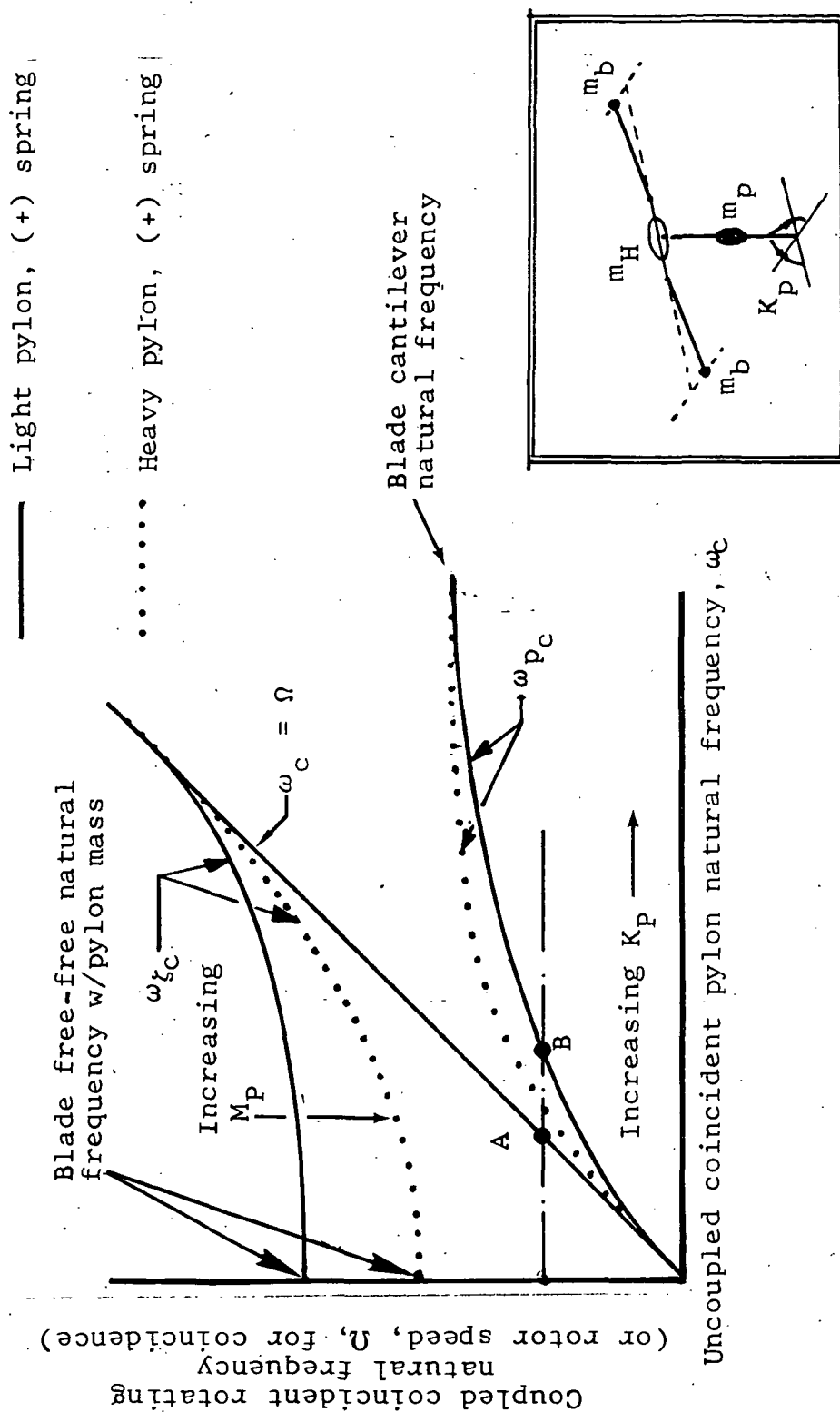


Figure 3. Coupled Coincident Rotating Natural Frequency Variation With Pylon Mass and Spring Rate

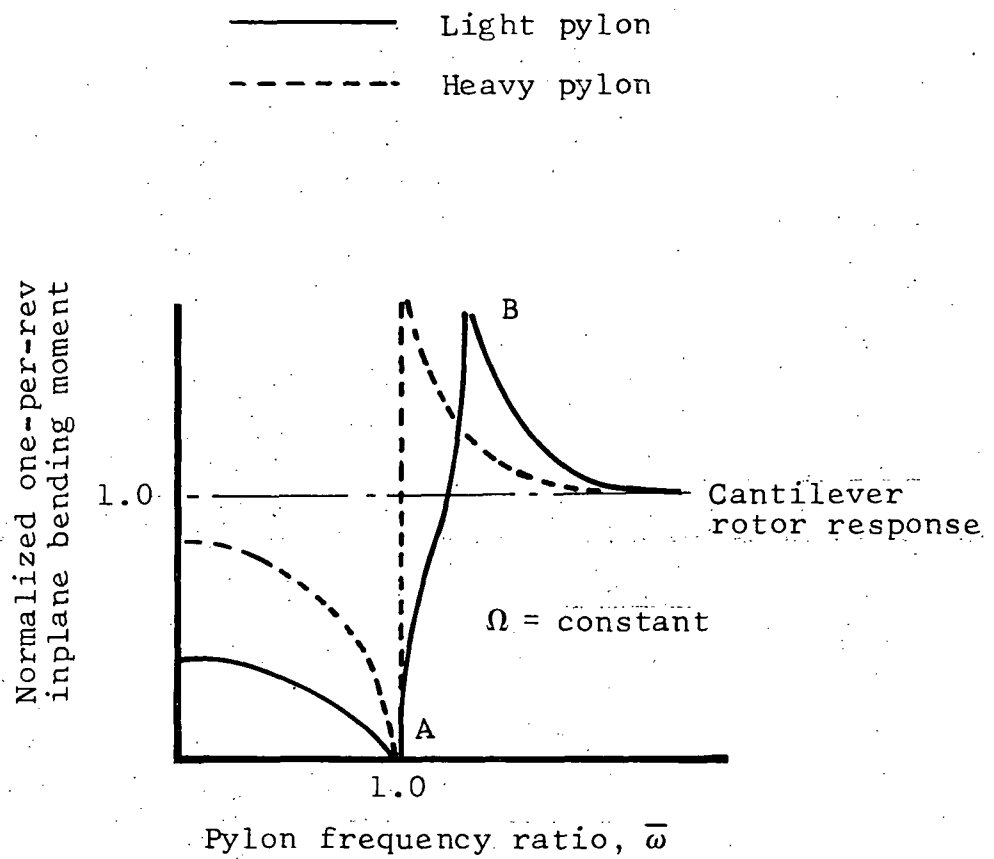


Figure 4. One-per-rev Inplane Rotor Response Variation With Pylon Frequency Ratio

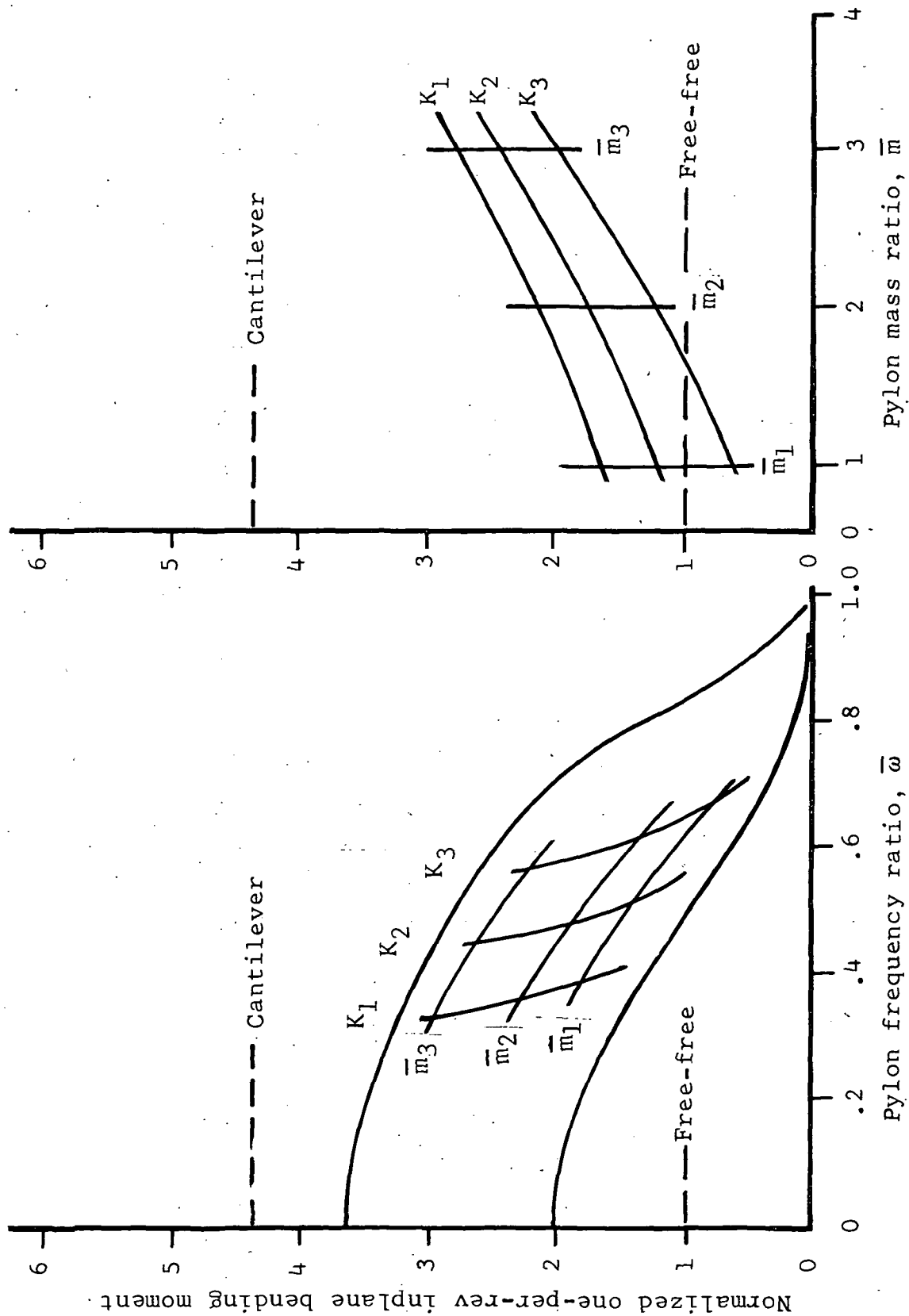


Figure 5. Variation of Normalized One-per-rev Inplane Bending Moment With a) Pylon Frequency Ratio, b) Pylon Mass Ratio

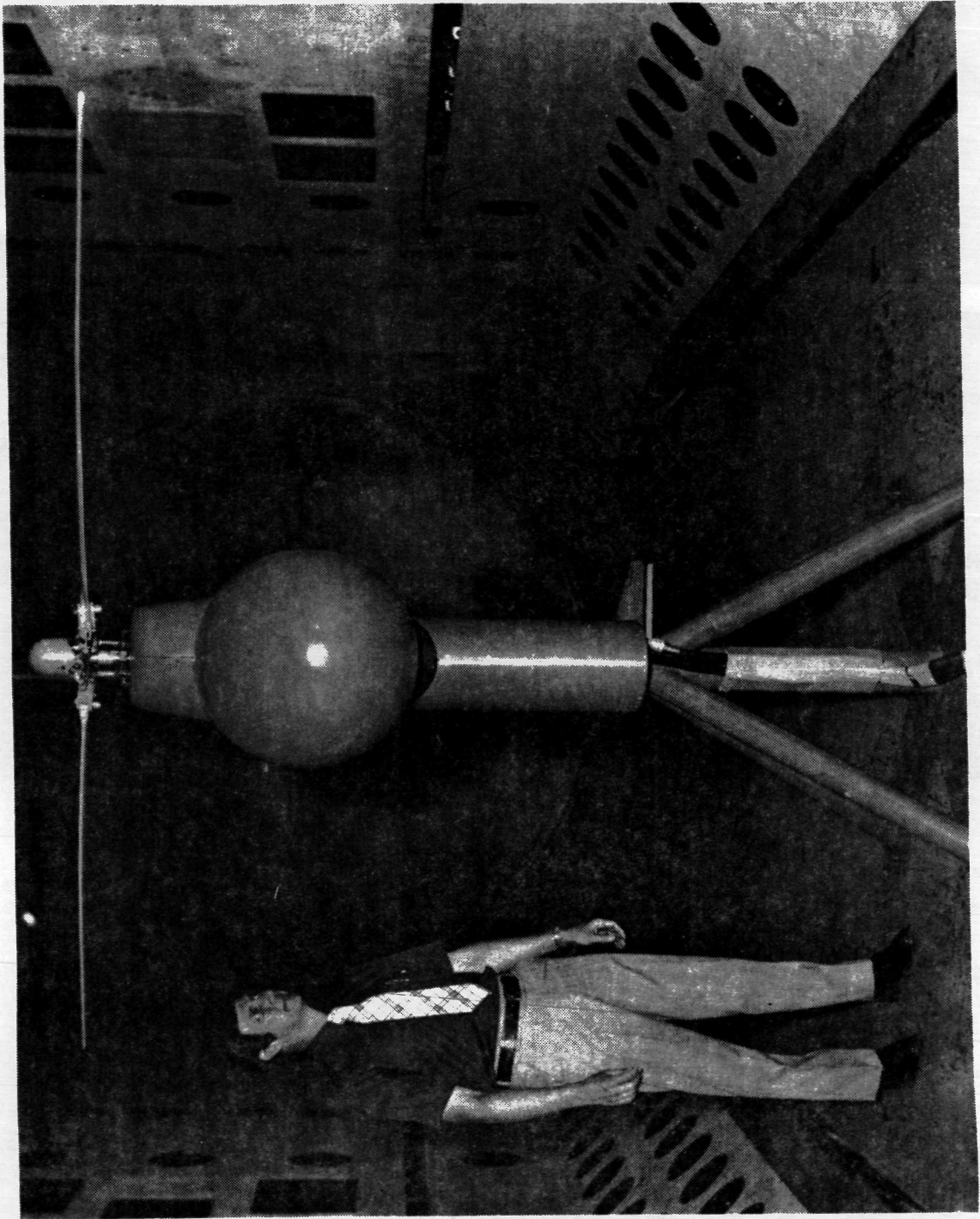


Figure 6. Model Installed in Tunnel.

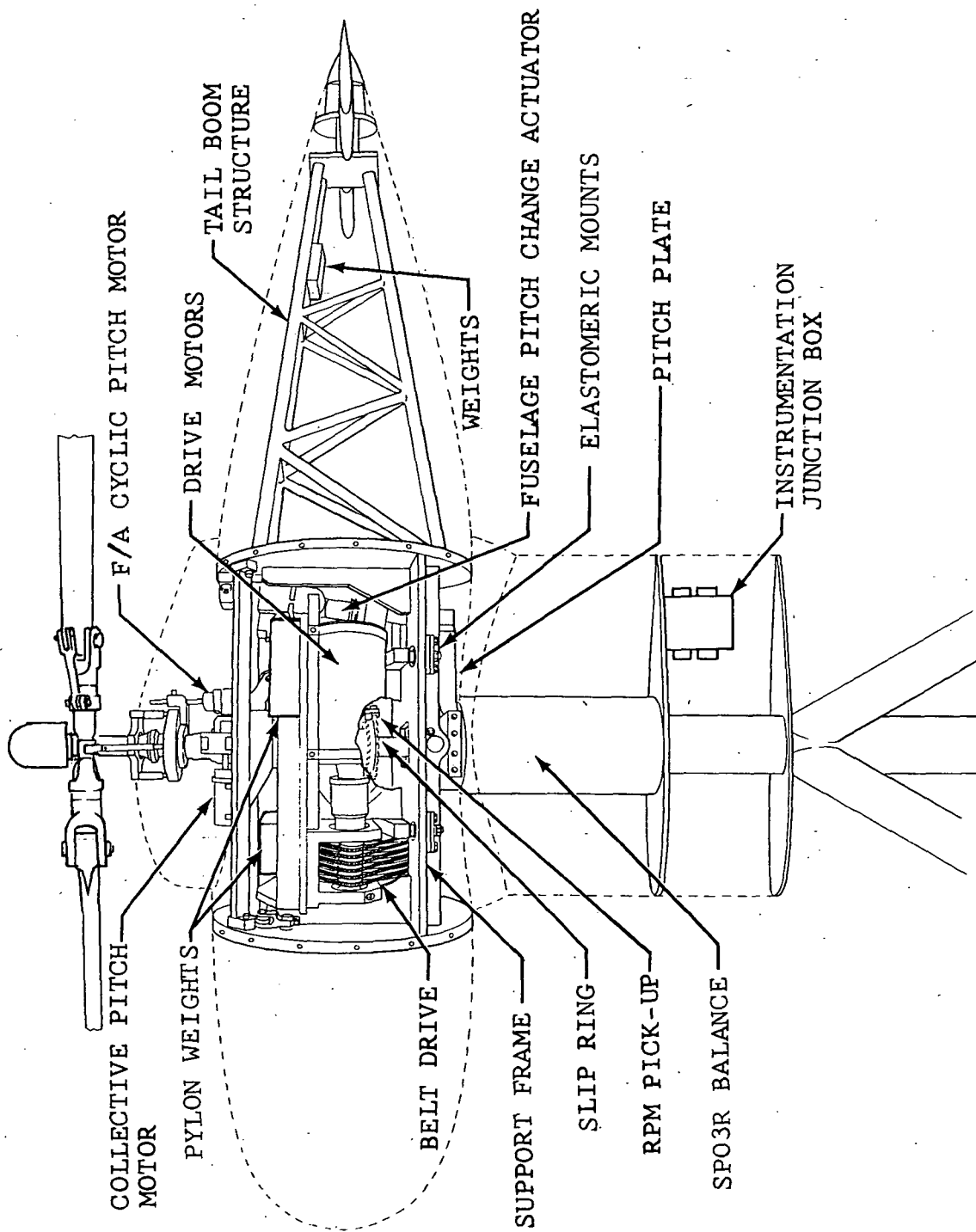


Figure 7. Model Schematic.

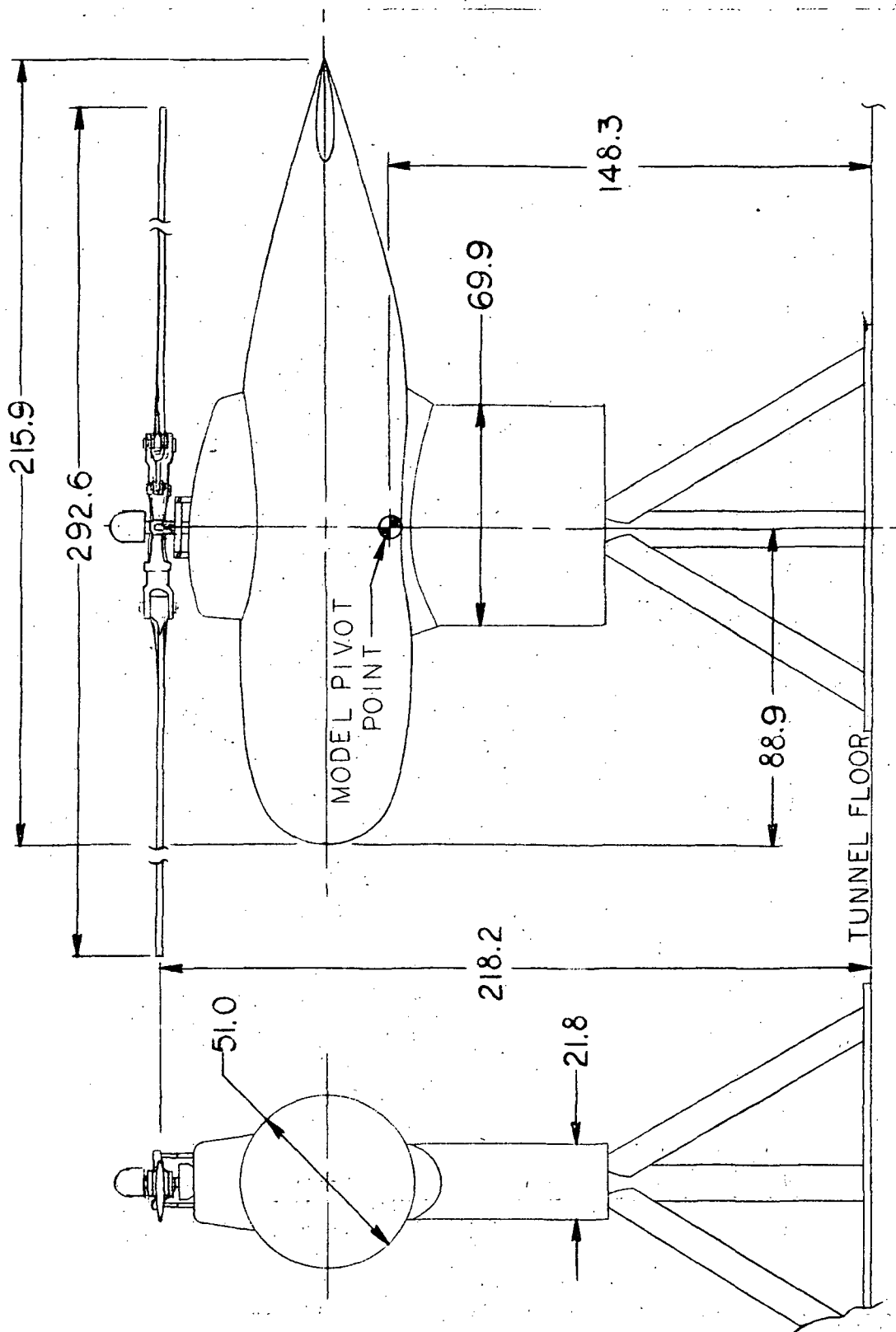


Figure 8. Tunnel Installation Dimensional Data.
All Dimensions in Centimeters.

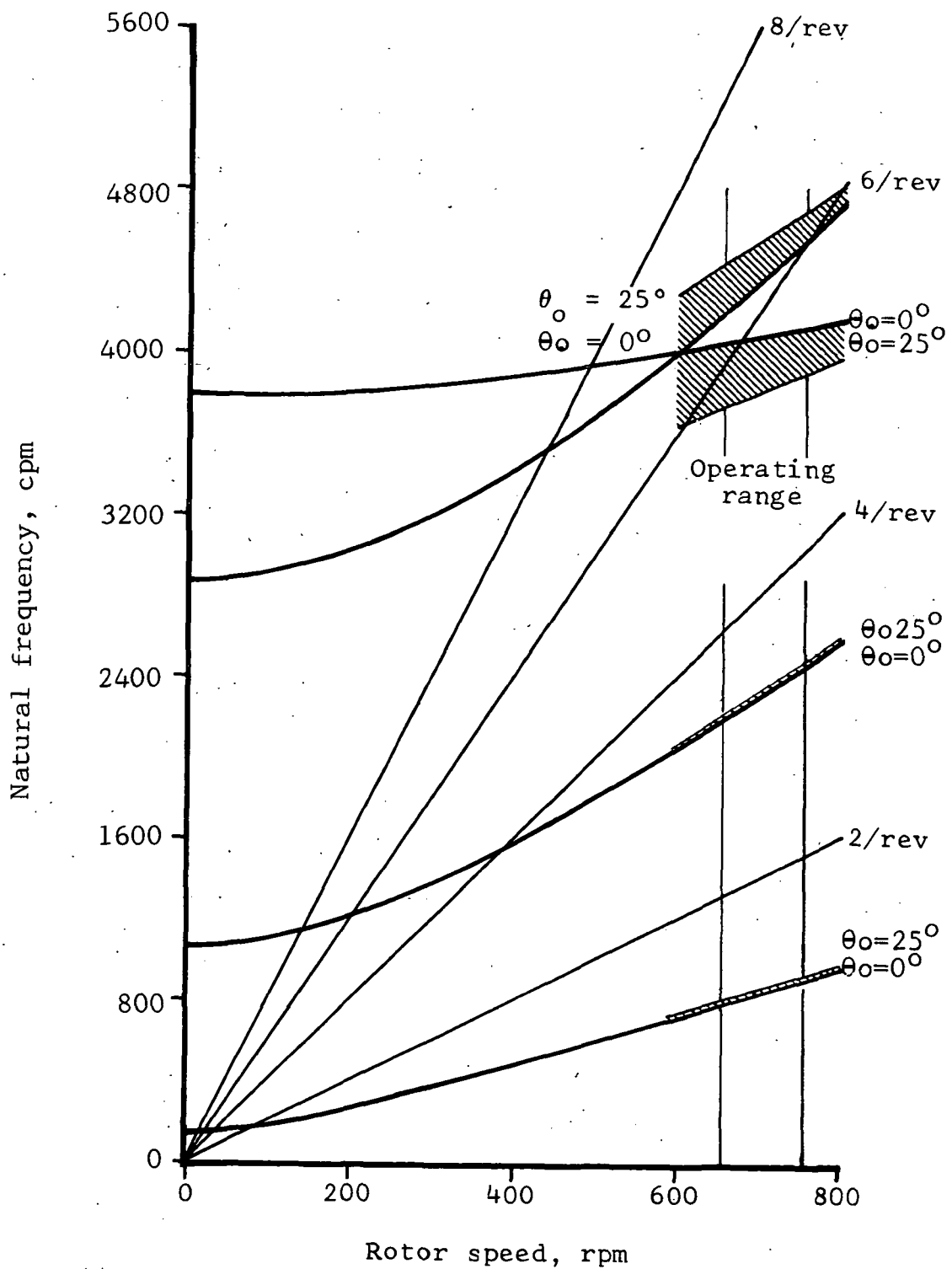


Figure 9. One-fifth Scale UH-1D Model Rotor Natural Frequencies, Collective Mode Fan Plot

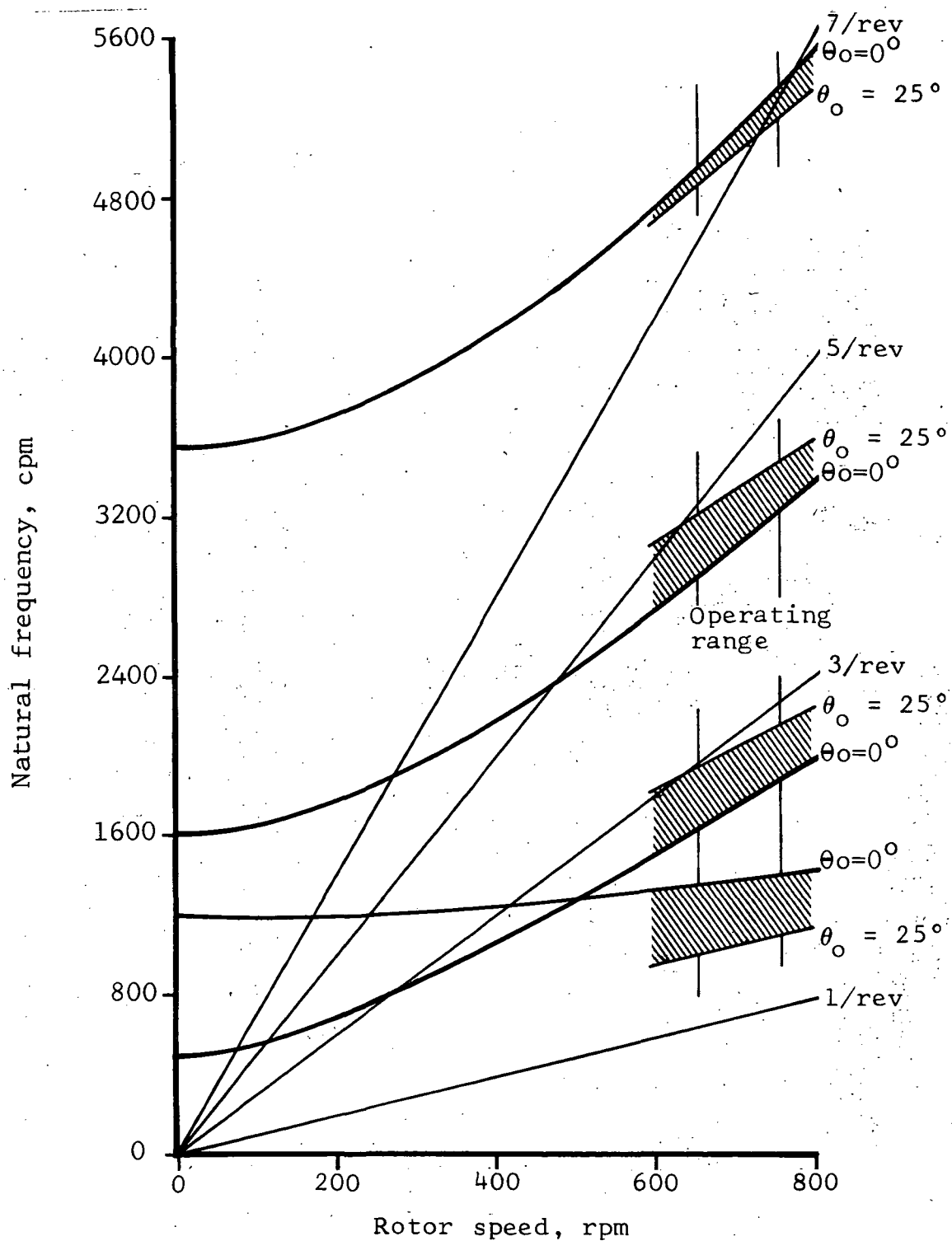


Figure 10. One-fifth Scale UH-1D Model Rotor Natural Frequencies, Cyclic Mode Fan Plot

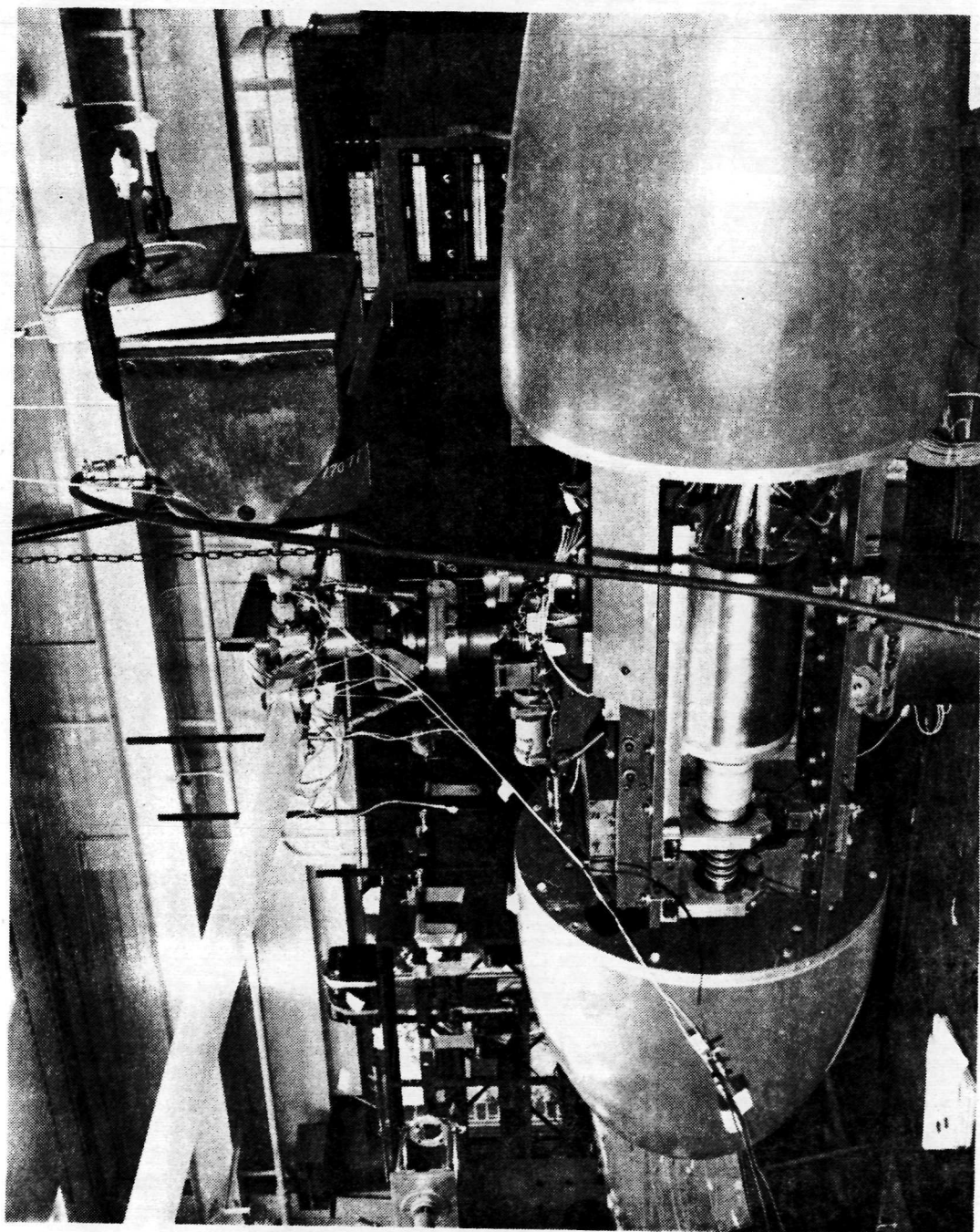


Figure 11. Shake Test Installation.

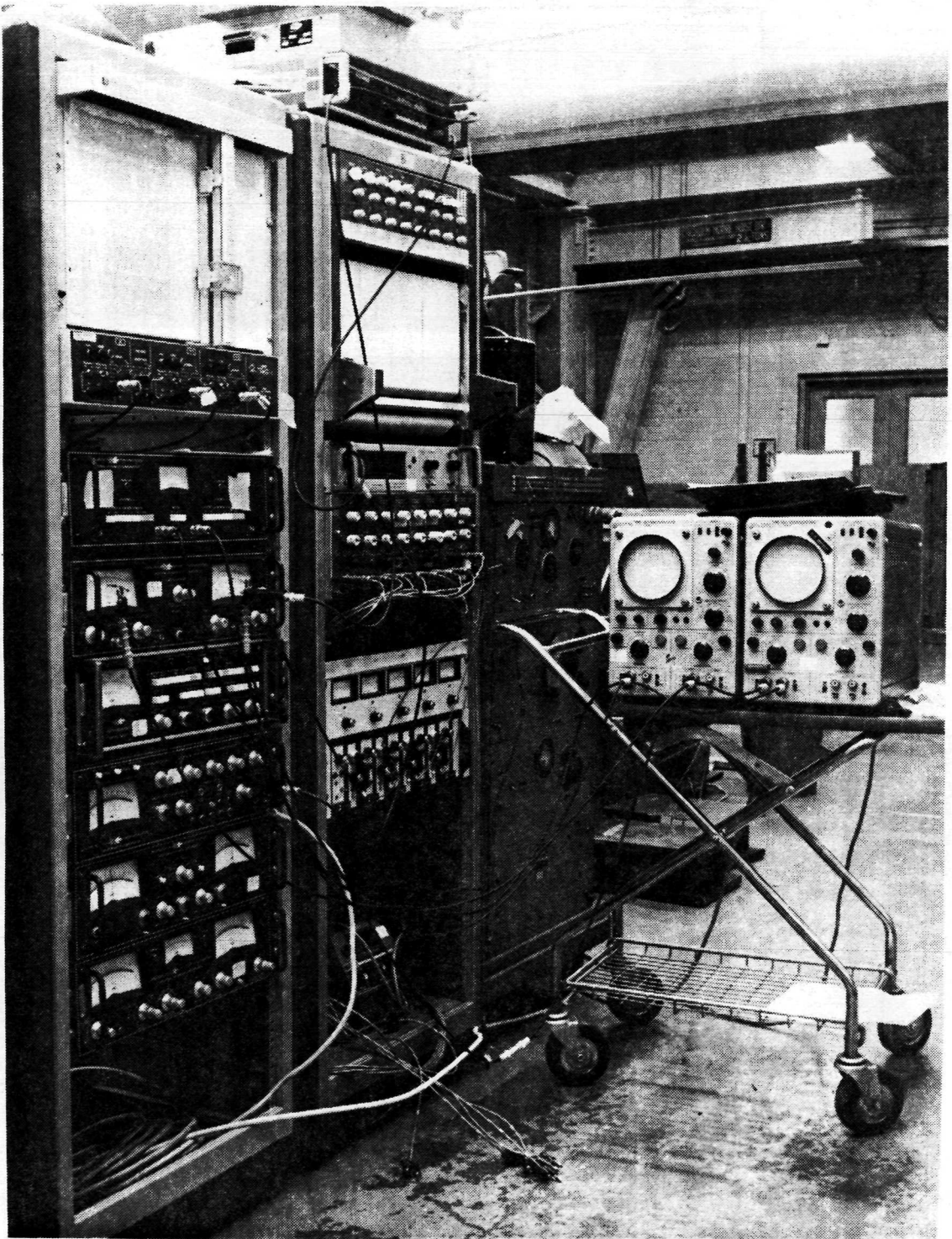


Figure 12. Shake Test Controls and Data Acquisition System.

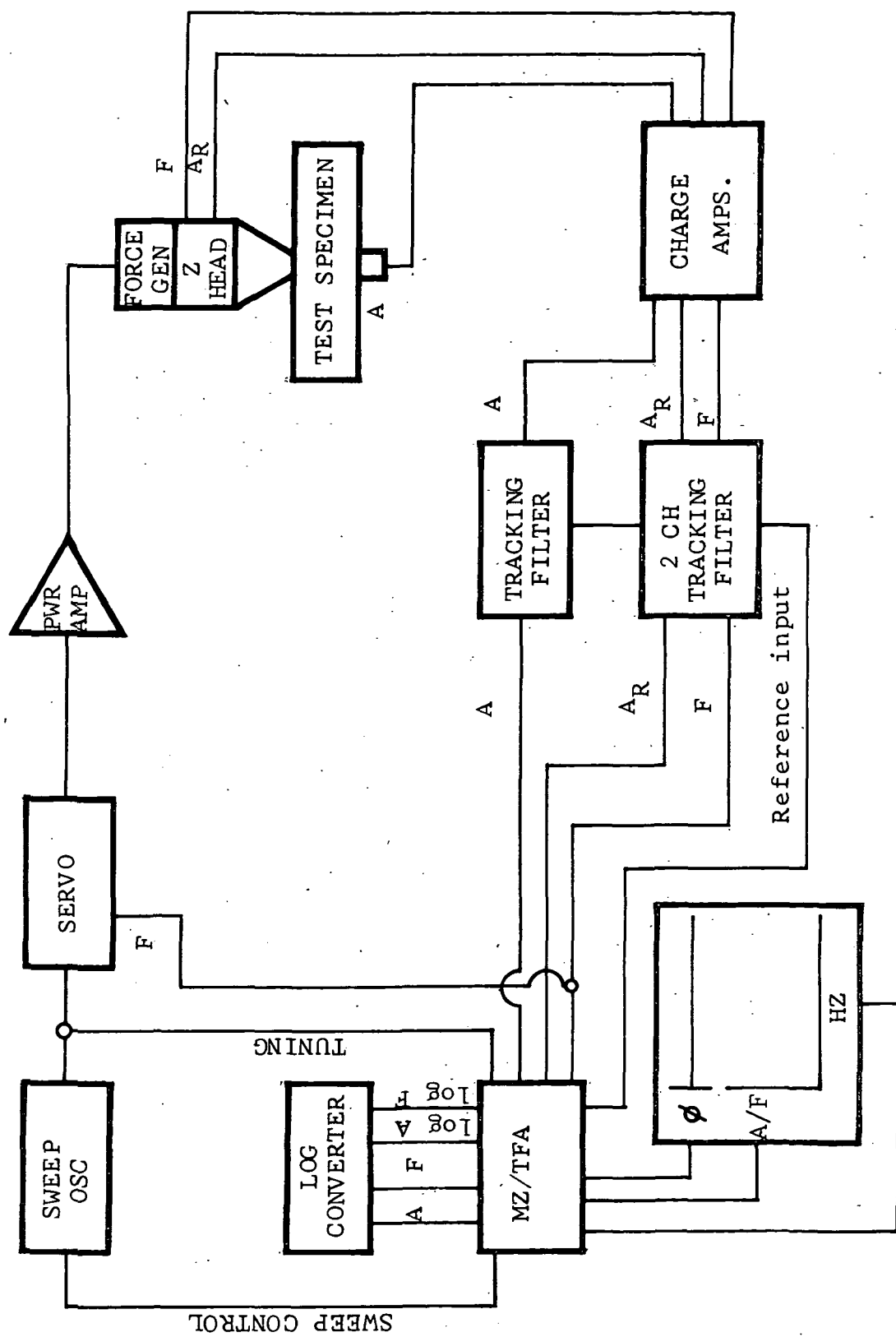


Figure 13. Block Diagram of Ground Vibration Test Data Acquisition System

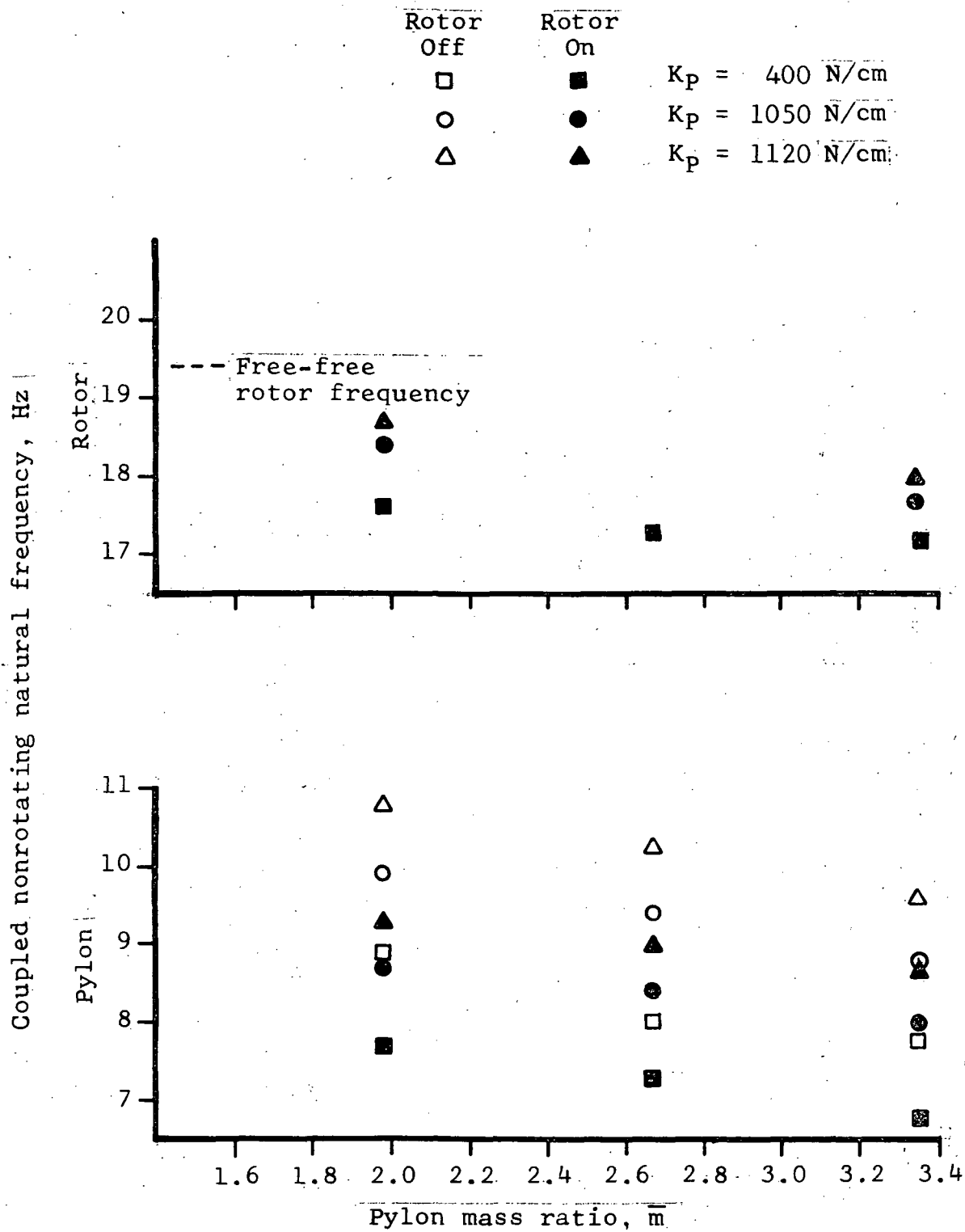


Figure 14. Variation of Longitudinal Pylon and Rotor Natural Frequencies With Pylon Mass Ratio and Spring Rate

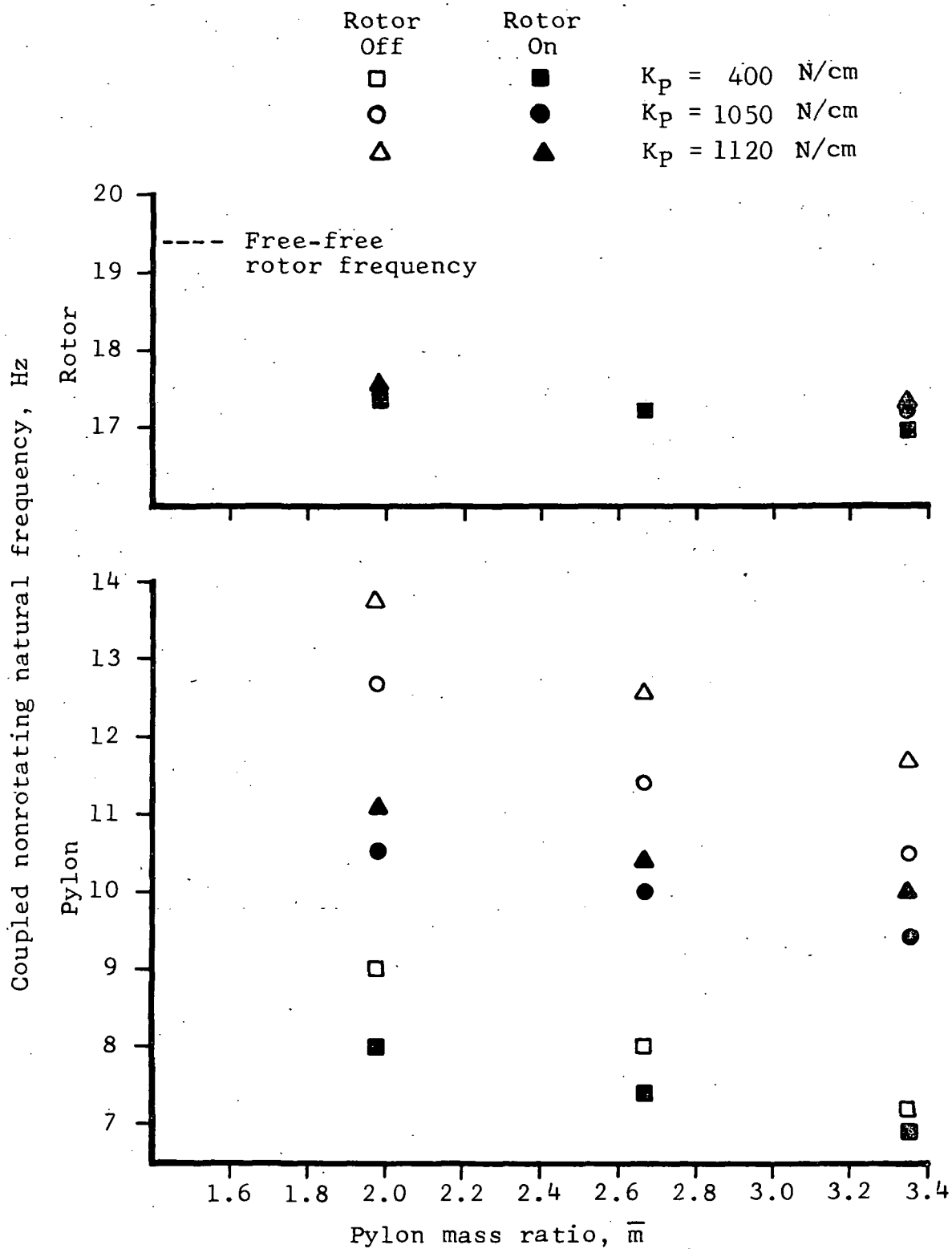


Figure 15. Variation of Lateral Pylon and Rotor Natural Frequencies With Pylon Mass Ratio and Spring Rate

Pylon natural frequency, Hz

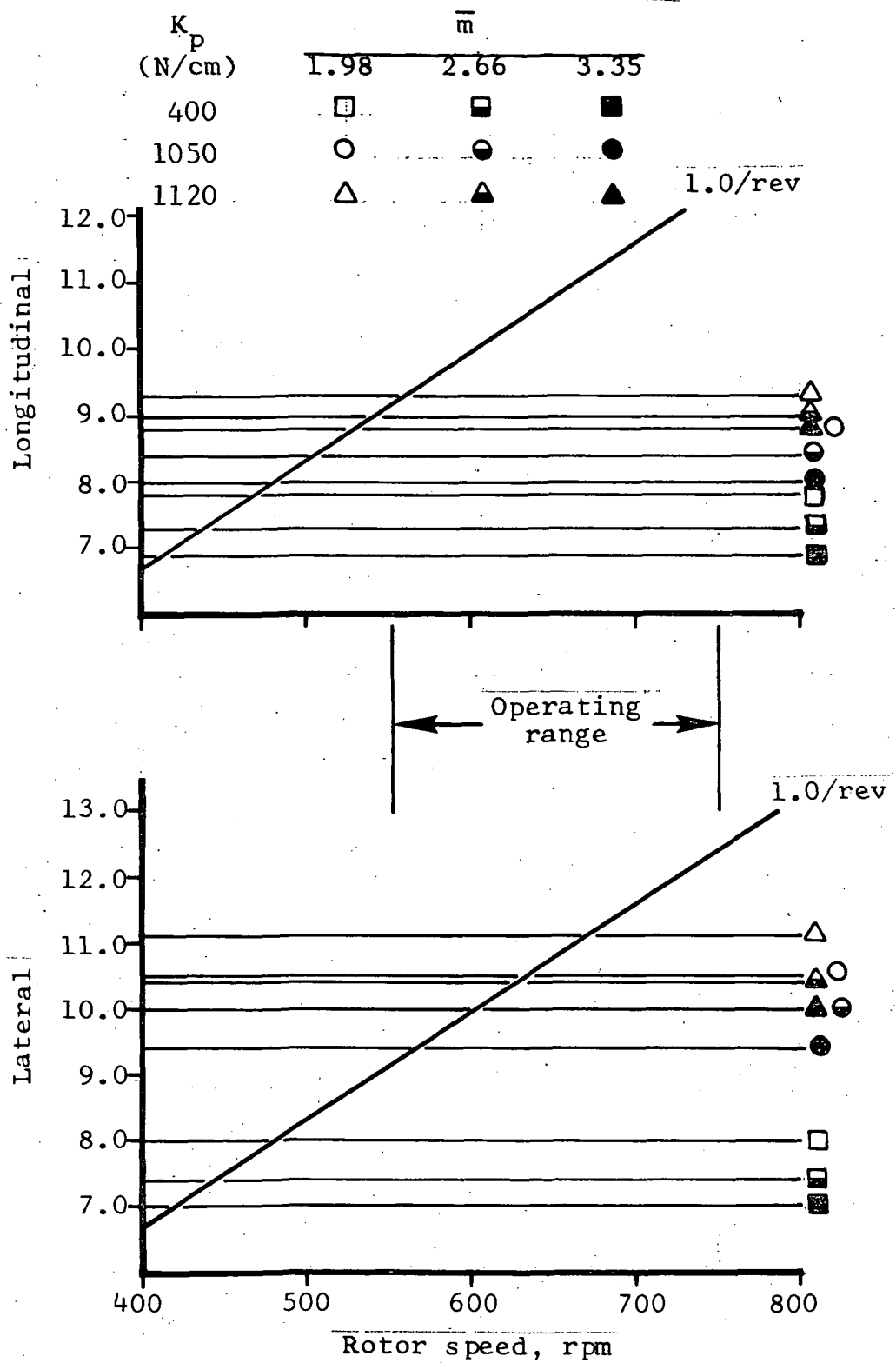


Figure 16. Pylon Fixed System Coincident Frequencies

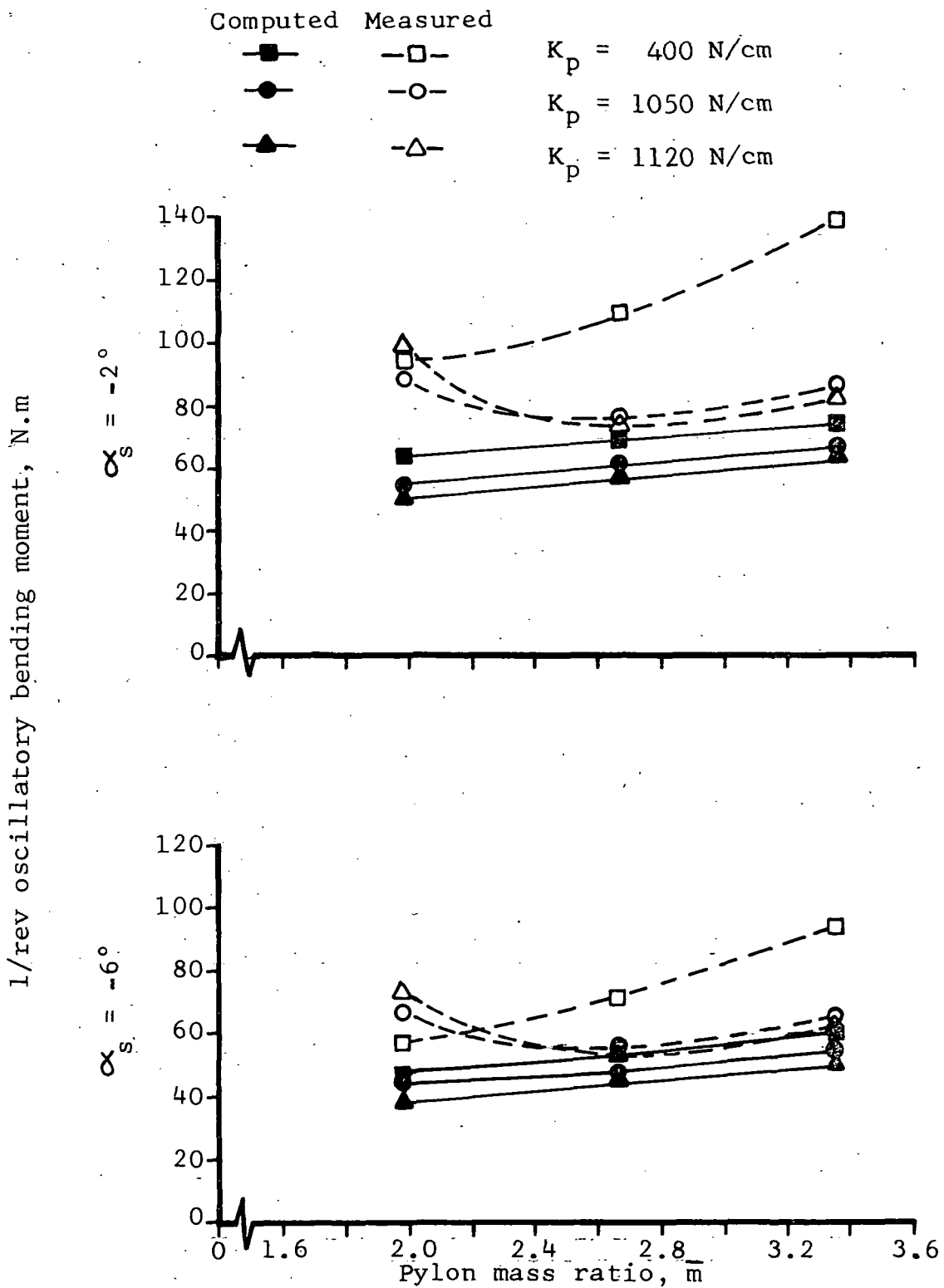


Figure 17. Comparison of Computed and Measured One-per-rev Oscillatory Inplane Bending Moment (15.6-percent Radius) vs Pylon Mass Ratio and Spring Rate for $V = 20.7 \text{ m/s}$, $\text{rpm} = 720$, and $\theta_0 = 16^\circ$

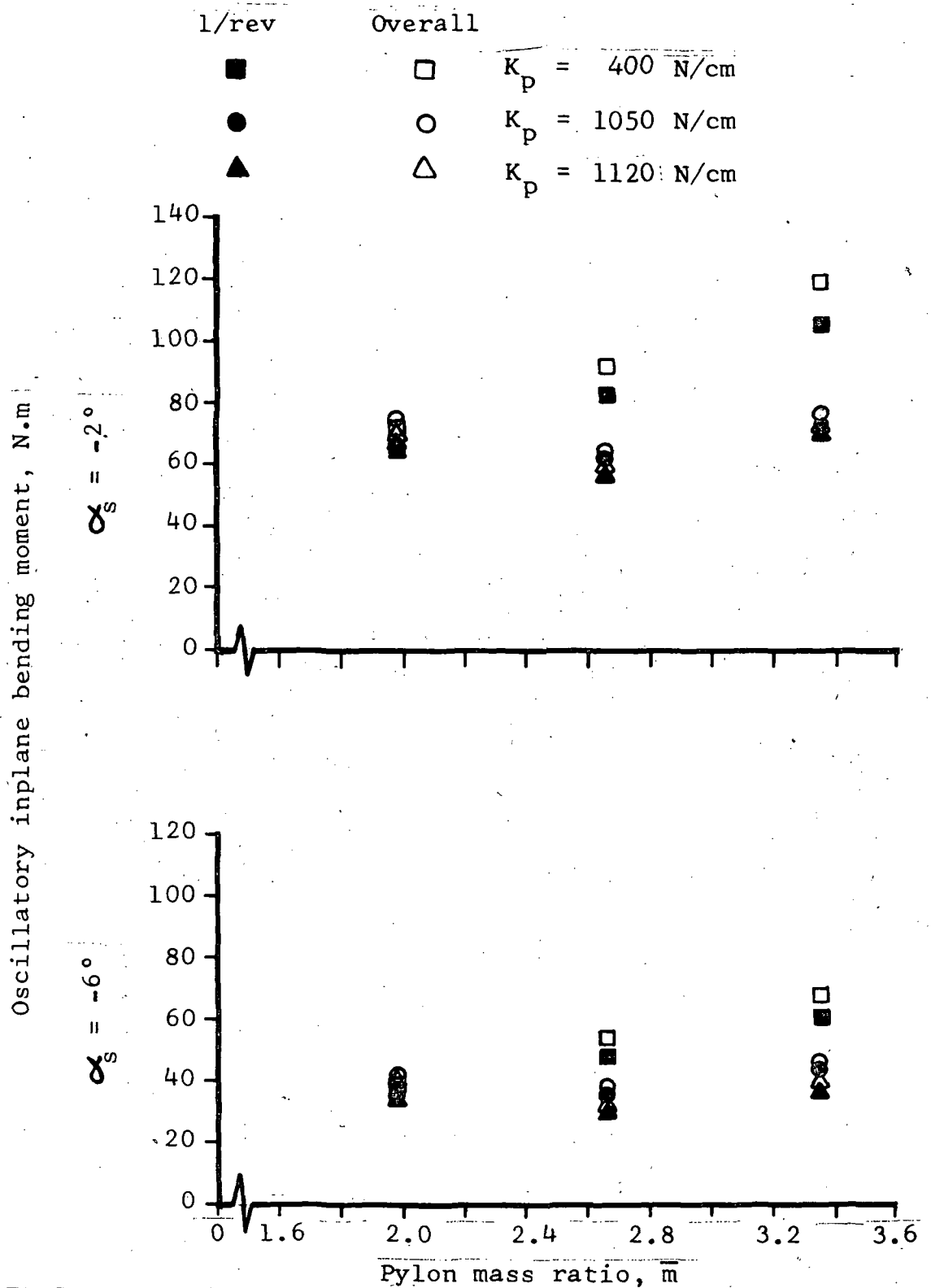


Figure 18. Variation of Inplane Bending Moment (15.6-percent Radius) with Pylon Mass Ratio and Spring Rate for $V = 32.3 \text{ m/s}$, $\text{rpm} = 720$, and $\theta_0 = 16^\circ$

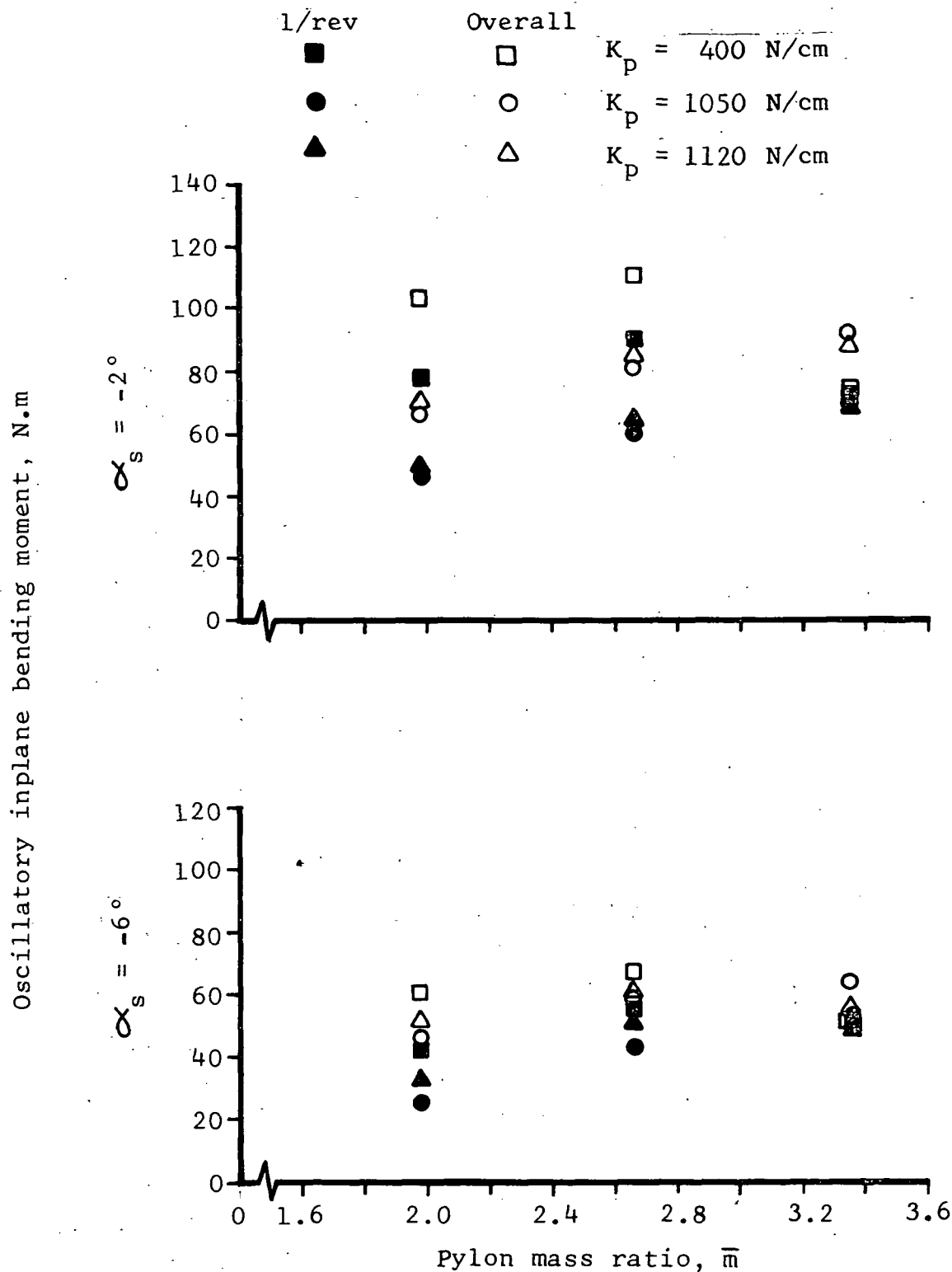


Figure 19. Variation of Inplane Bending Moment (15.6-percent Radius) with Pylon Mass Ratio and Spring Rate for $V = 20.7 \text{ m/s}$, $\text{rpm} = 650$, and $\theta_0 = 16^\circ$

Oscillatory inplane bending moment, N.m

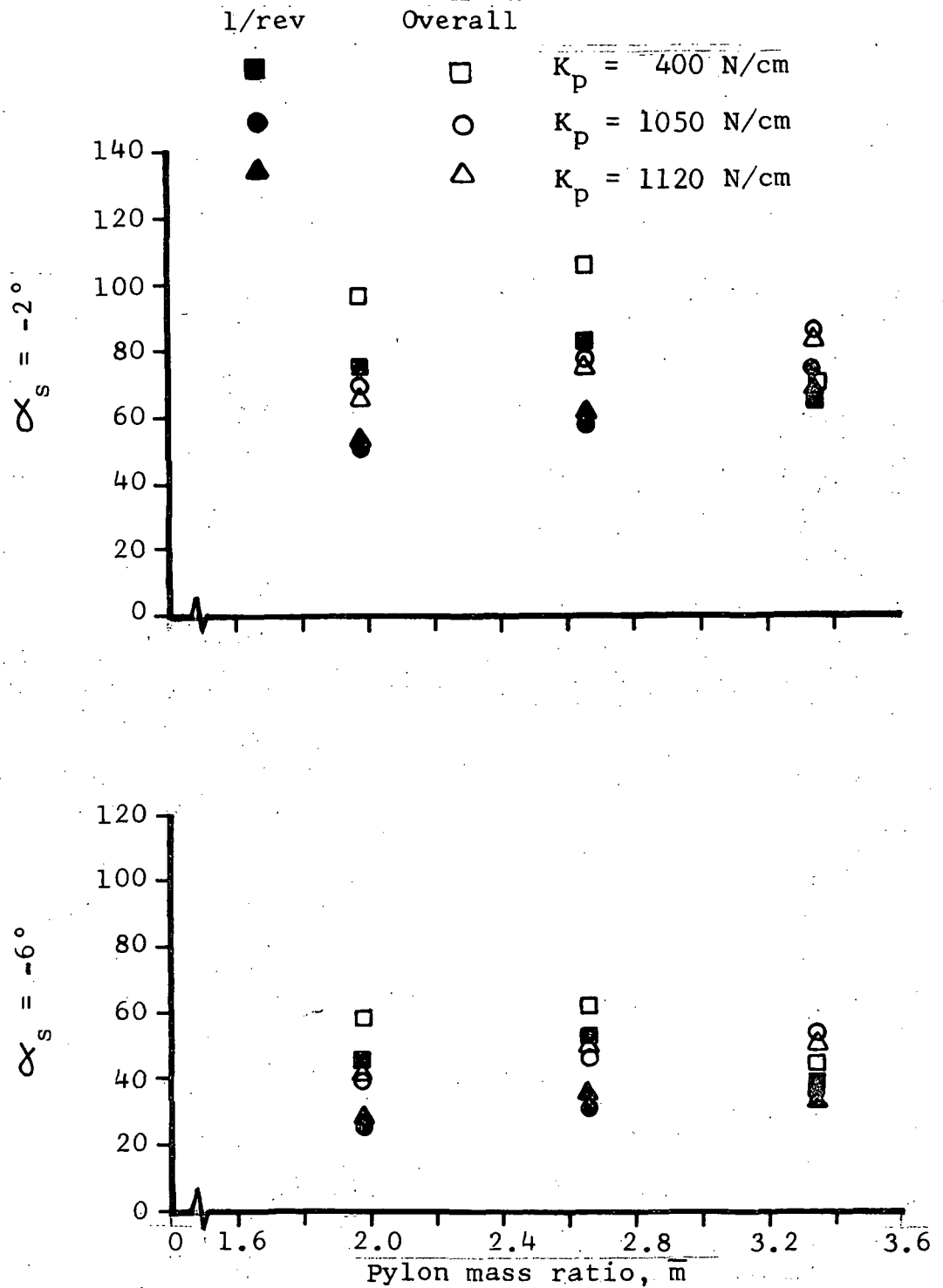


Figure 20. Variation of Inplane Bending Moment (15.6-percent Radius) with Pylon Mass Ratio and Spring Rate for $V = 32.3$ m/s, rpm = 650, and $\theta_0 = 16^\circ$

- Legend
- Overall
 - △ 1/rev
 - 2/rev
 - ◇ 3/rev
 - ▷ 5/rev

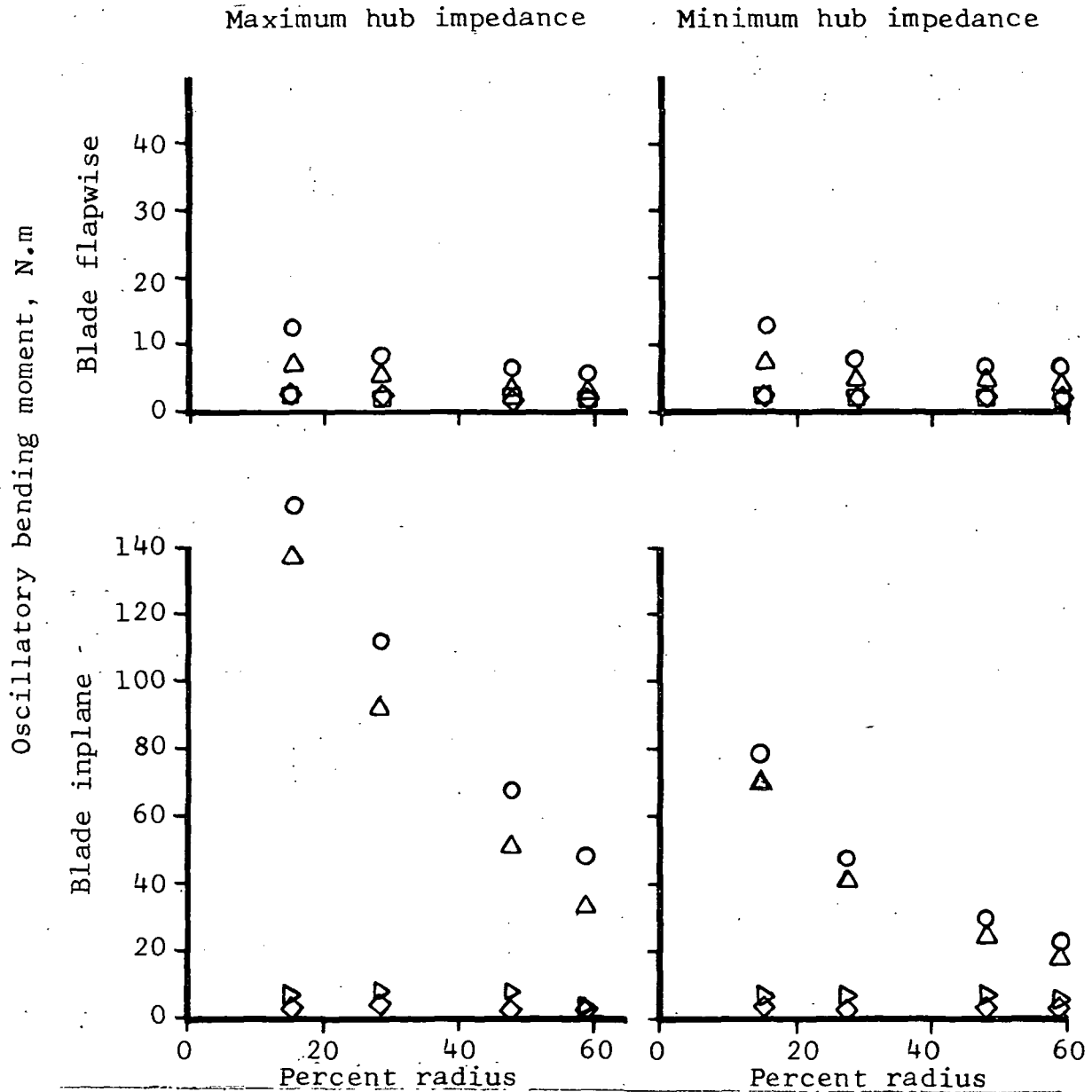


Figure 21. One-fifth Scale UH-1D Main Rotor Oscillatory Bending Moment vs Percent Radius for Maximum and Minimum Hub Impedance at $V = 20.7$ m/s, rpm = 720, and $\theta_0 = 16^\circ$

Page Intentionally Left Blank

APPENDIX

Supplementary Test Data

This appendix contains the test data, or samples of the test data, from which the data tables, data plots, and some conclusions presented in the basic report were derived. Only sample plots of the shake test data are included herein. The large number of shake test parameters not presented are summarized in Tables IV and V of the basic report. Data for only one shaft angle, $\alpha_s = -2^\circ$, are included since the trends at the other shaft angle tested, $\alpha_s = -6^\circ$, were entirely consistent with those contained herein. A brief discussion of each figure or type of figure is contained in the paragraphs that follow.

Figures 22 through 24 show typical response curves (rotor off) for each pylon spring rate at the maximum pylon mass ratio tested ($m=3.35$). Six system modes were observed and are identified in the figures. Figures 25 through 27 show the response curves for the same pylon configuration with the rotor on. Seven additional blade modes were observed and are identified on the figures.

The vertical blade tip response to fore-and-aft excitations at the main rotor hub for the standard pylon spring rate (1050 newton/centimeter) and maximum pylon mass ratio is presented in Figure 28. The inplane blade tip response for excitation of the free-free rotor at the blade tip with a single exciter is given in Figure 29 and with an exciter at each tip (operated in phase) is given in Figure 30. The 5.9 and 6.5 hertz frequencies shown in these figures are related to the suspension system. The other frequencies are rotor natural modes and are identified on the figures.

Composite graphs of overall oscillatory loads as a function of rotor speed, tunnel velocity, and impedance parameters are presented in Figures 31 through 34 for inplane moments at each instrumented blade radial station. Similar data are presented in Figures 35 through 38 for flapwise moments, in Figures 39 and 40 for torsional moments, and in Figure 41 for the pitch link axial loads.

The same trends, as a function of impedance parameters, are demonstrated for inplane loads at all radial stations as discussed in the preceding sections for the 15.6 percent blade radius station. It may be noted that as the magnitude of the inplane moment is reduced (increasing blade radial location), the impedance effects become less apparent.

APPENDIX - Continued

The overall flapwise moments (Figures 35 through 38) show no appreciable variation with inplane impedance parameters. This is the expected result because the vertical hub impedance is essentially invariant for the range of pylon parameters investigated.

The blade torsional moments (Figures 39 and 40) and pitch link axial load (Figure 41) do not exhibit a notable variation with inplane impedance parameters. For the lower velocity case ($V=20.7$ m/s), the torsional moment at the 15.6 percent blade radius station (Figure 39) is significantly higher at 720 rpm than at 650 rpm. This is caused by the proximity of a blade torsional mode near the rotor one-per-rev frequency at 720 rpm. The torsional response varies with rpm but does not vary with impedance changes.

The overall, one-per-rev, and three-per-rev inplane bending moments at the 15.6 percent blade radial station are given as a function of blade root collective pitch and impedance parameters in Figures 42 and 43. Figures 42 and 43 are for Code 3 and Code 2 operating conditions, respectively. The same impedance effects at 14 degrees collective pitch are shown as discussed earlier for 16 degrees collective pitch. The inplane response is too low to observe impedance effects at 12 degrees collective pitch. It is notable that the three-per-rev moment shows no effects due to impedance parameters for either operating condition shown.

The overall, and principal harmonic flapwise bending moments versus collective pitch angle for each pylon configuration is given in Figures 44 and 45 for Code 3 and Code 2 operating conditions, respectively. No variation with impedance parameters are shown for any of the harmonics for either operating condition shown.

APPENDIX-Continued

Rotor-Off

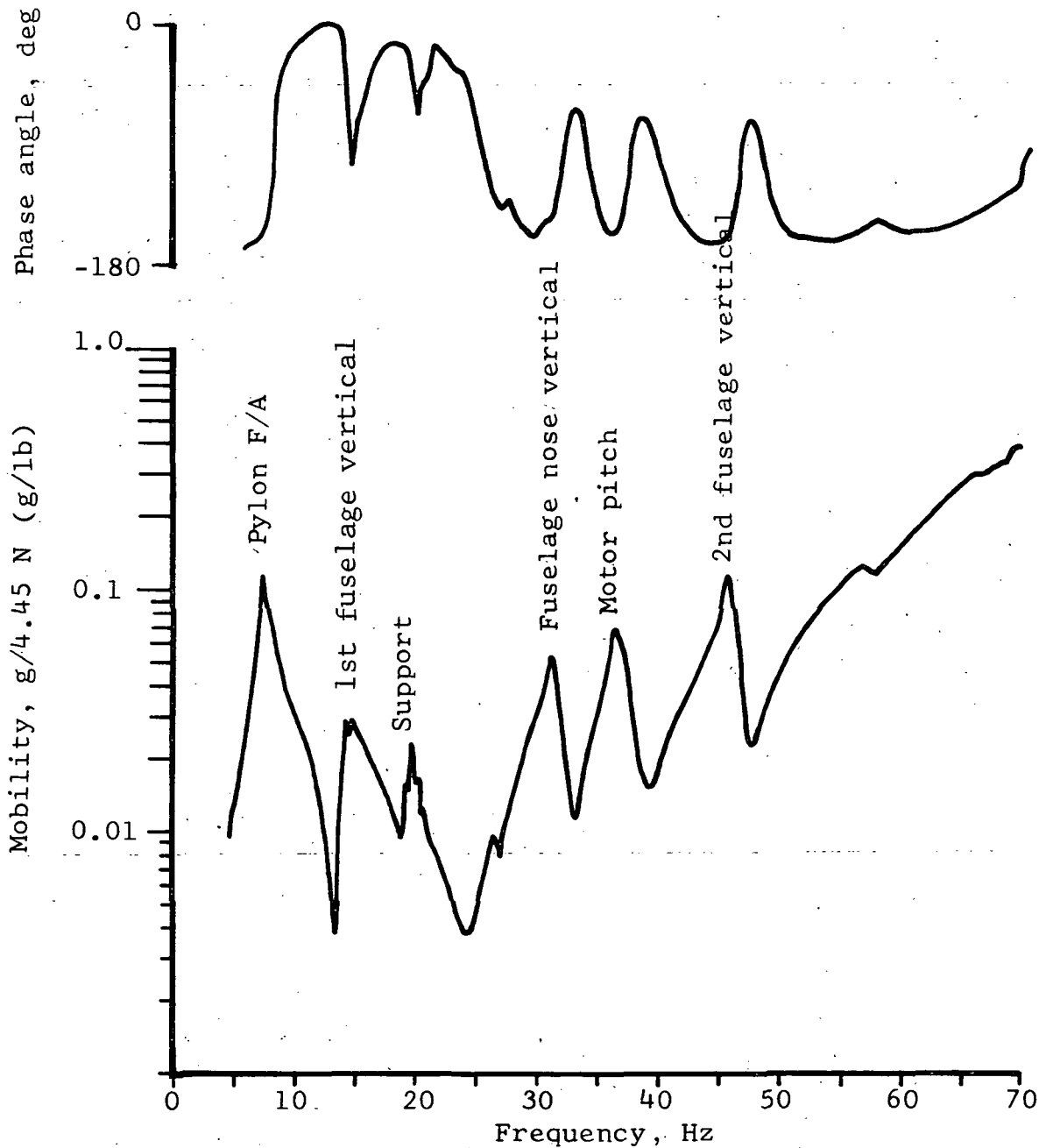


Figure 22. Pylon Longitudinal Hub Mobility vs Frequency for $K_p = 400 \text{ N/cm}$ and $\bar{m} = 3.35$

APPENDIX-Continued

Rotor-Off

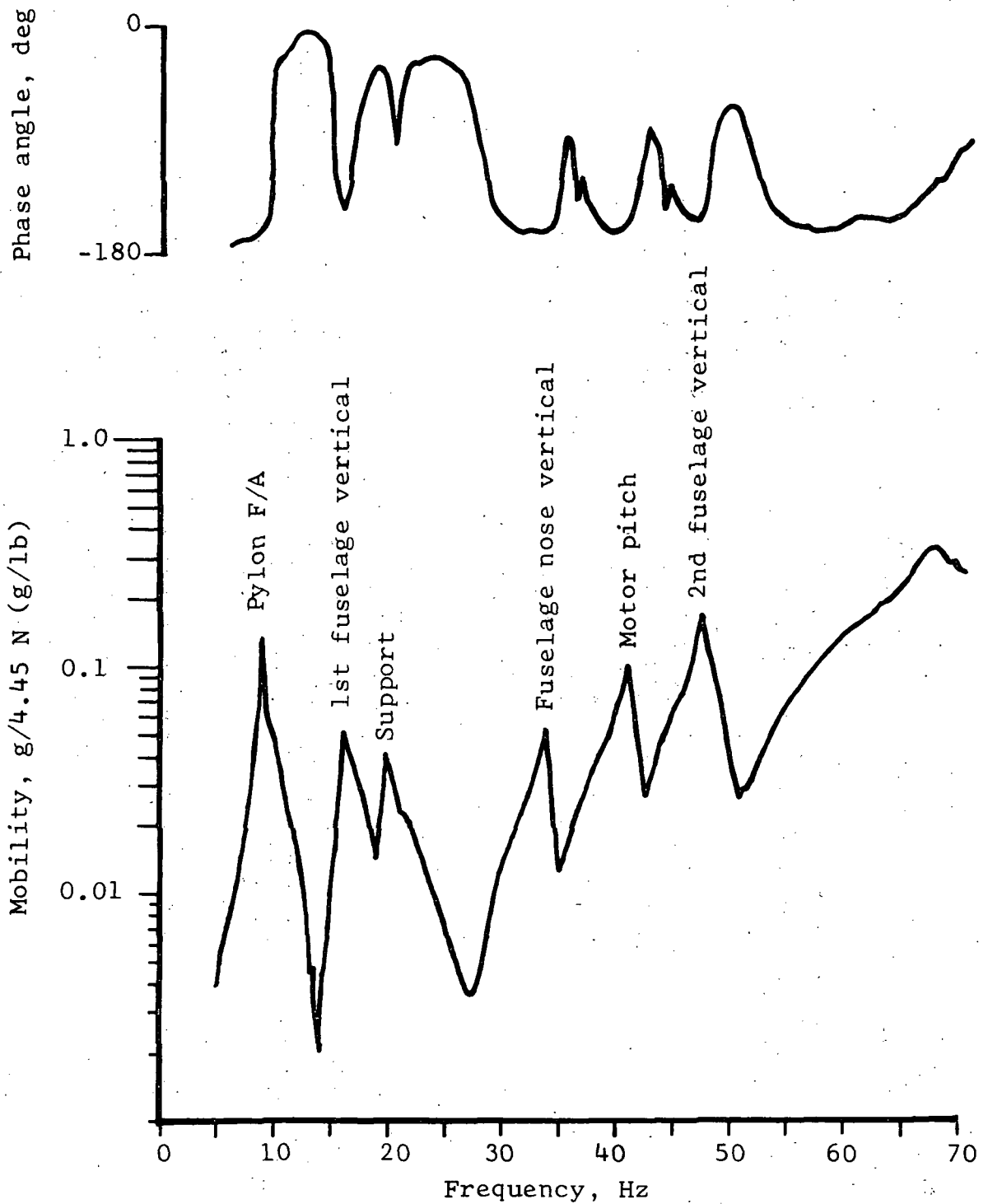


Figure 23. Pylon Longitudinal Hub Mobility vs Frequency for $K_p = 1050 \text{ N/cm}$ and $\bar{m} = 3.35$

APPENDIX-Continued

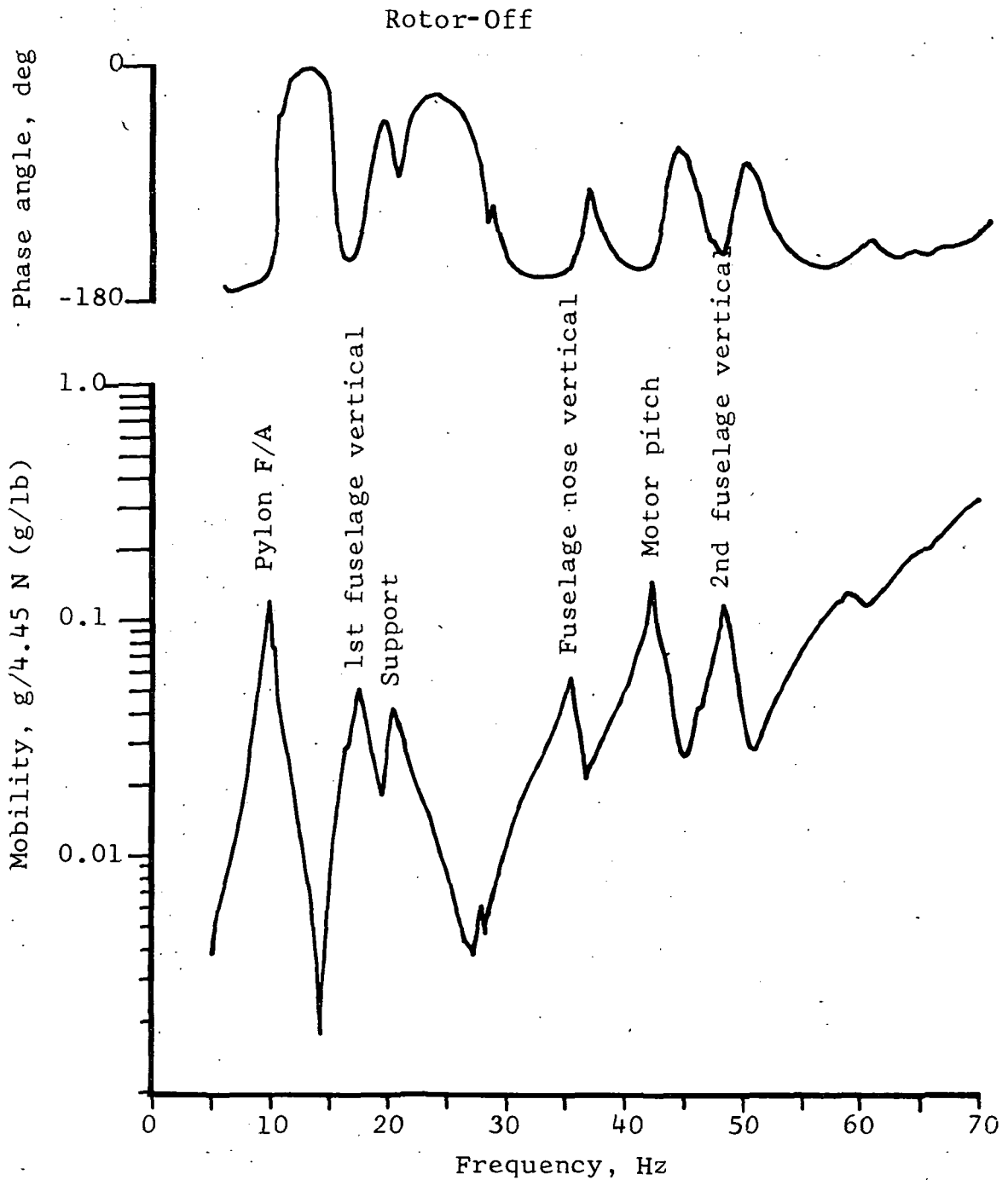


Figure 24. Pylon Longitudinal Hub Mobility vs Frequency
for $K_p = 1120 \text{ N/cm}$ and $\bar{m} = 3.35$

APPENDIX-Continued

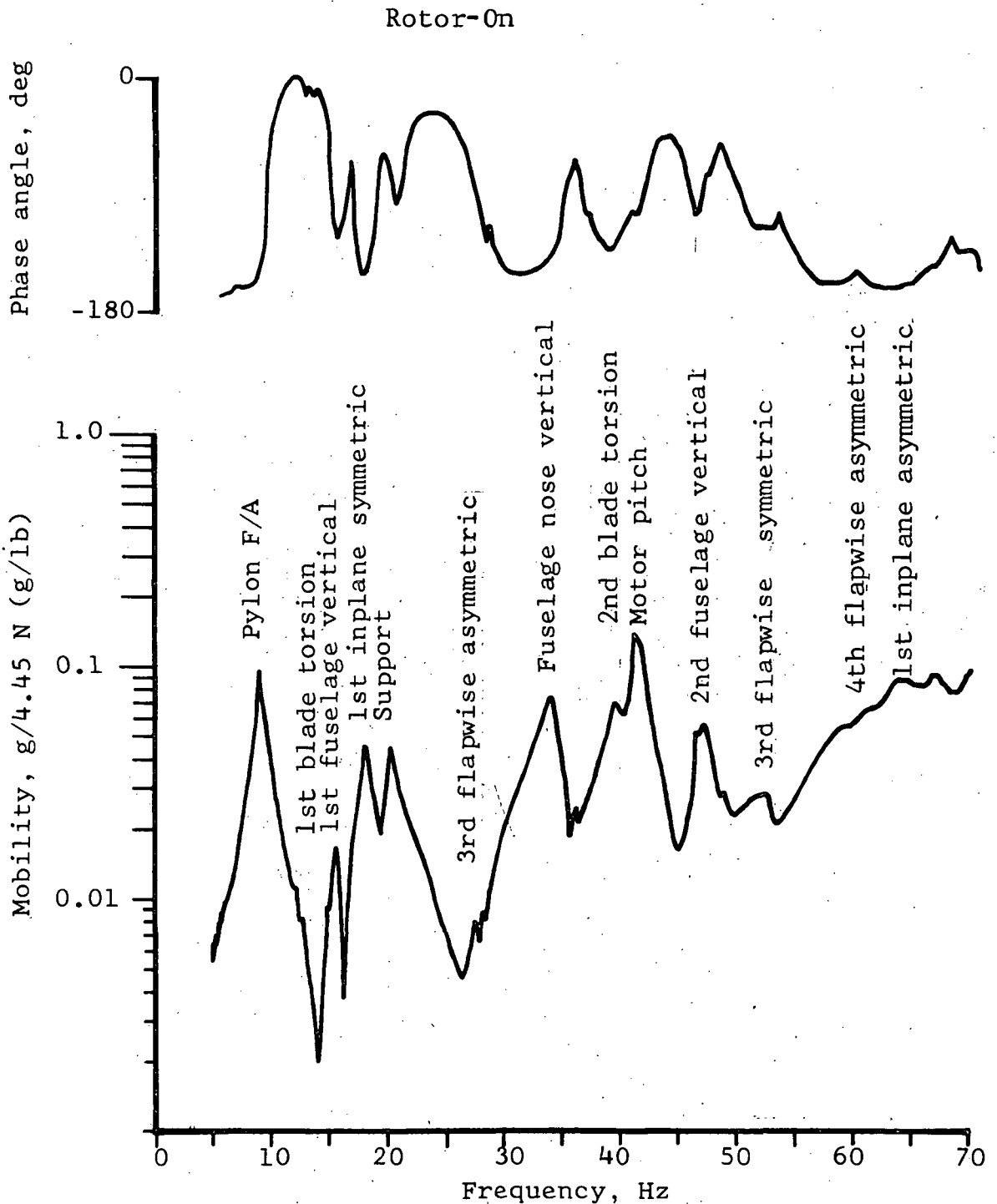


Figure 25. Coupled Pylon/Rotor Longitudinal Hub Mobility vs Frequency for $K_p = 400 \text{ N/cm}$ and $\bar{m} = 3.35$

APPENDIX-Continued

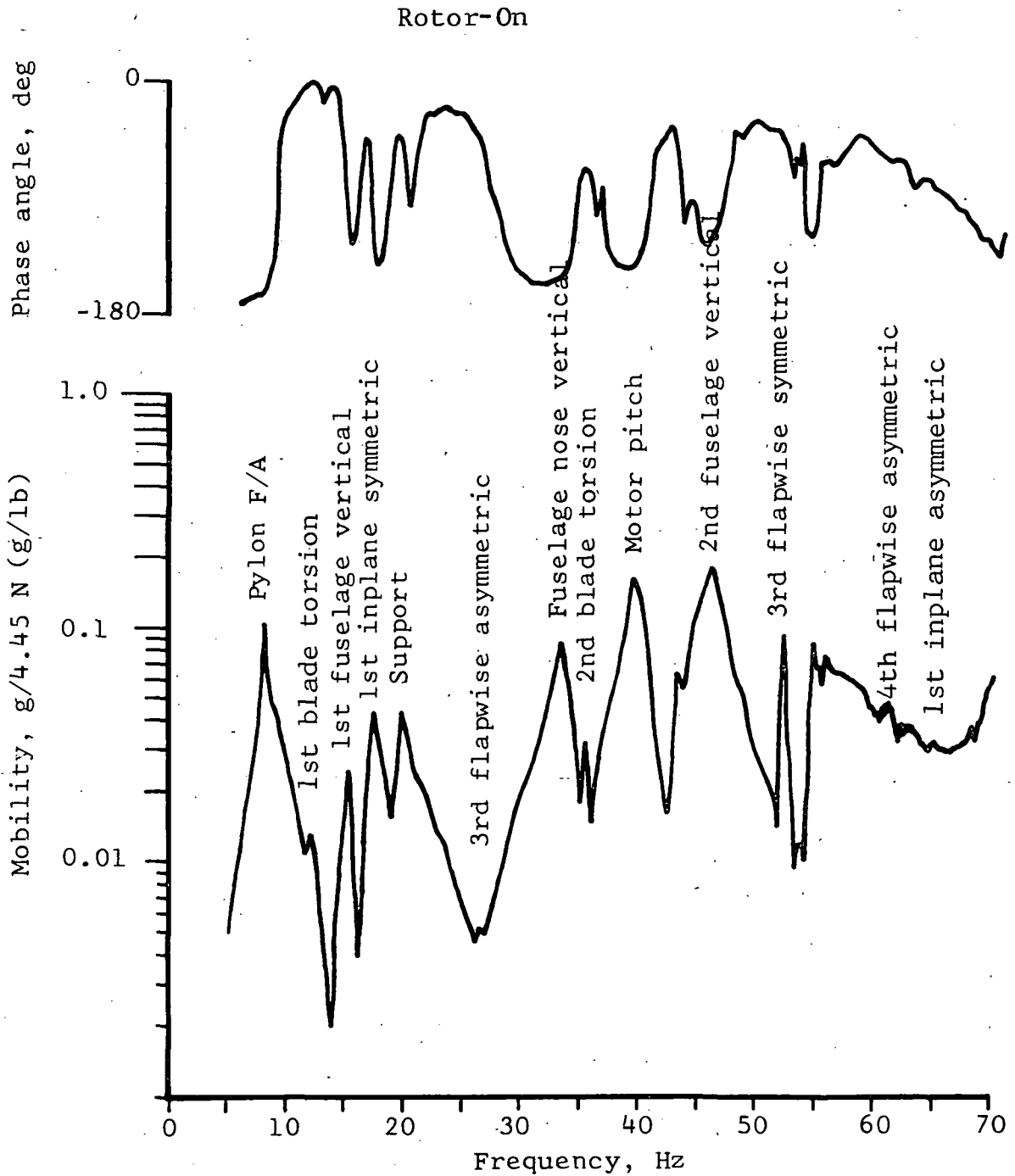


Figure 26. Coupled Pylon/Rotor Longitudinal Hub Mobility vs Frequency for $K_p = 1050 \text{ N/cm}$ and $\bar{m} = 3.35$

APPENDIX-Continued

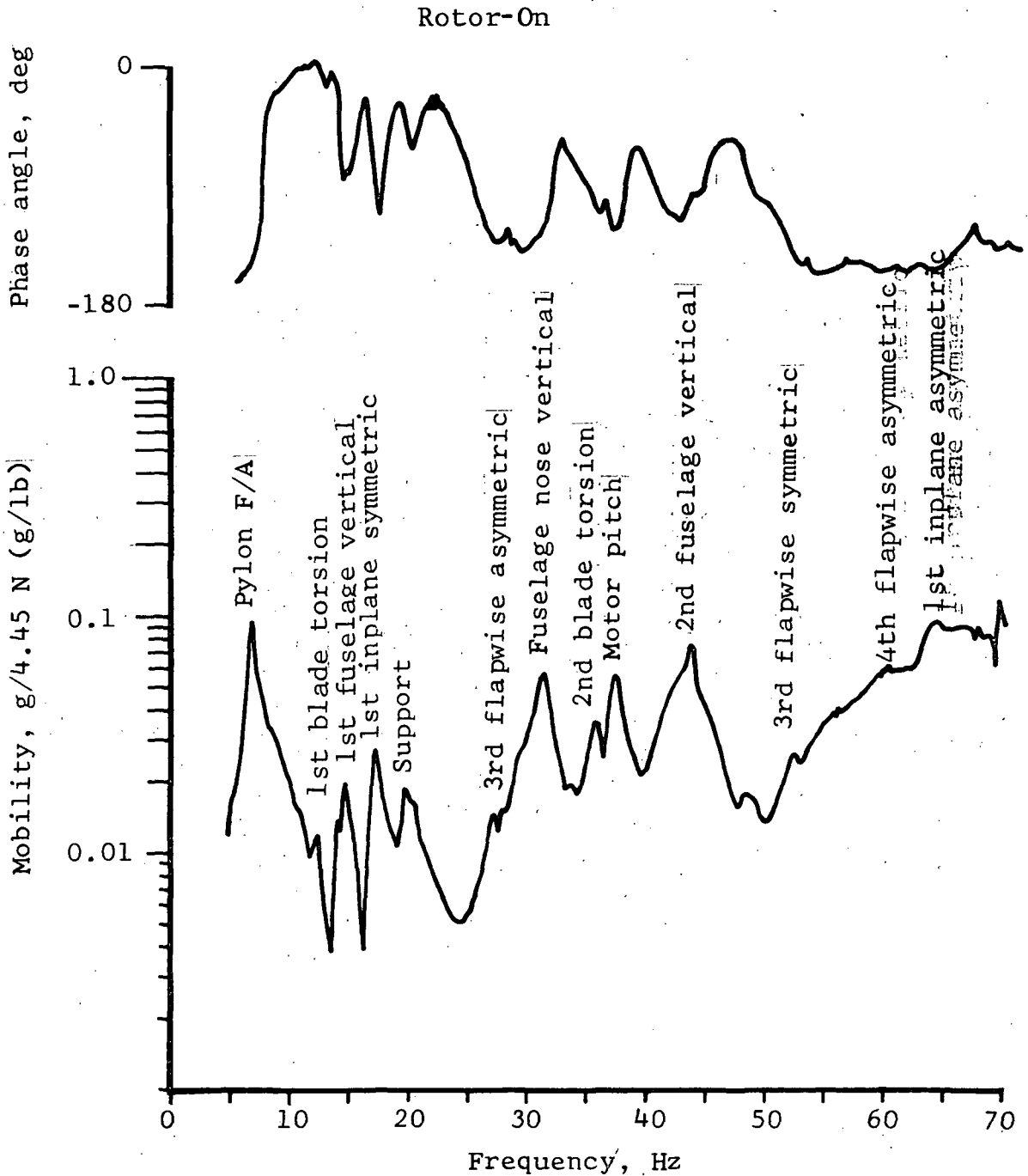


Figure 27. Coupled Pylon/Rotor Longitudinal Hub Mobility vs Frequency for $K_p = 1120 \text{ N/cm}$ and $m = 3.35$

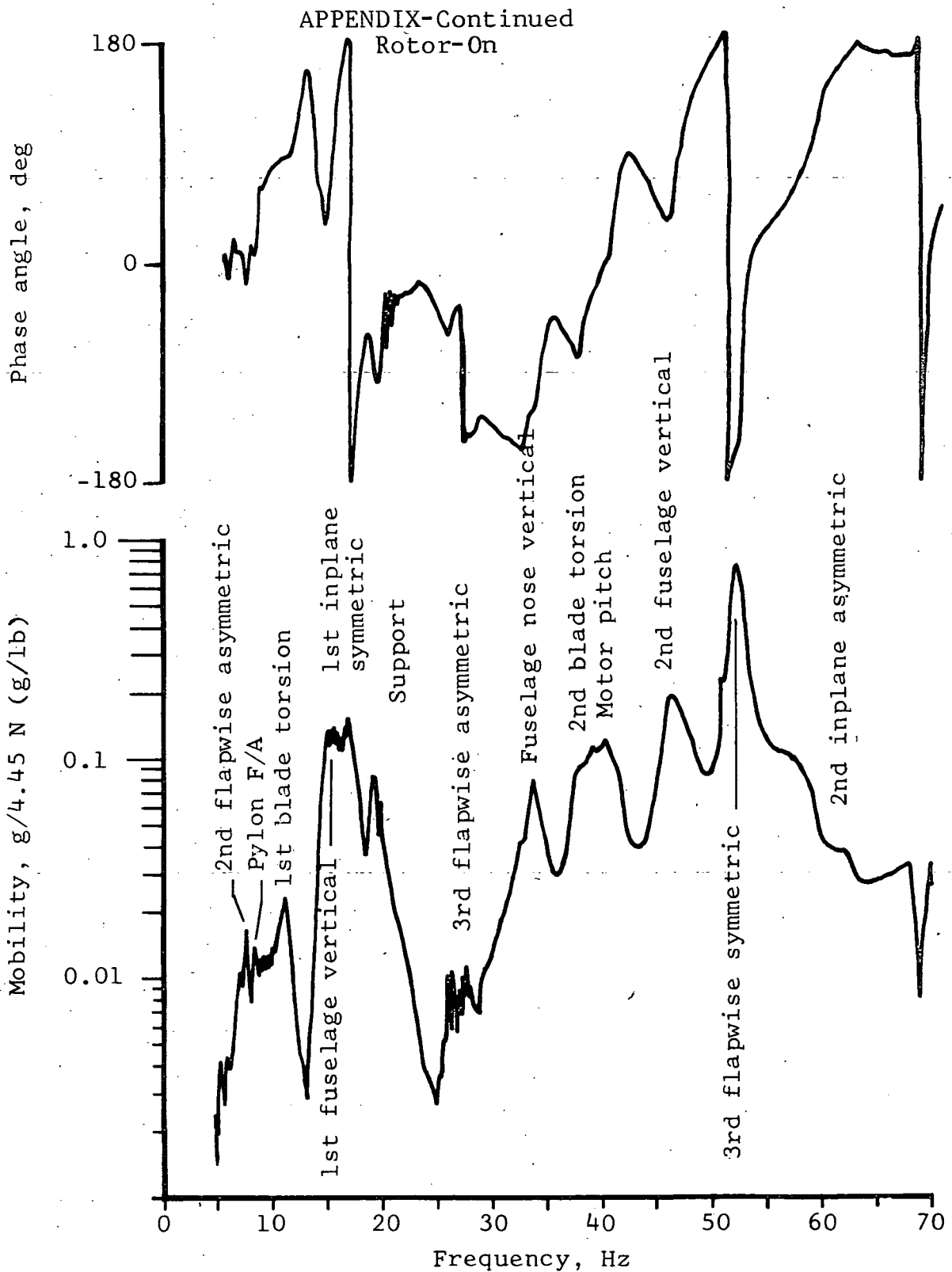


Figure 28. Instrumented Blade Vertical Tip Transfer Mobility vs Frequency for Inplane Excitation at Rotor Hub. (Pylon/Rotor Assembly) $K_p = 1050 \text{ N/cm}$ and $\bar{m} = 3.35$

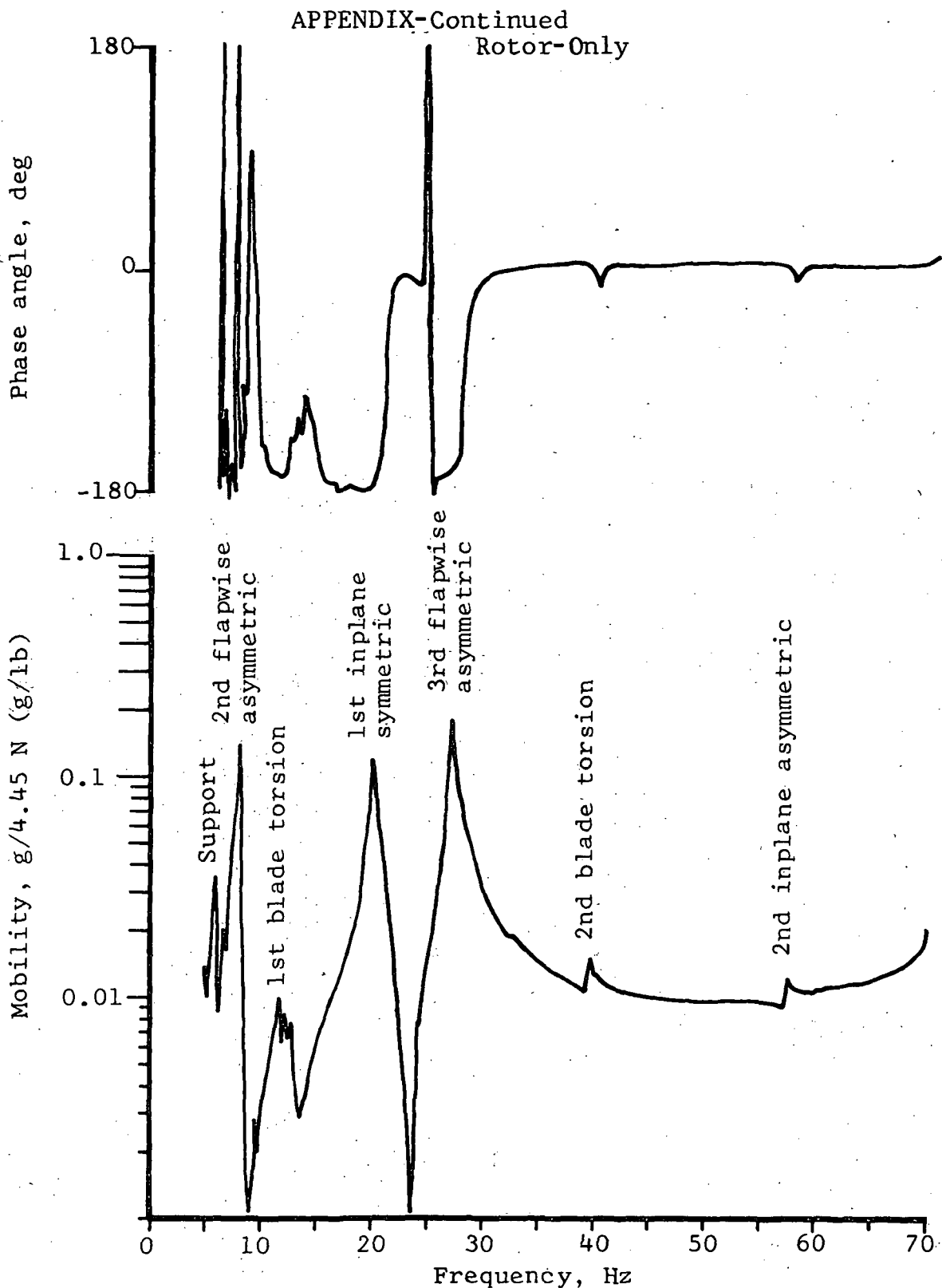


Figure 29. Free-Free Rotor Inplane Hub Mobility vs Frequency for Single Inplane Exciter at Instrumented Blade Tip

APPENDIX-Continued

Rotor-Only

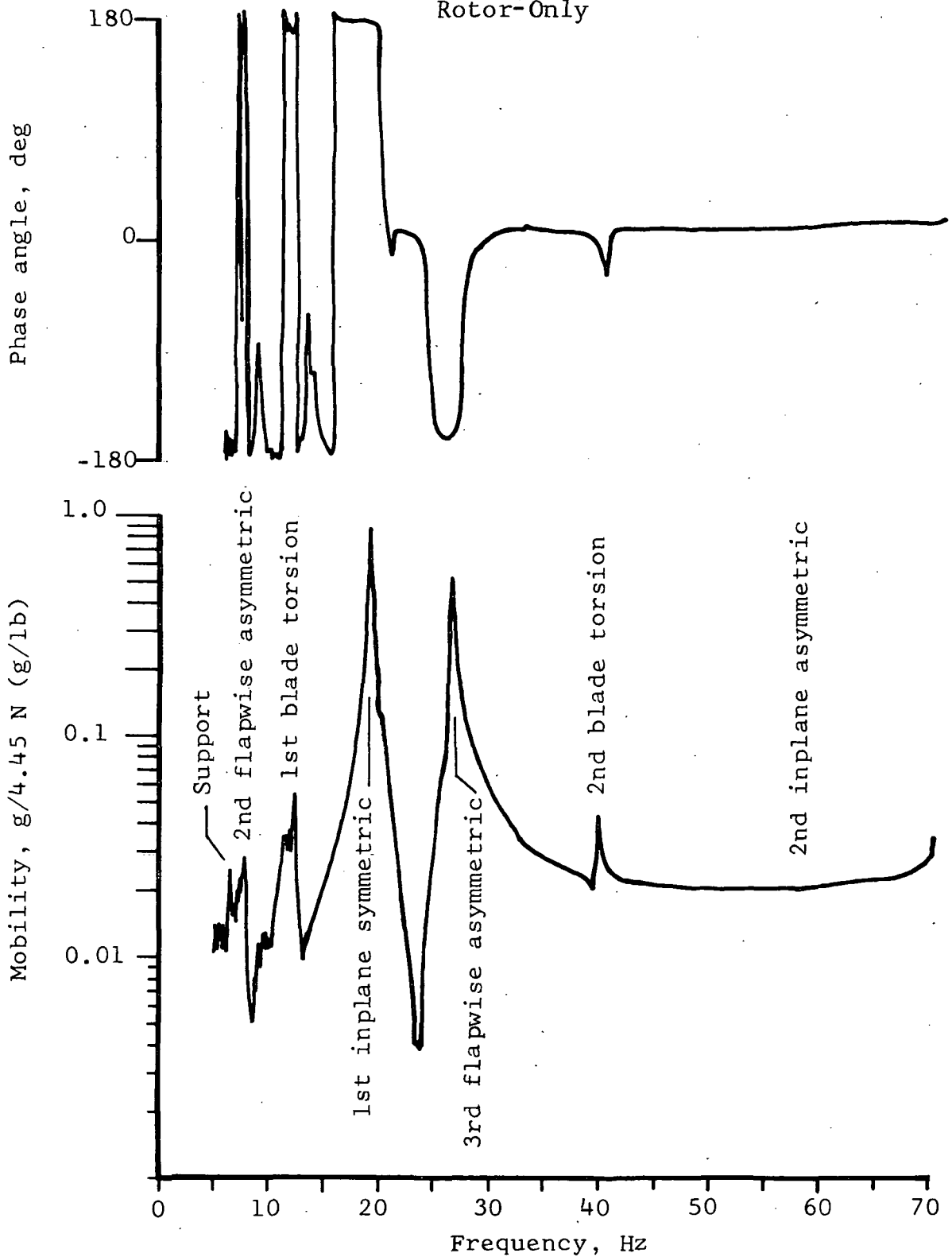


Figure 30. Free-Free Rotor Inplane Hub Mobility vs Frequency for Inplane Excitation at Each Blade Tip

APPENDIX - Continued

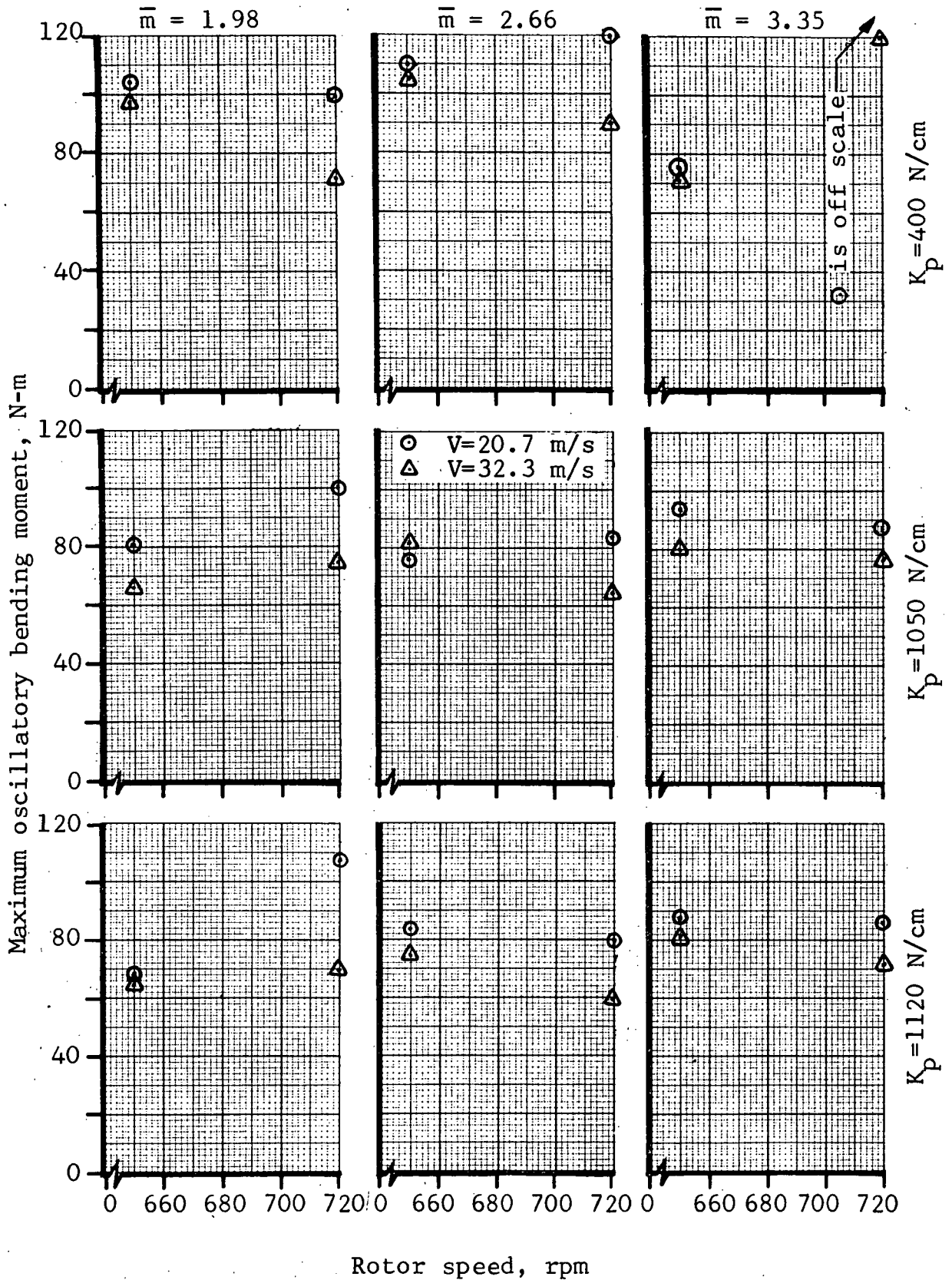


Figure 31. Blade Inplane Bending Moment @ 15.6 Percent Radius,
 $\alpha_s = -2^\circ$, $\theta_o = 16^\circ$

APPENDIX - Continued

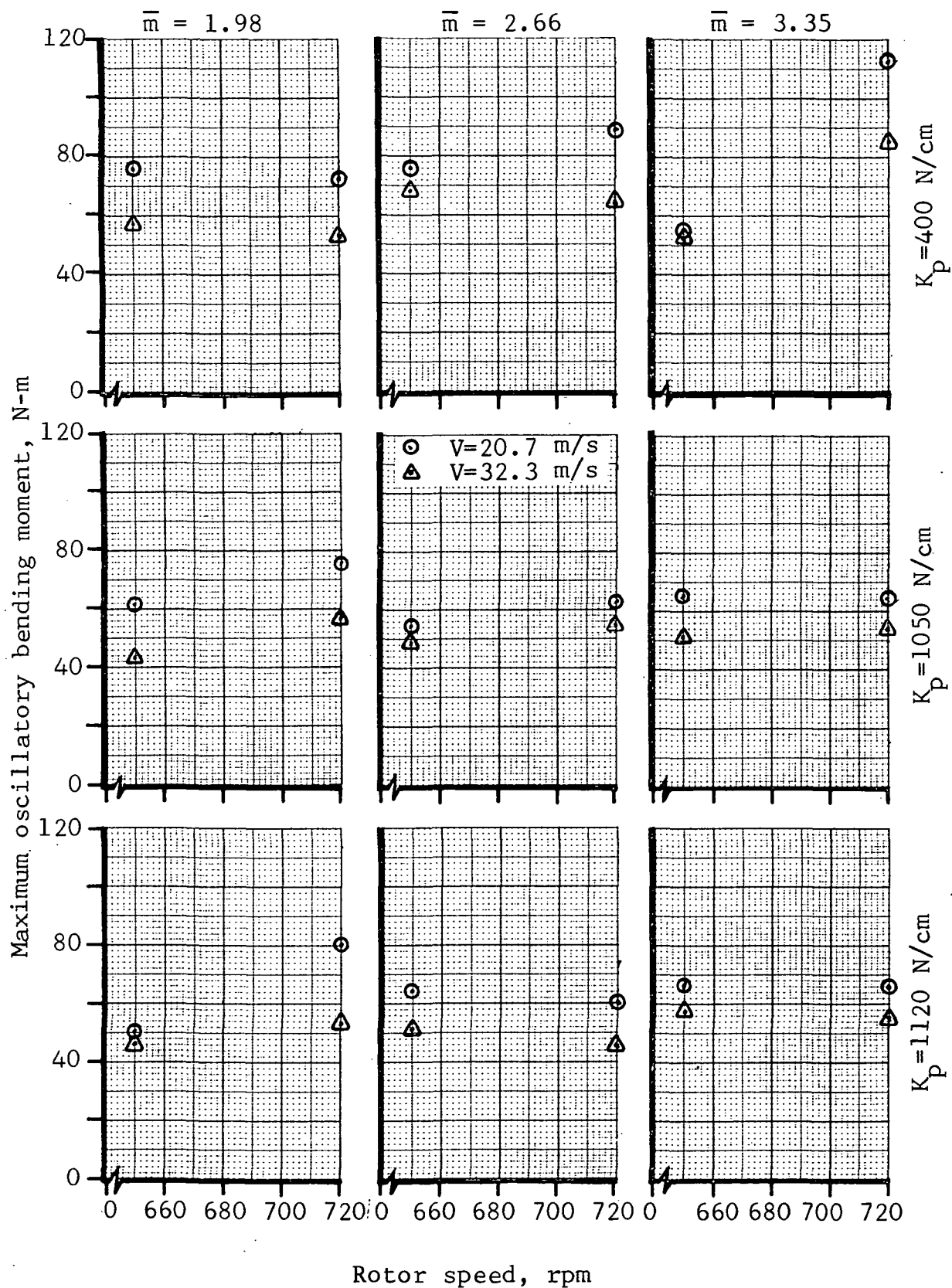


Figure 32. Blade Inplane Bending Moment @ 28.8 Percent Radius, $\alpha_s = -2^\circ$, $\theta_o = 16^\circ$

APPENDIX - Continued

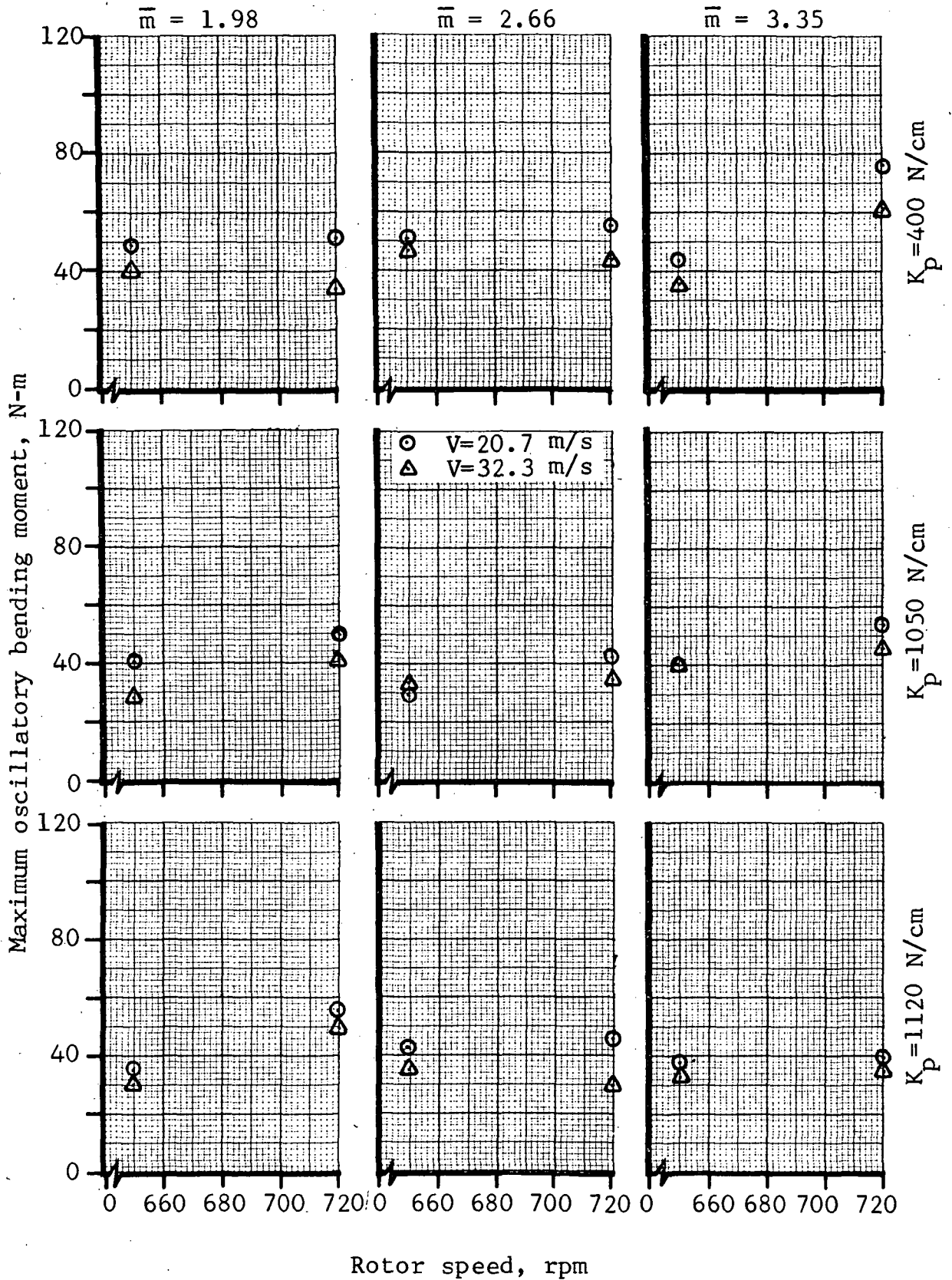


Figure 33. Blade Inplane Bending Moment @ 47.9 Percent Radius, $\alpha_s = -2^\circ$, $\theta_o = 16^\circ$

APPENDIX - Continued

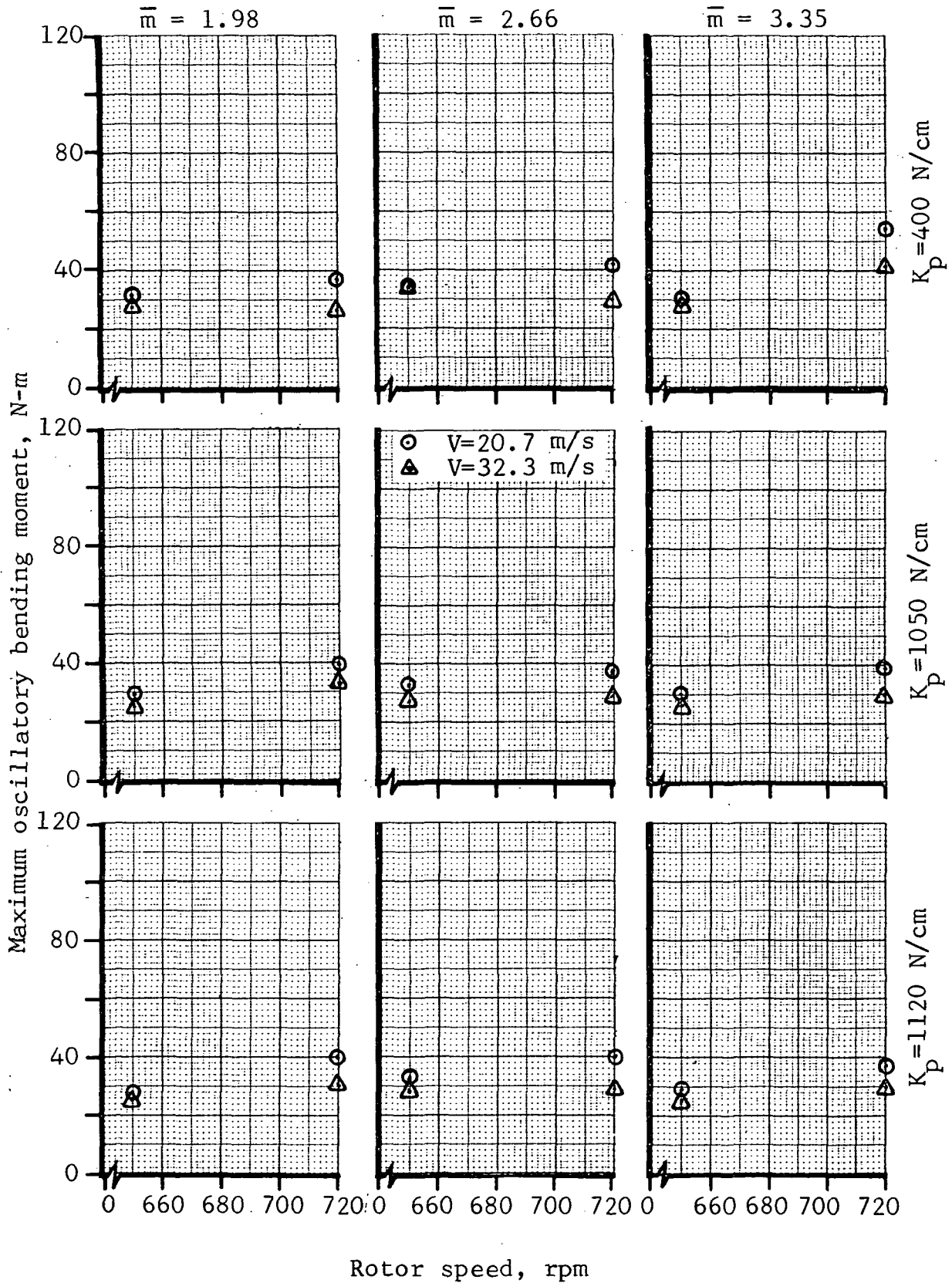


Figure 34. Blade Inplane Bending Moment @ 59.0 Percent Radius,
 $\alpha_s = -2^\circ$, $\theta_o = 16^\circ$

APPENDIX - Continued

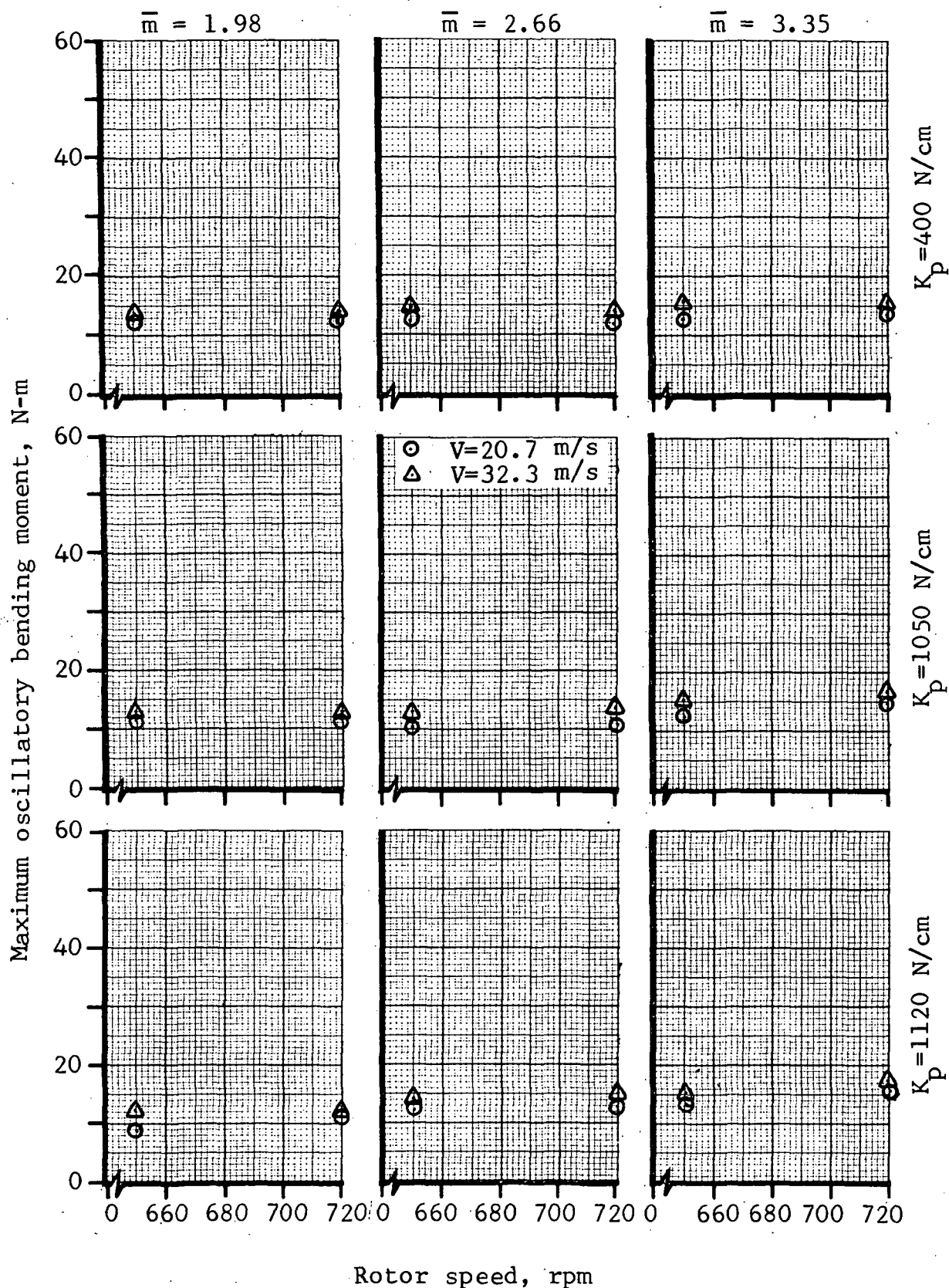


Figure 35. Blade Flapwise Bending Moment @ 15.6 Percent Radius, $\alpha_s = -2^\circ$, $\theta_o = 16^\circ$

APPENDIX - Continued

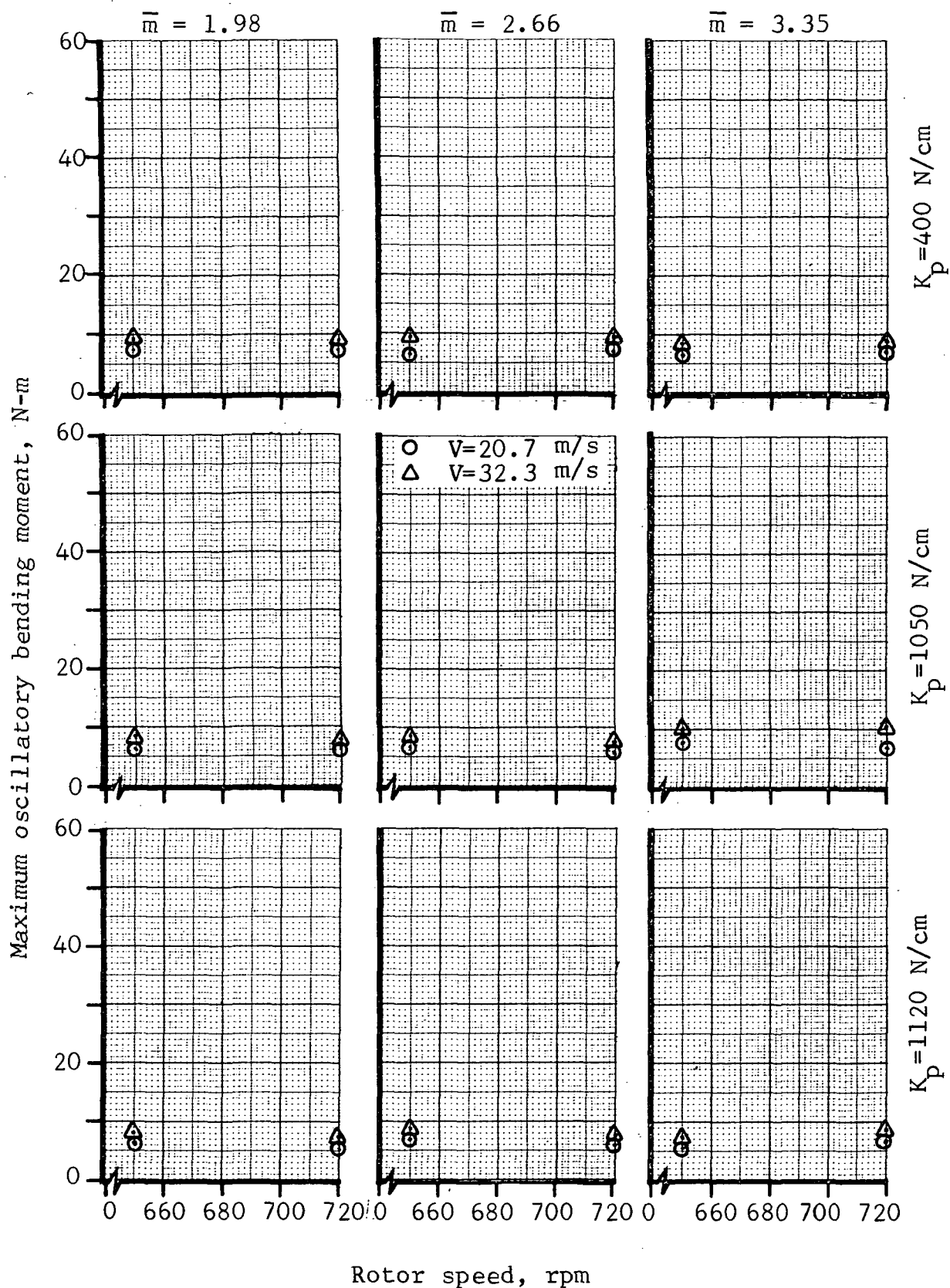


Figure 36. Blade Flapwise Bending Moment @ 28.8 Percent Radius,
 $\alpha_s = -2^\circ$, $\theta_o = 16^\circ$

APPENDIX - Continued

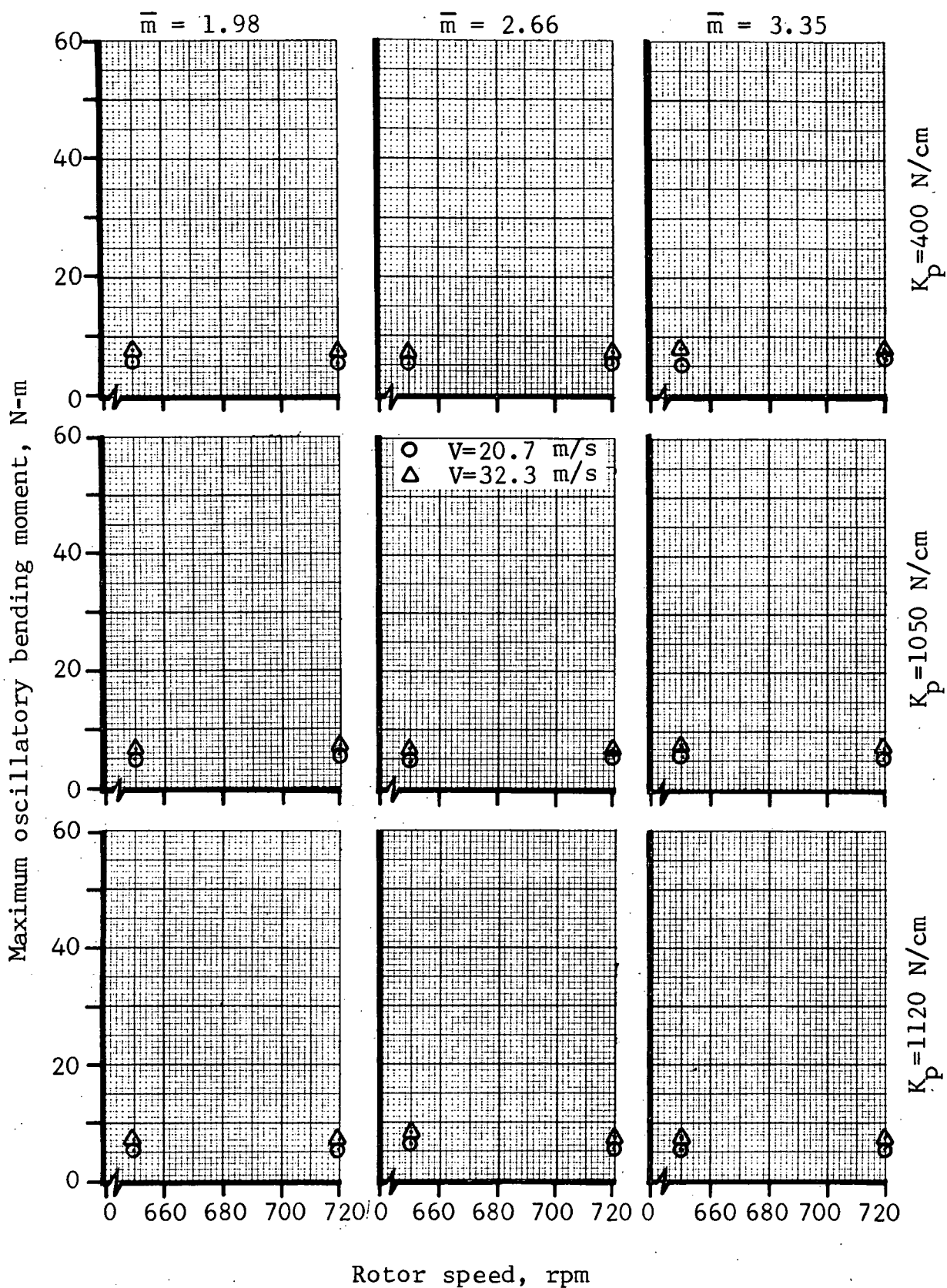


Figure 37. Blade Flapwise Bending Moment @ 47.9 Percent Radius,
 $\alpha_s = -2^\circ$, $\theta_o = 16^\circ$

APPENDIX - Continued

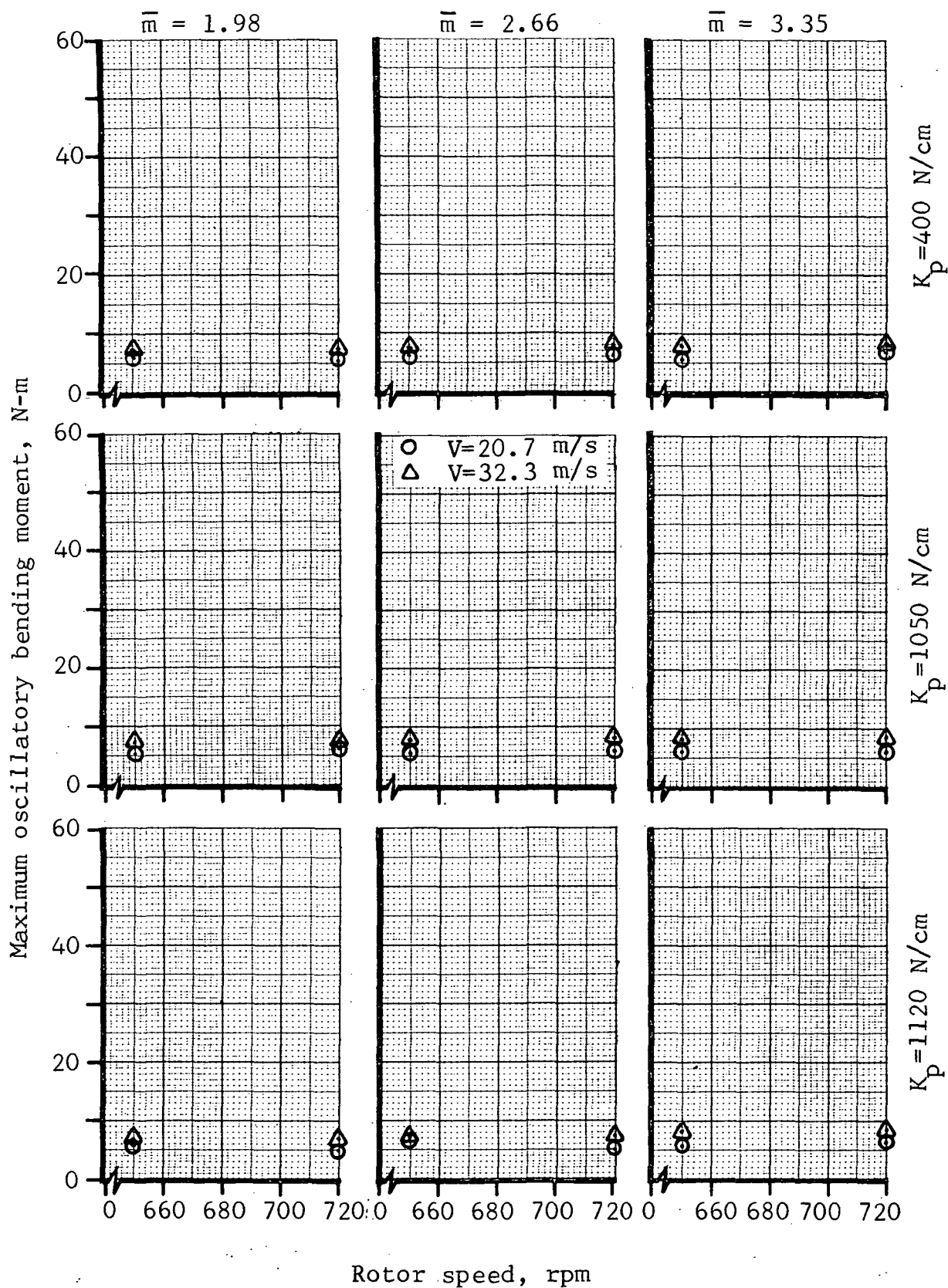


Figure 38. Blade Flapwise Bending Moment @ 59.0 Percent Radius, $\alpha_s = -2^\circ$, $\theta_o = 16^\circ$

APPENDIX - Continued

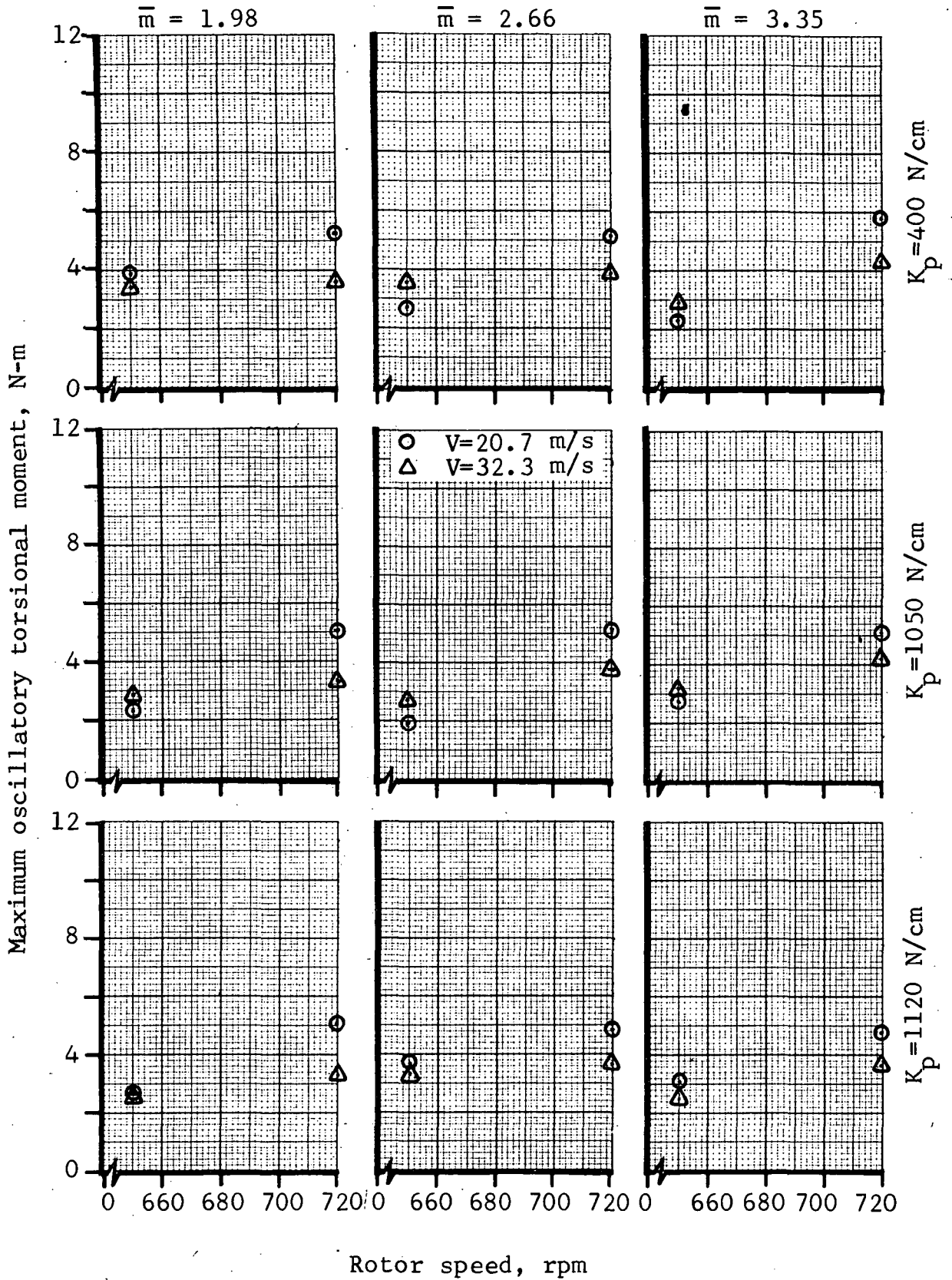


Figure 39. Blade Torsional Moment @ 15.6 Percent Radius,
 $\alpha_s = -2^\circ$, $\theta_o = 16^\circ$

APPENDIX - Continued

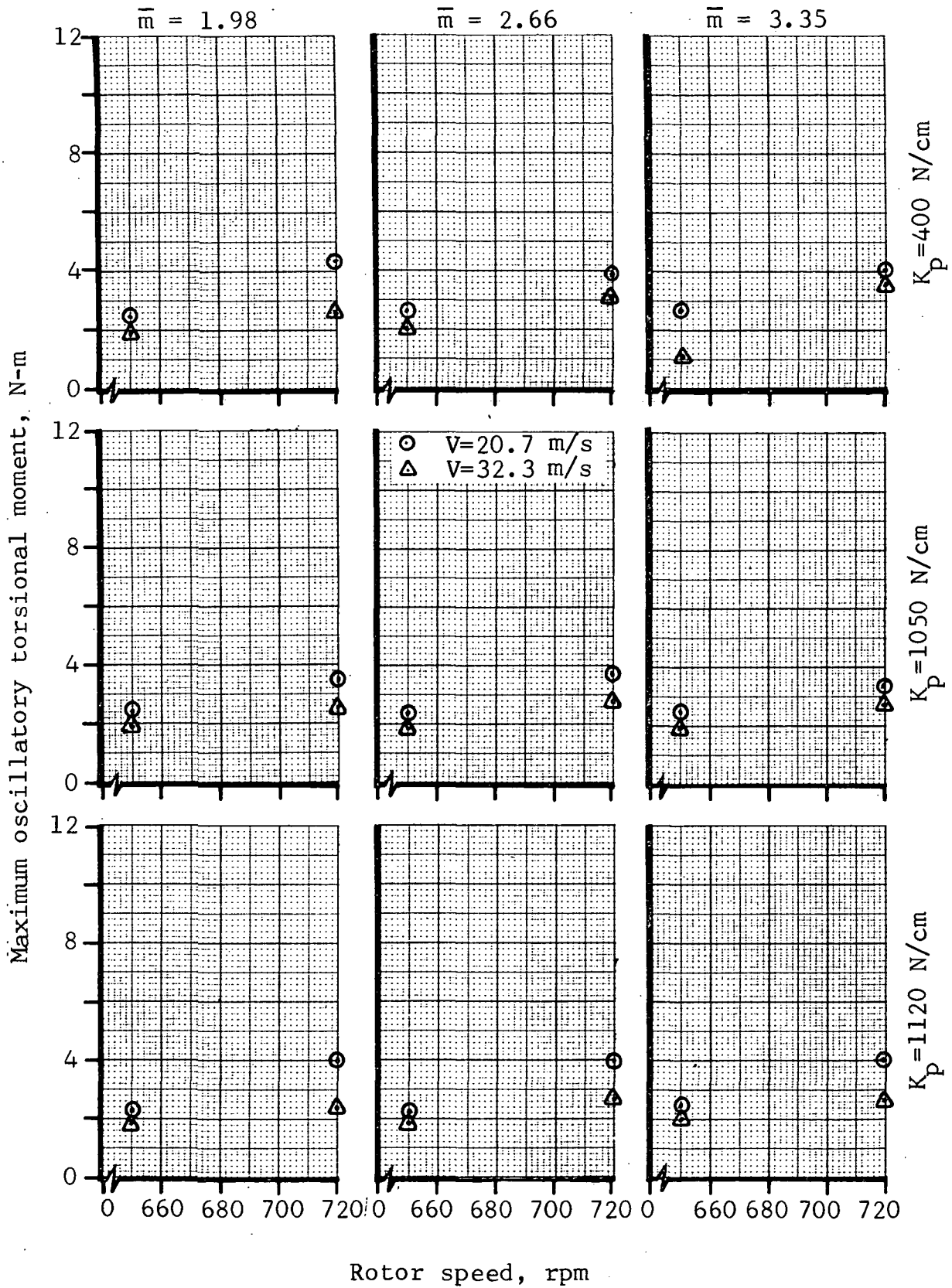


Figure 40. Blade Torsional Moment @ 47.9 Percent Radius,
 $\alpha_s = -2^\circ$, $\theta_o = 16^\circ$

APPENDIX - Continued

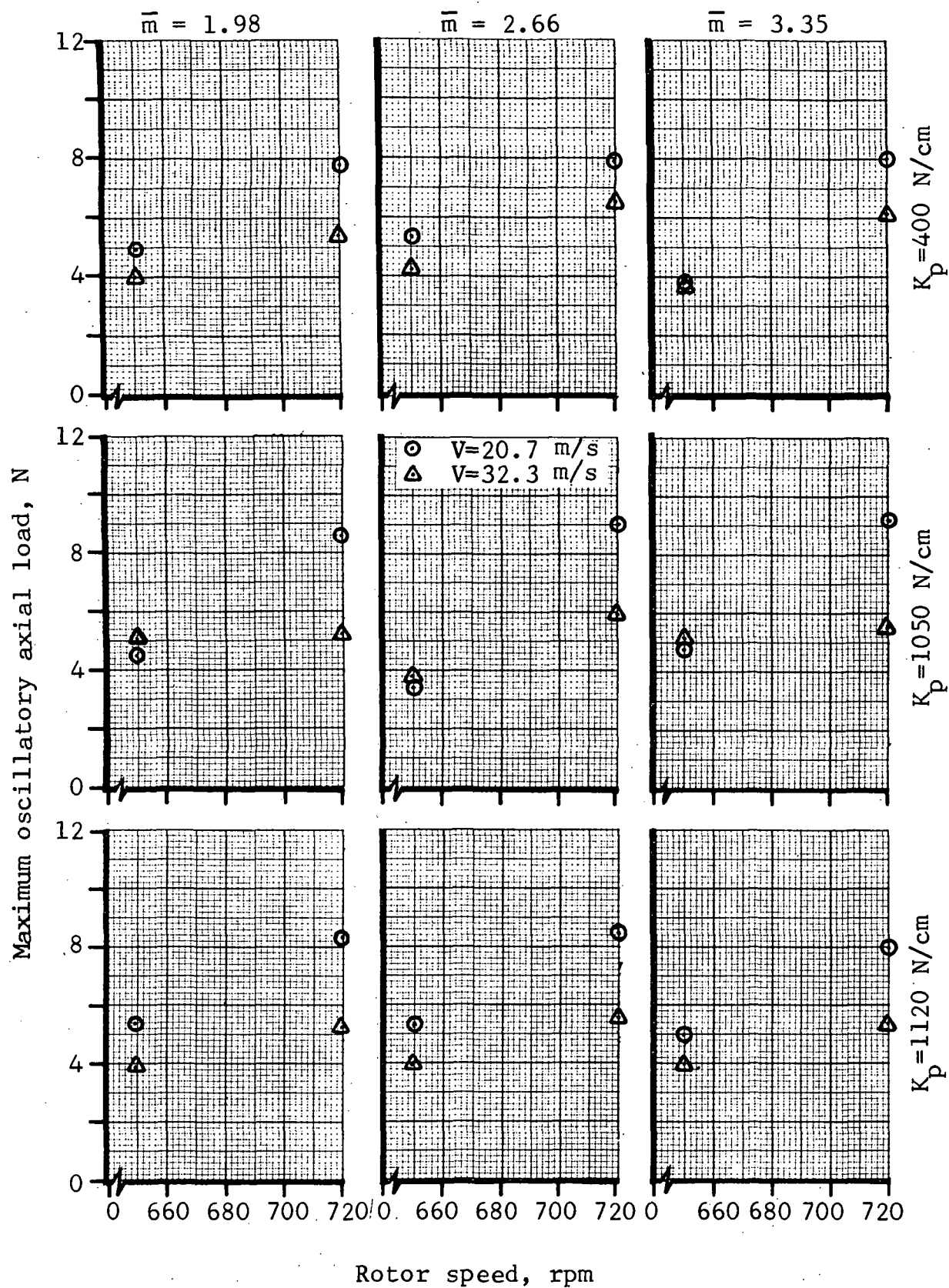


Figure 41. Pitch Link Axial Load
 $\alpha_s = -2^\circ$, $\theta_o = 16^\circ$

APPENDIX-Continued

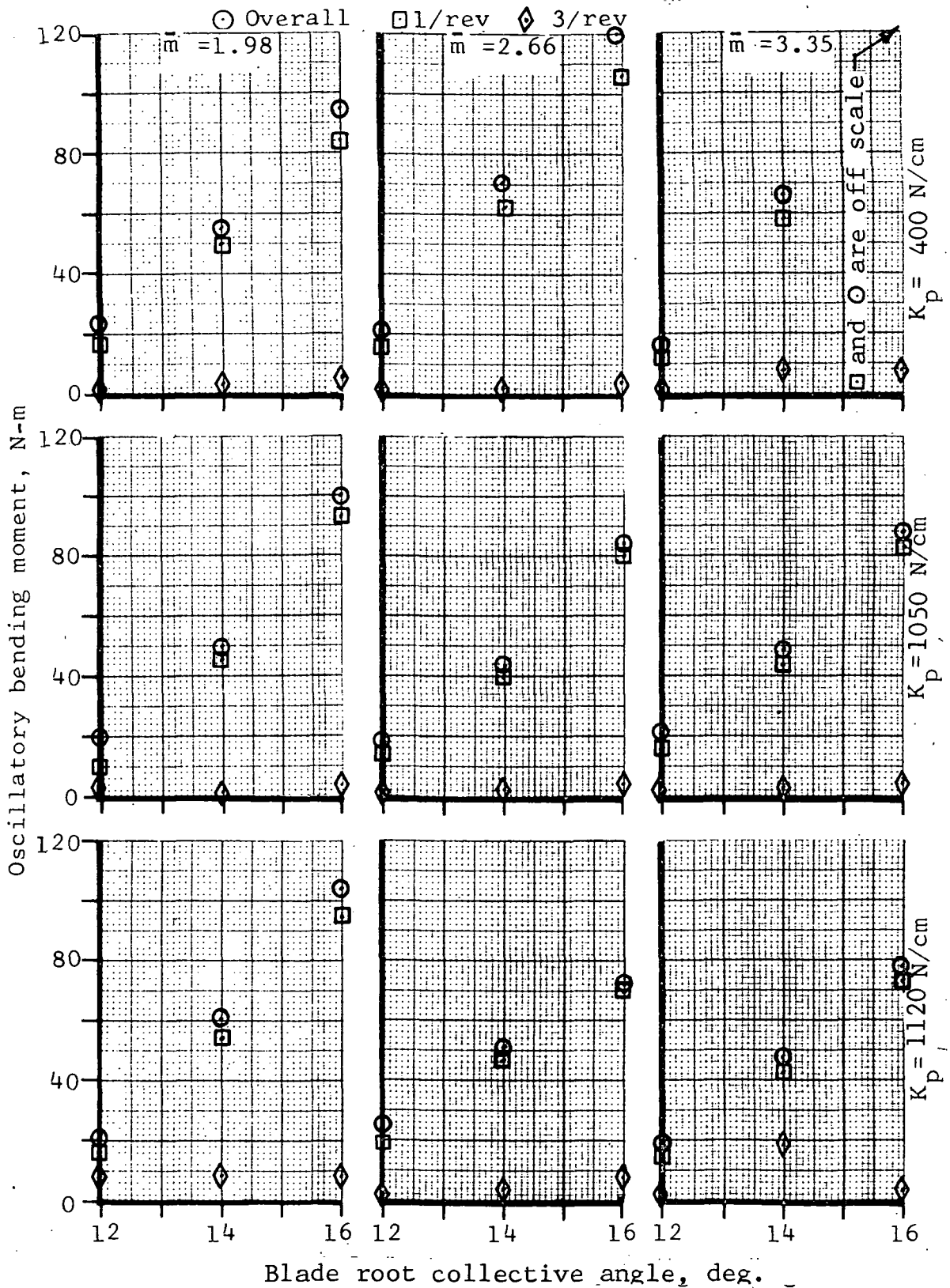


Figure 42. Blade Inplane Bending Moment Vs Collective Blade Angle
 $V=20.7 \text{ m/s}$, $\text{rpm}=720$, $\alpha_s=-2^\circ$, $15.6\%R$

APPENDIX-Continued

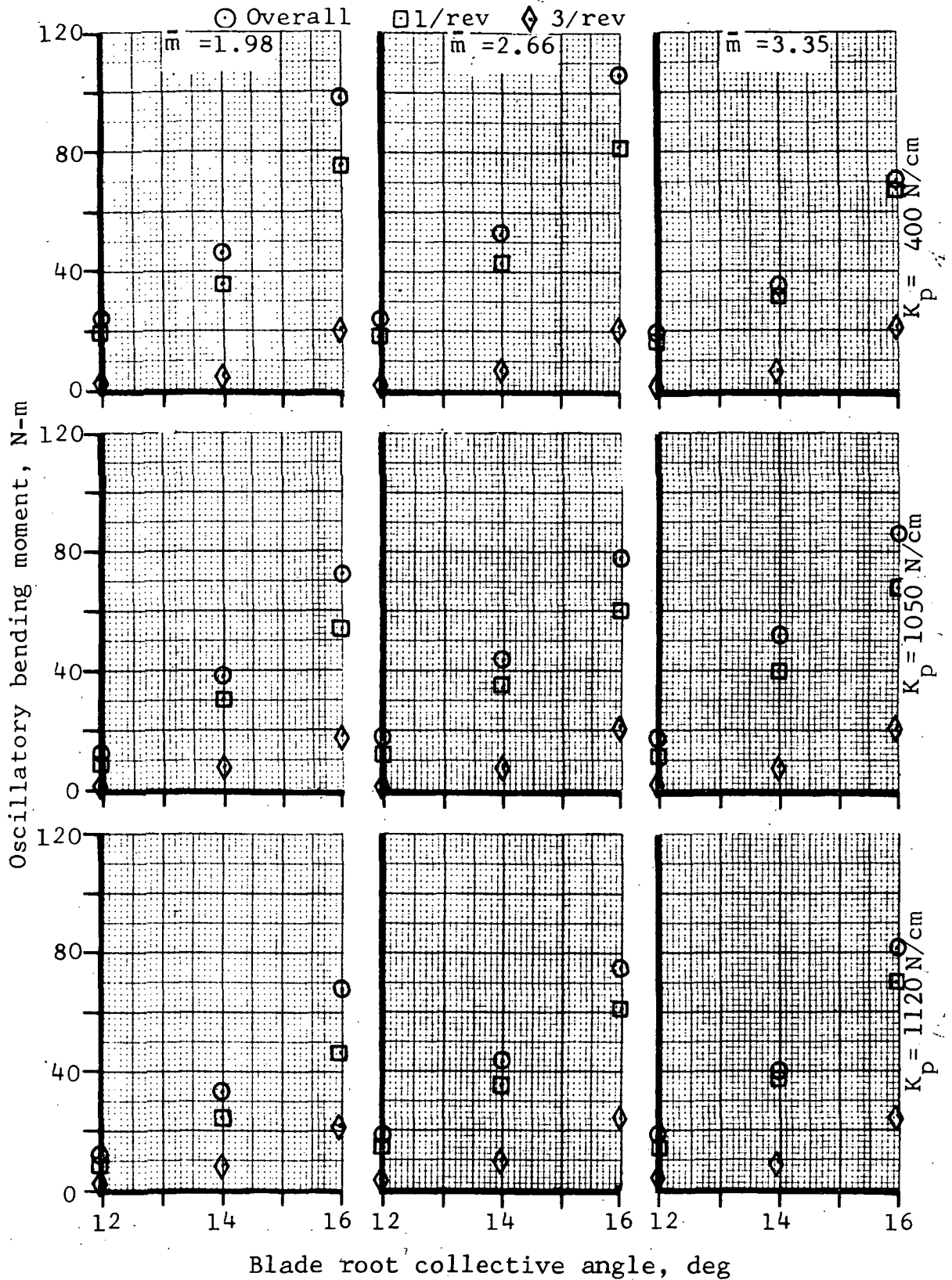


Figure 43. Blade Inplane Bending Moment Vs Collective Blade Angle
 $V=32.3 \text{ m/s}$, $\text{rpm}=650$, $\alpha_s = -2^\circ$, $15.6\%R$

APPENDIX-Continued

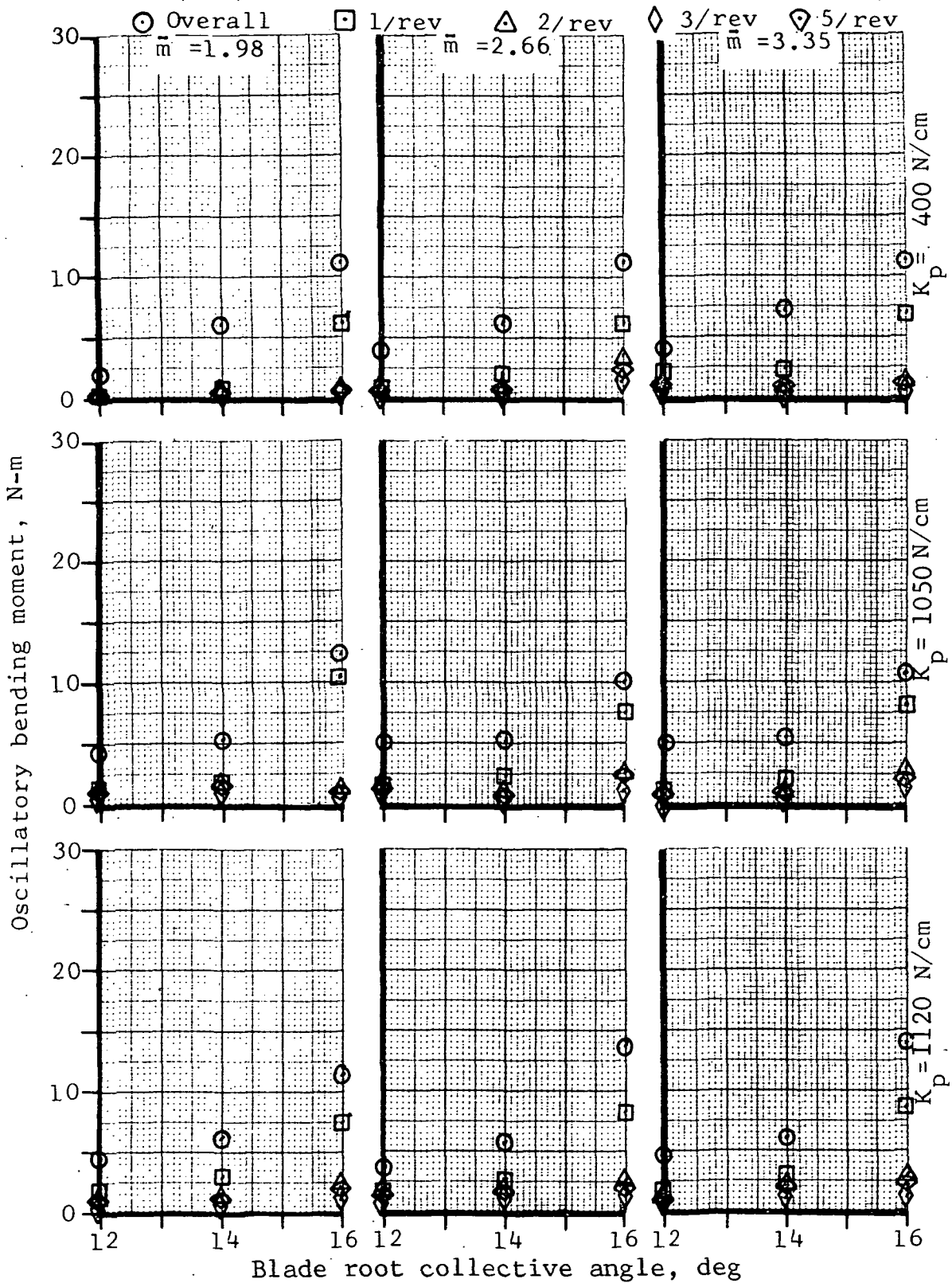


Figure 44. Blade Flapwise Bending Moment Vs Collective Blade Angle
 $V=20.7$ m/s, rpm=720, $\alpha_s = -2^\circ$, 15.6%R

APPENDIX-Concluded

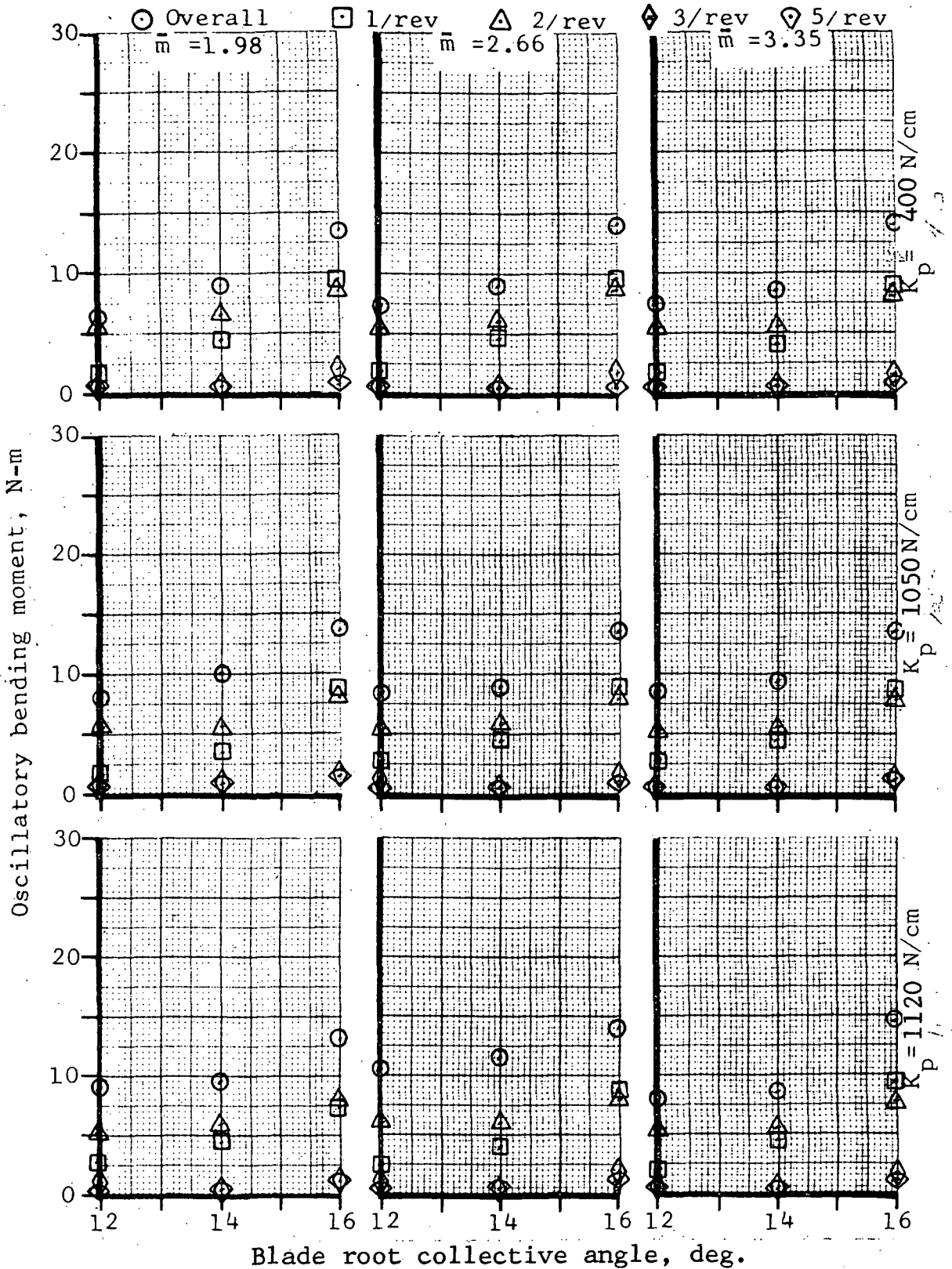


Figure 45. Blade Flapwise Bending Moment Vs Collective Blade Angle
 $V=32.3 \text{ m/s}$, $\text{rpm}=650$, $\alpha_s = -2^\circ$, $15.6\%R$